DESIGN AND CONTROL OF AN INDOOR MINIATURE AUTONOMOUS BLIMP

A Thesis
Presented to
The Academic Faculty

By

Qiuyang Tao

In Partial Fulfillment
of the Requirements for the Degree
Doctor of Philosophy in the
School of Electrical and Computer Engineering

Georgia Institute of Technology

December 2020

DESIGN AND CONTROL OF AN INDOOR MINIATURE AUTONOMOUS BLIMP

Approved by:

Dr. Fumin Zhang, Advisor
School of Electrical and Computer Engineering
Georgia Institute of Technology

Dr. Patricio A. Vela
School of Electrical and Computer Engineering
Georgia Institute of Technology

Dr. Ye Zhao
School of Mechanical Engineering
Georgia Institute of Technology

Dr. David G. Taylor
School of Electrical and Computer Engineering
Georgia Institute of Technology

Dr. Kok-Meng Lee
School of Mechanical Engineering
Georgia Institute of Technology

Date Approved: October 19, 2020

ACKNOWLEDGEMENTS

This thesis would have not been possible without the help and support of many people throughout my Ph.D. study. I owe my heartfelt gratitude to all these people.

First and foremost, I would like to thank my advisor, Dr. Fumin Zhang, for providing me with excellent guidance, enormous patience, career advise, and many resources. Looking back on the days that I joined the lab as an undergraduate student, I marvel at my growth both professionally an personally. His input helped me improve my capabilities of analyzing practical intuitions with theoretical foundations. We went through a large variety of projects and great adventures, many of which I was not able to capture in this thesis. I will miss being a student of you, and hope we will have fruitful future collaborations.

I must thank my thesis committee members: Dr. Kok-Meng Lee, Dr. David G. Taylor, Dr. Patricio A. Vela, and Dr. Ye Zhao, for their precious time and valuable suggestions for the work done in this dissertation.

I gratefully acknowledge the Georgia Robotics and Intelligent Systems (GRITS) Laboratory, the prototyping lab of the Graphics, Visualization and Usability (GVU) Center, and the Invention Studio for their generous support on the facilities and equipment.

I would like to show my gratitude to people who generously assisted during the i-Corps program for exploring the commercial applications of the miniature autonomous blimp presented in this thesis. Especially, Mr. Rich Wagner who served as industrial mentor, Dr. Fumin Zhang who is the principal investigator, Mr. Sean Maxon who participated as co-lead of the team, and all instructors of the cohort.

Finally, I would like to thank my family, friends, and fellow lab members in the Georgia Tech Systems Research (GTSR) lab for their love and support.

TABLE OF CONTENTS

LIST OF TABLES

LIST OF FIGURES

SUMMARY

Aerial robots have been pushing the boundary of indoor capabilities by demonstrating application success in tasks such as surveillance and inspection. However, existing aerial platforms have not developed the smooth and safe indoor operations necessary for human interaction. Existing drones like quadcopters are still notoriously unsatisfactory in aspects including safety and endurance. For example, mini drones usually exhibit sub-ten minute flight times, and require cages and netted enclosures for safe indoor operation.

We present a miniature autonomous blimp that can safely operate in close proximities to humans and can fly for multiple hours, solving the two biggest challenges for indoor aerial robots. The blimp prototype outlined in this thesis is the first of its kind due to features including a saucer-shaped design without tail fin, symmetrical planar actuation, a low-latency off-board control scheme, ultra-light-weight electronics, and an improved localization system. The blimp also has a compact design that favors mobility in confined indoor spaces, making it one of the smallest autonomous blimps in the world.

The modeling, identification, and controller design of the miniature blimp is presented with emphasis on swing oscillation reduction. This undesired motion is inevitable among indoor blimps and can impact many applications. We establish the dynamics model of the swing motion for both hovering and cruising flight. We then propose a procedure to identify the model parameters via multiple means, including physical measurements, computer modeling, and experimental data captured during flight. A swing-reducing flight control system is then developed that incorporates the strong coupling between the translational and rotational movements of the blimp. Waypoint navigation and station-keeping flights are experimentally validated with swing oscillation reduction. The modeling and control methods proposed in this thesis demonstrate the autonomous flight of a saucer-shaped blimp without control surface or tail fin, and is the first realization of the swing stabilization feature among existing indoor miniature blimps reported in the literature.

CHAPTER 1
INTRODUCTION

1.1 Background and Motivation

Indoor aerial robots are gaining increasing attention owing to their promising applications including surveillance, structure exploration, and search and rescue [1, 2, 3, 4]. In particular, human-robot interaction (HRI) with indoor airborne robots is a growing research trend [5, 6, 7, 8]. However, most existing indoor aerial platforms, such as quadcopters, have fast-spinning propellers which may cause safety concerns in human-occupied indoor environments [3, 9, 10, 11]. Besides, these platforms usually have limited flight endurance [12], typically less than 10 minutes for nano drones [13], which restricts their applications. Therefore, a safer robot with longer airborne endurance is increasingly needed.

Lighter-than-air-robots (LTARs) keep themselves aloft without the need for consistent motor action. Hence, LTARs are the most power efficient unmanned aerial system [12], and their endurance can be several orders of magnitude greater than that of heavier-than-air vehicles [14]. The extended flight endurance makes LTARs well-suited to many applications that require sustained airborne presence [14, 15]. Moreover, LTARs can fly quietly due to their reduced requirements on propulsion [16]. The size of LTARs is usually at the scale of a couple meters, such that it can obtain a sufficient amount of buoyancy [12, 17]. As a consequence, most LTARs are designed for outdoor applications instead of indoor purposes.

We develop the Georgia-Tech Miniature Autonomous Blimp (GT-MAB), a lighter-than-air robot specifically designed for indoor applications [18]. The diameter of the GT-MAB is only around 0.7 meters, which allows for good mobility even in confined indoor spaces. Despite the miniature size, the GT-MAB still guarantees a payload capacity for a wide

range of task payloads such as wireless cameras [19]. As shown in Figure 1.1, the GT-MAB is cushioned with a helium-filled envelope, which makes the robot safe to fly indoors, causing no threat to humans and the surroundings even when collisions occur. With the lifting force provided by buoyancy, the GT-MAB has a loitering time of more than 2 hours [20]. The extended flight endurance makes the GT-MAB well-suited to many applications that require sustained airborne presence [14].

Figure 1.1: Children play with the GT-MAB, demonstrating the miniature blimp is safe to fly in the human-occupied indoor environment.

1.2 Requirements for Indoor Operation

The human-occupied indoor environment and the unique applications of miniature blimps require different capabilities of the GT-MAB than conventional airships. Here we summarize a set of requirements to guide the design and development of the GT-MAB.

1.2.1 Requirements on Robot Design

Due to the confinements of indoor spaces, the GT-MAB must have a compact shape so as to avoid undesirable collisions with the environment and possible ruptures when navigating through tight enclosures, such as doorways. Safety needs to be ensured for indoor flight, especially in close proximity to humans. The blimp should have an envelope without sharp edges or tail fins, and propellers needs to be protected in the event of collision. Extended

flight endurance is also essential for most applications of indoor blimps, where sustained airborne presence is highly required. Moreover, the blimp should be expandable for a variety of task payloads, and be convenient to use and maintain.

1.2.2 Requirements on Indoor Mobility

Due to the limited indoor space and close proximity to humans, hovering and slow flight are the most common operating scenarios for indoor blimps. This is in contrast to outdoor airships that are usually designed for long-distance cruising. Therefore, precision multi-degree-of-freedom (DOF) mobility is prioritized for indoor blimps over the speed and efficiency of cruising flight.

Holonomic maneuverability is an essential requirement for many applications of the GT-MAB such as human-robot-interaction and inspection. Such tasks require the blimp to move both longitudinally and laterally, make sharp turns in place, and simultaneously maintain height. This will allow onboard cameras and other directional sensors to be pointed towards a desired direction despite translational movement of the blimp.

Precise position and velocity tracking is also required for an indoor blimp to serve as a research testbed. For example, path planning and source seeking experiments often require the blimp to travel towards a certain direction at a constant velocity. Similarly, swarming and HRI applications typically demand precise position tracking. Attitude stabilization is an essential feature for most applications of the GT-MAB. Swing oscillation is inevitable among indoor blimps due to the underactuated configuration. Moreover, environmental disturbances are unavoidable due to ambient airflow and harmless contact with humans and surrounding objects. Hence, the GT-MAB should be able to stabilize its attitude and recover from disturbances quickly.

1.3 Challenges

1.3.1 Design and Implementation

Light-weight mechatronics is a major challenge when trying to ensure the GT-MAB achieves a compact form that can fulfil the necessary requirements of endurance, actuation, computation, and expandability. The total buoyancy of the blimp depends on the volume of the envelope, which reduces with its diameter in a cubical manner. For instance, the overall payload of the 0.7m-diameter GT-MAB is only about 60 grams. However, the flight endurance of the blimp is proportional to the battery capacity. As such, a significant portion of the precious payload is inevitably occupied by the battery. The challenge is further escalated by the requirement for holonomic maneuverability. Multiple thrusters, their mechanical support, and driving electronics have to be implemented with minimum weight while still providing adequate propulsion. Consistency of the actuation is also required among varying battery levels (which occurs as the battery becomes depleted). Many functionalities of the GT-MAB, such as computer vision, demand intensive computational power. Such computation will occupy large amounts of valuable payload and consume a lot of energy if implemented onboard. However, if realized off-board, communication between the aerial robot and the ground station must meet the demands on low latency and high update rate.

Localization is another challenge for miniature indoor blimps. Such robots usually rely on optical motion capture systems to obtain pose information in GPS-denied indoor environments. These localization systems incorporate multiple infrared cameras to track the reflective markers installed on the robot. Infrared illumination lamps are required to ensure the visibility of the reflective markers to the cameras. Indoor blimps usually use metallized film for their envelope to reduce gas permeability. Such shiny envelopes cause excessive reflections that are often stronger than the markers. This undesirable reflection induces interference in a motion capture system, and impacts both the accuracy and reliability of the pose measurement.

1.3.2 Modeling and Identification

The unique aerodynamic shape, the complex envelope geometry, and the slow-flying nature of indoor blimps are the major difficulties in modeling the motion of the GT-MAB. In contrast to outdoor airships with cigar-shaped envelopes, the GT-MAB has a saucer-shaped envelope for omnidirectional maneuverability. Due to the high agility and safety requirements for indoor operation, there is no tail fin or control surface on the GT-MAB. As a result, analytical methods for modeling outdoor airships such as [21, 22] cannot be applied. Indoor blimps usually use Mylar film for sturdier envelopes and slower deflation [23]. Therefore, as seen in Figure 1.1, folding is usually inevitable on this non-stretchable envelope. The imperfect shape may cause inaccuracy when calculating model parameters from the geometry of the blimp [5]. The complex geometry of the envelope also makes it difficult to estimate model parameters with CFD (computational fluid dynamics) simulations [24]. Moreover, wind tunnel experiments for outdoor airships like [25, 26] cannot be conducted on the slow-flying indoor MABs since the tests are usually designed for high-speed vehicles.

1.3.3 Flight Control

Swing oscillation is an inevitable challenge to the fight control among indoor miniature blimps. The main difficulties in reducing the swing motion of the GT-MAB are its unique underactuated design, fluctuated position measurement, and latency in the control system.

All onboard electronics of the GT-MAB, including the thrusters, are installed on one single gondola mounted underneath the envelope. This configuration reduces weight, ensures alignment between thrusters, and enhances the durability of the blimp. However, this underactuated thruster configuration also causes undesired pitching or rolling torque once the motors are on. This disturbance shows a more significant impact on the roll and pitch motion of the GT-MAB when more powerful thrusters are installed for better maneuverability against airflow. Moreover, the inevitable environmental disturbances such as indoor

air ventilation also introduce undesired swing motion to the blimp.

Most MABs require external localization systems to fly inside the GPS-denied indoor environment. These systems usually incorporate multiple ceiling-mounted infrared cameras to track the retroreflective markers installed on the robots. The localization markers are usually installed at the top of the envelope for the best visibility to the cameras. The measurement from the localization systems is the pose of the markers. The marker position has constant offset above the center of gravity (CG) of the GT-MAB and is used to represent the position of the blimp when there is negligible roll or pitch angle. Therefore, the marker position becomes fluctuated when the GT-MAB is swinging. Moreover, since the pivot of the swing oscillation, CG, is located between the markers and the actuators, the markers will first move toward the opposite direction of the motor thrust, and then towards the same direction. This undesired behavior may further aggravate the swing oscillation.

A ground station computer is required to interface with the external motion capture system and to compute the pose of the GT-MAB. Other computationally intensive tasks, such as computer vision, are also implemented on the ground station computer to save the payload and energy onboard the blimp. Therefore, wireless communication is required to exchange data between the ground station and onboard electronics of the GT-MAB. As reported in work [27], control system latency of an indoor blimp with external localization device and off-board computing is around 0.2-0.4 seconds. The latency is acceptable to control the relatively slow translational and steering motion of the GT-MAB, but cannot satisfy the needs for regulating the fast swing oscillation.

1.4 Contribution

The main contributions of this thesis are the creation of the miniature autonomous blimp, GT-MAB, and the modeling and control methods that stabilize the swing oscillation that is inevitable among MABs. A summary of the contributions is described as follows.

1.4.1 Design and Implementation of GT-MAB

- We proposed a symmetrical saucer-shaped indoor autonomous blimp with no tail fin. This configuration provides symmetrical properties and balances air drag, buoyancy, and accessibility for indoor applications. To the best of our knowledge, GT-MAB is the first indoor blimp that uses a symmetric saucer-shaped design. The GT-MAB has a diameter of about 0.7m, which is among the smallest indoor autonomous blimps.

- We incorporated an X-shaped symmetrical actuator configuration for holonomic mobility that allows thrusters to only operate in a single direction. Moreover, a power module is developed that provides consistent voltage to the blimp despite battery voltage variations. The incorporation of such actuator configuration and power module is our novel contribution among indoor aerial robots.

- We developed a low-latency off-board control scheme that is specifically suitable for indoor aerial robots. The scheme reduces onboard power consumption and allows computationally intensive algorithms to be executed on the ground station. The low-latency and high-update-rate features enable off-board computation for real-time tasks of the GT-MAB such as attitude stabilization. The proposed system has the lowest latency and the highest update rate among indoor flying robots.

- We designed a light-weight electronic suite which reserves precious buoyancy for battery, actuation, structure, and task payload. The core electronics board integrates all essential functionalities of the GT-MAB, and weighs only less than half a gram. We believe this is the lightest implementation among such devices with the same functionality.

- We developed an active positioning marker for indoor aerial robots that does not require external infrared illumination in current optical motion capture systems. The elimination of external lamps resolves the strong reflection from the shiny metalized

envelopes of indoor miniature blimps, which improves the reliability and accuracy of the motion capture measurement. Weight of the active marker is roughly one gram, making it the lightest design of its kind, and is the only realization that meets the strict payload limitation of indoor miniature blimps.

- Safety, consistency, convenience and expandability features are emphasized for the GT-MAB to serve as a robotic research testbed and education tool for a wide range of users. The GT-MAB is an aerial platform that is robust to collisions and never causes damage. To the best of our knowledge, the GT-MAB has supported a relatively large number of experiments compared to other indoor blimps.

1.4.2 Modeling and Identification

- We established and identified the 4-DOF decoupled motion model for the saucer-shaped GT-MAB with no tail fin. We believe this is the first effort in the literature on the modeling of the saucer-shaped miniature blimp.

- We examined the undesired swing oscillation of the GT-MAB during hovering flight. Given the unique design and operating scenarios of indoor blimps, we proposed a procedure to identify the model parameters using multiple ways including physical measurements, computer modeling and flight data captured during swing motion.

- We also investigated the swing oscillation of the GT-MAB during cruising flight. The dynamics model of the coupled translational and rotational motion is established and identified. To the best of our knowledge, we are the first in investigating and experimentally identifying the swing oscillation of indoor miniature blimps.

- With the identified motion model, we analyzed the impact of control system latency on the swing stabilization of the GT-MAB. The results guide the control system design and mechatronic development of the latest GT-MAB prototype.

1.4.3 Flight Control System Design

- A flight controller is designed to navigate the GT-MAB in 3D space. The controller is developed upon the decoupled 4-DOF motion model on translational and steering movements. Waypoint navigation is realized based on the non-holonomic motion of the blimp. We are the first to demonstrate autonomous flight control of saucer-shaped indoor blimps with no tail fin.

- The swing oscillation of the GT-MAB is stabilized during hovering flight. An updated flight control system is designed that stabilizes the swing oscillation while simultaneously maintaining the position and heading of the blimp. The controller incorporates the identified dynamics of the swing oscillation in addition to the decoupled 4-DOF motion model. To the best of our knowledge, this is the first realization of swing stabilization among indoor miniature blimps.

- The swing stabilization feature is then expanded to cruising flight. We developed a flight controller that stabilizes the swing oscillation while tracking the desired velocity. The controller incorporates the coupled dynamics between the translational and rotational motion of the GT-MAB. As far as we know, this is the first and only realization of swing stabilization with velocity tracking for indoor MABs.

- We expanded the swing-reducing velocity controller for both station-keeping and waypoint navigation in 3D space. Experimental results show the effectiveness of the functionalities and demonstrate the robustness of the swing-reducing velocity controller in spite of large disturbance. To the best of our knowledge, we are the first to demonstrate station-keeping and waypoint navigation of indoor miniature blimps with swing stabilization.

- The thruster-hull interaction is inevitable for all indoor miniature blimps. We investigated and experimentally measured the asymmetrical actuation for the heave motion

of the GT-MAB. An model predictive controller (MPC) is designed that copes with the asymmetrical actuation constraint. Faster settling time and lower overshoot are achieved compared to the conventional proportional-integral-derivative (PID) control. To the best of our knowledge, this is the first implementation of MPC, a computationally intensive algorithm, on indoor miniature blimps.

- Indoor miniature blimps usually rely on ceiling-mounted motion capture systems due to the GPS-denied environment. There are positioning markers usually located on top of the envelope for better visibility to localization cameras. The marker position is widely used to represent the position of the blimp among existing works as the roll and pitch angles are assumed to be zero. However, since the center of gravity is located between the markers and the actuators, the markers will first move in the opposite direction to the actuation, and then follow the thrust direction. We are the first to pinpoint this undesired phenomenon with experimental data, and have resolved this issue by representing the position of the blimp with CG position calculated from the pose of the markers and the identified motion model.

1.5 Thesis Overview

The rest of the thesis is organized as follows. Chapter 2 presents a review of the literature relevant to this research work. Chapter 3 demonstrates the design and development of the indoor miniature blimp GT-MAB. Chapter 4 introduces the modeling and waypoint navigation of the GT-MAB without swing stabilization. Chapter 5 extends the modeling of the GT-MAB by including the swing-related dynamics into consideration. Then, Chapter 6 presents the development of flight controllers with swing-stabilization. Finally, Chapter 7 concludes this document and discusses future work.

CHAPTER 2

RELATED WORK

2.1 Design Trends of Indoor Blimps

Traditional outdoor airships have been developed for more than 100 years. As shown in Figure 2.1a, outdoor airships usually have cigar-shaped envelopes to reduce the aerodynamic drag as they are designed for long-distance cruising, and have multiple tail fins with control surfaces to stabilize and control their attitude [28, 29]. Larger-scale indoor blimps with size around two meters, such as [26, 30, 31], usually have similar cigar-shaped layout as outdoor airships and are also equipped with tail fins, as illustrated in Figure 2.1b. Instead of using control surfaces for steering, these indoor blimps control their heading with motors. Indoor blimps with size around one meter, including [32, 33, 34, 35], usually don't have tail fins nor control surfaces, as seen in Figure 2.1c and Figure 2.1d. Some designs incorporate symmetrical envelope for larger payload capacity and omnidirectional mobility.

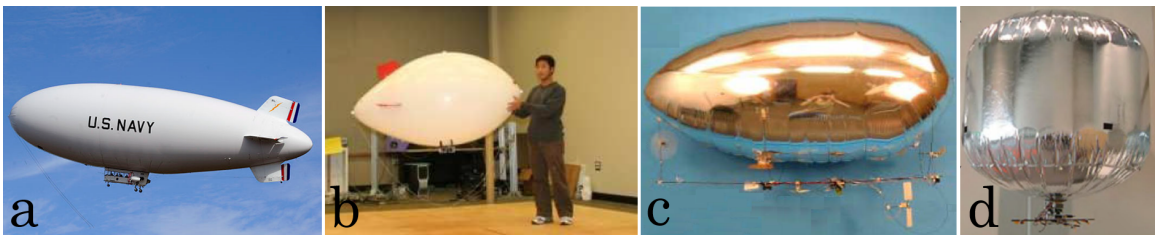

Figure 2.1: Typical designs of outdoor airship (a), indoor blimp with size around two meters (b), and indoor blimps with sizes around one meter (c,d).

Shown in Figure 2.2, indoor autonomous blimp with size less than one meter, such as [18, 23, 36, 37] are developed recently. These miniature blimps with huggable size are highly preferred for indoor applications due to the confined environment. Most indoor MABs have symmetrical saucer-shaped envelope to balance payload capacity, safety, air

drag and maneuverability. Due to the nature of the non-elastic film of the envelope, there are folding on the envelope of indoor MABs. Moreover, all electronics and actuators of MABs are integrated on one single gondola for weight reduction. As a consequence, the indoor MABs are typically underactuated [38]. Table 2.1 concludes the typical designs of airships and indoor blimps with different sizes.

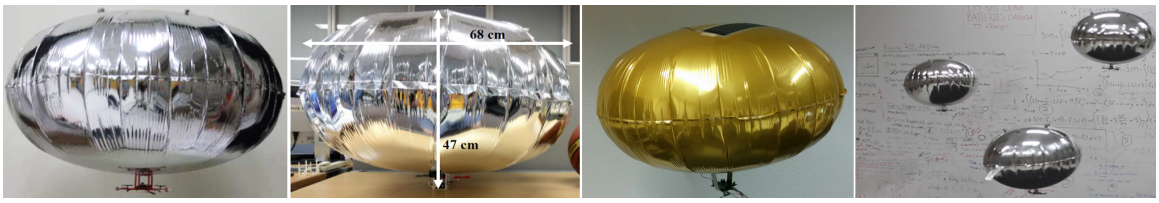

Figure 2.2: Typical designs of indoor blimps with sizes less than one meter.

Table 2.1: Typical designs of outdoor airships and indoor blimps with different sizes.

	Outdoor	Indoor ($\sim$2m)	Indoor ($\sim$1m)	Indoor ($<$1m)
envelope Shape	Cigar	Cigar	Cigar and Symmetric	Symmetric
Tail Fins	Yes	Yes	Yes and No	No
Control Surface	Yes	No	No	No
Distributed Actuator	Yes	Yes and No	Yes and No	No

2.2 Dynamics Modeling of Indoor Blimps

Dynamics modeling of large-sized airships with conventional shape have long been studied [22]. However, due to the limitations including light-weight mechatronics, miniature indoor blimps are not widely available until recently. Only a few projects address the modeling of the indoor blimps with sizes similar to the GT-MAB.

The existing approaches for modeling the dynamics of indoor blimps can be categorized into two groups, physics-based and data-driven. The physics-based methods investigate the aerodynamics from the specific shape of the blimp [33], while the data-driven approaches discover the dynamics from data measurements [27].

2.2.1 Physics-based Methods

The work [39] presented the 6-DOF motion model of a cigar-shaped indoor blimp, and simplified the model to separate the translational and steering motion. The model was then simplified to only containing the decoupled movements on the horizontal plane for the convenience of studying the control strategy under wind disturbance. The identification of the parameters, such as viscous coefficient, was not discussed. [40] established the 6-DOF mathematical model of a cigar-shaped indoor blimp. The pitch and roll angles were assumed to be small, and the model is simplified by removing the roll and pitch dynamics. Authors of [33] modeled the 6-DOF dynamics of an indoor blimp with cigar-shaped envelope, and developed a simulator based on the model. The model parameters were analytically derived from the geometry of the envelope. All these works [33, 39, 40] focus on modeling indoor blimps with cigar-shaped envelope. Unfortunately, analytical methods may only be valid for a specific class of envelope shapes [24]. As a result, existing analytical methods on determining model parameters for traditional cigar-shaped blimps cannot be applied to the saucer-shaped GT-MAB.

Computational fluid dynamics (CFD) and wind tunnel tests are commonly used approaches for outdoor airships that have less dependency on the shape of the envelope. CFD simulations numerically determine the aerodynamic parameters, i.e., drag coefficient, as a function of envelope geometry [24]. As shown in Figure 2.2, indoor MABs usually have folding on their envelops. The complex surface geometry of the envelope makes it difficult to accurately construct the mesh model and perform CFD simulations. Wind tunnel tests are another commonly adopted approach to experimentally investigate the aerodynamics of larger-sized airships [25, 41]. Hovering and slow-flying are the most common operating scenarios for indoor MABs, while outdoor airships are usually designed for cruising. As a result, wind tunnel tests are not applicable due to the low-speed nature of indoor MABs.

2.2.2 Data-Driven Methods with Known Model Structure

Due to the difficulties in applying physics-based methods on indoor MABs, data-driven approaches are usually incorporated to model the aerodynamics of miniature indoor blimps.

The work [27] simplified the dynamical equations of an indoor blimp along its vertical axis, and then identified the model parameters from the step response of the vertical motion. The parameters of upward and downward motion were identified separately due to the asymmetric dynamics of the vertical motion. Unfortunately, only vertical motion was considered in this work. Our previous work [20] simplified the motion model of GT-MAB into decoupled translational and steering movements, and each motion primitive was identified separately. Similarly, the recent work [4] simplified and identified the model of an indoor blimp as decoupled altitude and planar movements. The work [42] established the 6-DOF motion model of an indoor MAB, and introduced the experiment for identifying the drag coefficients of translational and steering movements. However, identification of the roll and pitch motions were not presented in these works [4, 20, 42]. To the best of our knowledge, our previous work [38] is the only literature that experimentally identified the swing-related roll and pitch motion of indoor blimps. However, the coupling between the rotational and the translational movements was omitted in [38]. Our recent work [43] extended the previous efforts [38] on modeling the swing motion of indoor blimps by including the coupling between the translational and rotational movements into consideration.

2.3 Flight Controller for Indoor MABs

Flight controllers for indoor blimps can be categorized into two groups based on whether a dynamic model is required. Due to the lack of dynamics model, large portion of the existing controller designs for indoor MABs are based on methods such as PID and fuzzy logic. Moreover, for the existing works in both categories, none of them has addressed the control of the coupled translational and rotational motion of indoor miniature blimps.

2.3.1 Controller Design without Dynamics Model

The work [44] compared PID and fuzzy logic algorithms for altitude control, and presented a fuzzy logic controller for collision avoidance. Authors of the work [32] developed a biologically based flight controller with visual information from two camera inputs. PID controllers are designed in [17, 35, 45] for motion control and landing. Cooperative control of multiple neural networks are reported in [46] for the robustness with mechanical failures. The work [34] presented a behavior-based navigation system for an indoor blimp.

2.3.2 Controller Design with Dynamics Model

The work [39] studied the control strategy under wind disturbance, and verified the proposed controller by simulation. Authors of [40] presented both modeling and controller design of a solar powered indoor blimp. The experimental results showed the blimp can successfully track a straight path in 3D space. [33] designed neuromorphic controllers, and trained the neural network using a simulator with identified dynamics model. The trained controller is then transferred on the physical blimp, and resulted very similar behavior with the simulated one. The works [27, 47, 48] designed a predictor-based controller to compensate for the system latency. Experimental results showed the controller can keep the blimp at the desired altitude. However, only the altitude-related modeling and control was considered in [27, 47, 48]. Our previous work [20] designed controllers for the translational and steering motion of the GT-MAB, and designed a waypoint following controller by combining a set of motion primitives. Similarly, the recent work [4] designed flight controllers for the decoupled vertical and planar motions of an indoor blimp. Moreover, PD controllers were implemented for the motion primitives of MABs with tilting [10] and quadcopter-like [49] actuator configurations. Our recent work [50] designed a control system to stabilize the swing oscillation during hovering flight. However, the control system introduced in [50] cannot stabilize the oscillation in cruising flight, due to the strong coupling between the translational and rotational movements of indoor MABs.

CHAPTER 3
DESIGN AND IMPLEMENTATION OF GT-MAB

3.1 System Overview

The Georgia Tech Miniature Autonomous Blimp (GT-MAB) is one of the smallest indoor autonomous blimps in the world. The blimp features outstanding safety, extended flight endurance, and expandability for versatile tasks including 3D field mapping [20, 36] and human-robot interaction [9, 19, 51], and has served as a testbed for deep-learning-based localization and multi-agent path planning [52, 53].

As demonstrated in Figure 3.1, the GT-MAB system consists of a ground station, one or multiple aerial robots, and an indoor motion capture system. The ground station interfaces the localization device, hosts the flight control software, processes computational intensive tasks, and communicates with the blimps wirelessly. The ground station is built around a generic computer to assure the compatibility for new device integration and software reuse. Moreover, each ground station supports multiple blimps simultaneously, enabling cooperative behaviors in multi-robot swarm applications. The aerial robot consists of a helium-filled envelope that supports an electronics package gondola beneath and localization markers above.

GT-MAB has a workflow different from most aerial robots, due to its unique off-board control scheme discussed in Chapter 3.3.3. As illustrated in Figure 3.1, the workflow of the system can be summarized as three major steps:

1. The ceiling-mounted motion capture cameras take photos of the positioning markers on top of the blimp at high frame rate. The image stream is transmitted in real time to the ground station computer via Ethernet.

2. The ground station computer calculates the pose of the blimp based on the image

stream from the motion capture cameras. Once the pose information is ready, the flight control software running on the ground station computer calculates the desired actuation, and encapsulates the controller outputs into a communication packet. The ground station transceiver obtains the data packet from the computer, and then sends the control commands to the blimp wirelessly.

3. The GT-MAB updates the actuation of the corresponding thrusters upon the reception of the control commands. At the same time, data from the onboard sensors will be transmitted back to the ground station through wireless link.

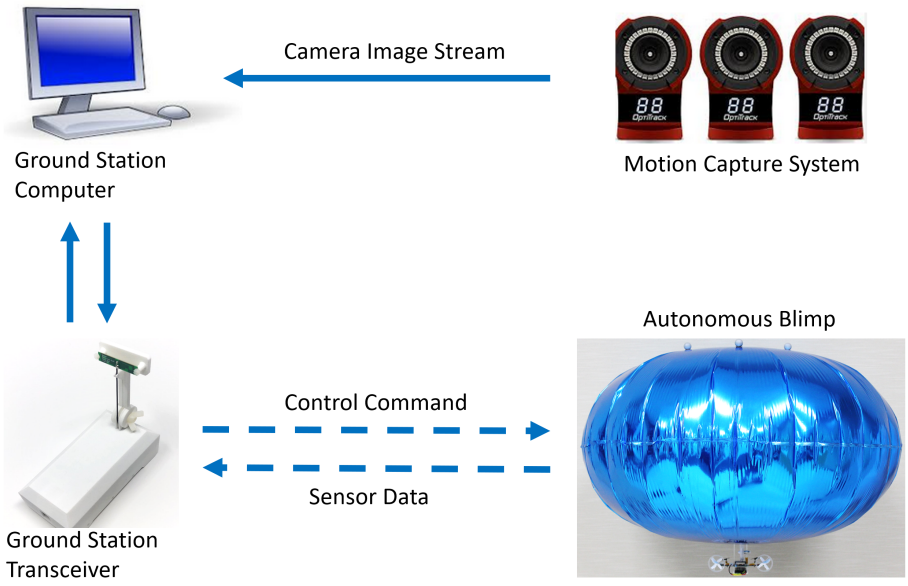

Figure 3.1: Major components and workflow of the overall system. Solid arrows denote wired connection and dashed arrows represent wireless communication.

3.2 GT-MAB: Two Generations

There are two major generations through the development of GT-MAB. A brief comparison among the prototypes is shown in Table 3.1.

The first generation platform, also referred to as GT-MAB 1.0, is designed to support the waypoint navigation missions as discussed in Chapter 4. As shown in Figure 3.2, there

Table 3.1: Comparison among major generations of GT-MAB

Term	GT-MAB 1.0	GT-MAB 1.5	GT-MAB 2.0
Planar movement	Non-holonomic	Holonomic	Holonomic
Planar actuation	Asymmetric	Asymmetric	Symmetric
Planar thruster	Bi-directional	Bi-directional	Uni-directional
Propeller guard	None	Partial thruters	All thruters
Processor	8-bit AVR	8-bit AVR	32-bit ARM
Comm. latency	45.2 ms	15.2ms	387us
System latency	192.2ms	30.5ms	15.7ms
Actuator power source	Battery Voltage	Battery Voltage	Constant Voltage
Power consumption*	242.7mW @10Hz	301.6mW @120Hz	46.2mW @2kHz

*The overall power consumption of the gondola with motor thrust set to zero. The power consumption is measured at the maximum supported controller update rate of the corresponding system.

are four thrusters installed on the gondola. The two vertically mounted motors are used to change the altitude, and are counter rotating to cancel the torque reaction. The two horizontal thrusters enable the blimp to fly forward and backward. These motors can also provide differential thrust for the steering motion. A light-weight variant is also developed to allow for larger payload capacity or flight using a smaller helium envelope.

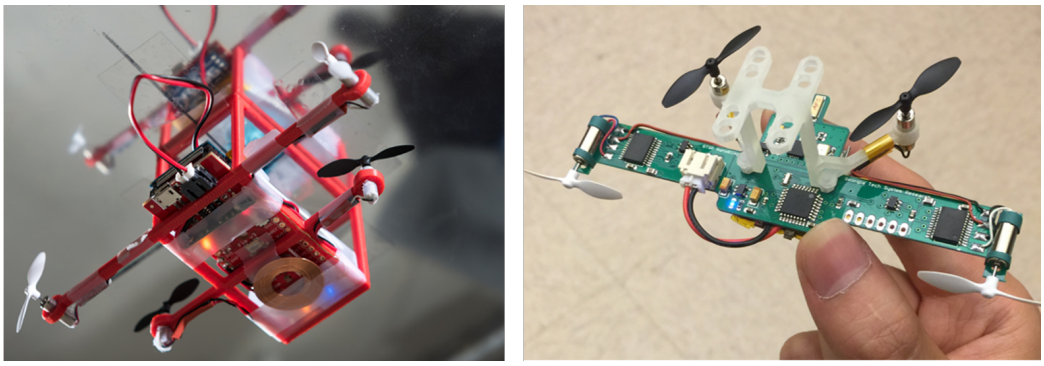

Figure 3.2: GT-MAB 1.0 with standard (left) and compact (right) form factors.

GT-MAB 1.5 is an upgrade over its predecessor with lateral actuation and lower system latency. As shown in Figure 3.3, a lateral thruster is added to provide actuation in the sway direction. The addition of the lateral actuation enables holonomic planar movement, which is essential for applications such as station-keeping and human-robot interaction. System latency is also reduced with refined software implementation and improved communication. Coreless motors and low-diameter multi-blade propellers are chosen for lower

shaft inertia. With low system latency and faster actuator response, the GT-MAB 1.5 enables swing oscillation reduction during station-keeping flight. Detailed discussion on the impact of system latency on attitude stabilization is presented in Chapter 6.1.

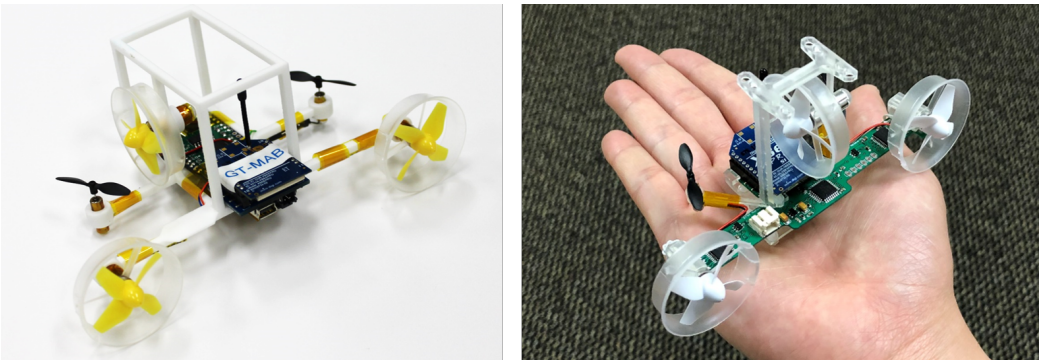

Figure 3.3: GT-MAB 1.5 with standard (left) and compact (right) form factors.

GT-MAB 2.0 is a major update based on our past experience on the development and deployment of indoor miniature blimps. The experimental and analytical results from our past works pinpoint the directions of the improvements. The latest GT-MAB also addresses the requirements identified from the deployment of GT-MAB on various research topics, and the exploration on commercial applications. As a result, GT-MAB 2.0 has comprehensive improvements over its predecessors in actuation, communication, localization, and compactness. Features such as safety, consistency, convenience and expandability are also enhanced. The major system components of the latest GT-MAB are shown in Figure 3.4. Detailed description on the featured designs of GT-MAB 2.0 can be seen in Chapter 3.3.

3.3 Key Features of GT-MAB

The GT-MAB is one of the smallest indoor blimps in the world, and solves the two biggest challenges of indoor aerial robots, safety and endurance. This section we present the key features that are exclusive to the GT-MAB, and the underlying technologies and design philosophy which can inspire future development of indoor aerial robots.

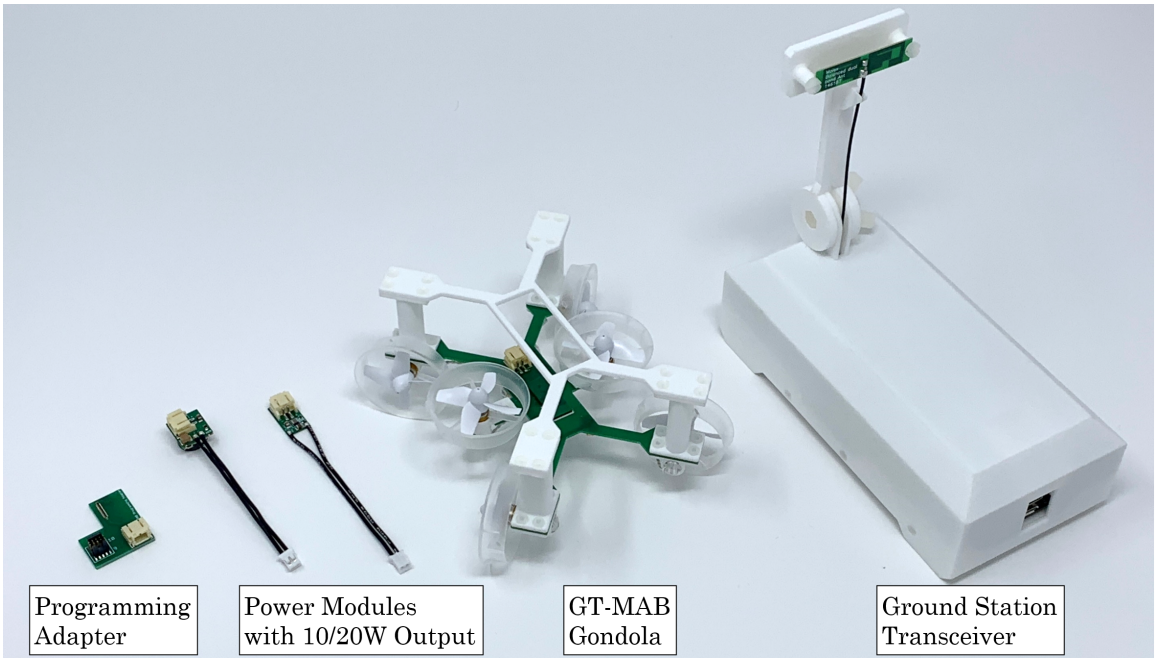

Figure 3.4: GT-MAB 2.0 with major system components.

3.3.1 Saucer-shaped Envelope with no Tail Fins

The GT-MAB incorporates a saucer-shaped envelope without fins or control surfaces. To the best of our knowledge, this configuration is the first of its kind among indoor autonomous blimps.

In contrast to outdoor airships, indoor MABs prioritize slow-speed maneuvers due to highly constrained spaces with possible human occupation. Under low velocity, control surfaces such as rudders have negligible efficiency, and tail fins can reduce maneuverability [54]. Moreover, tail fins are collision-risks that can jeopardize the blimp platform and the surrounding objects. In the presence of humans, the smooth helium envelope of the GT-MAB is dramatically preferred as sharp edges on tail fins may be especially dangerous.

Application scenarios of the GT-MAB such as HRI and inspection require bidirectional and symmetric maneuverability. Identical dynamics are preferred for motion in all planar directions. Therefore, spherical, spheroidal, and Mylar-shaped [55] envelopes are desirable for their symmetrical properties. Due to vertical limitations in indoor environments (ceilings), vertical maneuverability is much less necessary. As a result, planar motion is

emphasized for indoor blimps rather than vertical movement. Therefore, oblate spheroidal and Mylar-shaped envelopes are more desirable as their symmetric dynamics contribute less drag in planar motion. Finally, we chose Mylar-shaped envelopes instead of oblate spheroid envelopes due to their increased buoyancy per cubic inch and lighter weight. Mylar balloons are usually comprised of two circular sheets of inelastic film, fused together at the circumference [56]. Table 3.2 summarizes the comparison of major candidate geometries of the envelope.

In conclusion, the elimination of the tail fin provides a smoother envelope for safe indoor operation, and better maneuverability at low speeds. The choice of Mylar-shaped envelope ensures abundant buoyancy and reduces air drag for planar motion. The Mylar-shaped envelope also possesses symmetric properties including diagonal inertia, added mass, and drag matrices. This helps reduce dynamic coupling among the multiple axes.

Table 3.2: Comparison between candidate symmetrical envelope shapes

	Prolate spheroid	Sphere	Oblate spheroid	Mylar
Planar symmetry	No	Yes	Yes	Yes
Planar air drag	Medium / Low	High	Medium	Medium
Vertical air drag	Medium	Medium	High	High
Buoyancy	Low	Highest	Medium	High
Accessibility	Poor	Medium	Poor	Best

3.3.2 Omnidirectional Symmetrical Actuation

The GT-MAB features an unique symmetrical actuator configuration for holonomic planar motion that allows the thrusters to only operate in single direction. To the best of our knowledge, this configuration is the first occurrence among indoor miniature blimps.

Applications of indoor blimps prioritize multidirectional maneuverability and precise positioning. Holonomic mobility is a highly preferred feature for indoor MABs. With 3DOF motion on the planar plane, the blimp can move in any direction without steering,

and can make sharp turns in place. Moreover, with omnidirectional mobility, the blimp can keep an onboard directional sensor (such as a camera) pointed along a direction of interest regardless of translational movement. To achieve holonomic planar motion, three independent axes of thrust are required. As a consequence, the first actuator configuration in Figure 3.5, though it is widely applied among many indoor blimps including GT-MAB 1.0 for its simplicity, cannot fulfill the requirement of holonomic mobility.

The second and third configuration in Figure 3.5 add lateral actuation in addition to longitudinal thrusters. These configurations provide holonomic mobility and are applied to indoor blimps such as GT-MAB 1.5. Since the thrust directions align with the body axes, it is intuitive to allocate desired actuation to each individual motors. However, it is inevitable for motors to frequently switch directions for scenarios including attitude stabilization, station-keeping, and interacting with human. The frequent change of rotation direction reduces the lifespan of the motors, consumes energy, and increases burden to the driver circuit. Moreover, most motors and propellers are optimized for one direction. Larger thrust is usually generated when the thruster spins in the designated direction. The asymmetrical nature of the thrusters often cause difficulties in controller design, especially when the direction of the motors needs to be reversed very frequently.

Therefore, GT-MAB 2.0 uses an unique thruster configuration for symmetric actuation where only forward thrust is required for each motor. As demonstrated in the fourth configuration in Figure 3.5, there are four uni-directional thrusters forming an X-shaped configuration. Fully symmetric actuation can be achieved for the planar motion, as shown in Figure 6.21. Moreover, owing to the symmetric installation of the motors, the thruster-gondola interaction is also identical for all four actuators. Furthermore, without the need for frequently switching the direction of rotation, motors usually have higher efficiency, longer lifespan, and faster response time. The comparison between different thruster configurations is concluded in Table 3.3.

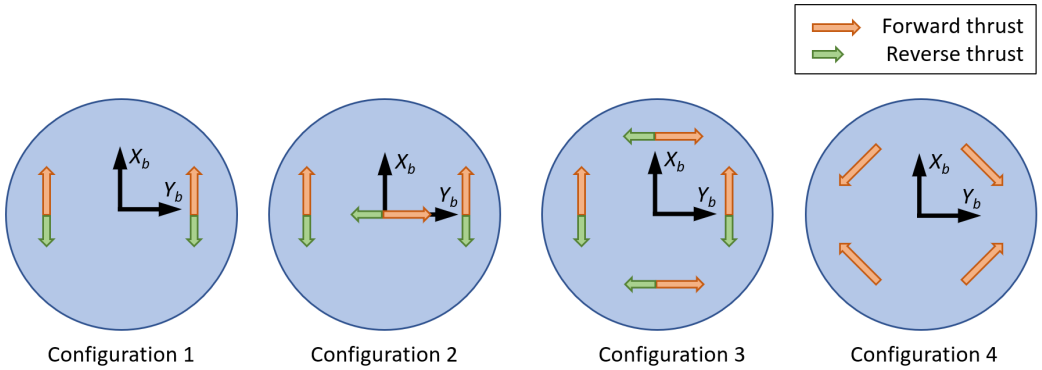

Figure 3.5: Candidate actuation configurations for indoor blimps with symmetrical envelope.

Table 3.3: Comparison between candidate actuation configurations

	Config. 1	Config. 2	Config. 3	Config. 4
Planar mobility	Nonholonomic	Holonomic	Holonomic	Holonomic
Thruster type	Bi-Dir.	Bi-Dir.	Bi-Dir.	Uni-Dir.
Symmetrical actuation	No	No	No	Yes

3.3.3 Low-latency Off-board Control Scheme

GT-MAB features an unique low-latency offboard control scheme, which allows the real-time flight controllers being implemented on the ground station instead of realized onboard. Benefits of off-board computation includes convenient accessibility to indoor localization systems, support for computationally-intensive algorithms, reduced size and power consumption, and convenience for development and post analysis.

Due to the GPS-denied environment, indoor motion capture systems are usually required for miniature autonomous blimps. A computer is typically essential to interface with such localization systems and calculate the pose of the blimp. For instance, the Optitrack system [57] used by the GT-MAB needs a high-performance computer to interface with multiple motion-capture cameras via Ethernet, and solve the pose of the blimp from the camera image stream. Therefore, implementing the flight controller on the same ground station computer allows the most convenient access and the minimum latency to the localization system. Moreover, the onboard computational power for small-sized robots includ-

ing the GT-MAB are limited due to constraints such as energy consumption and weight. As a result, computationally intensive algorithms such as model-predictive control (MPC) and computer vision, can hardly be implemented onboard. In contrast, there is no such limitations if these computations can be performed on the ground station computer. In addition, the development, debugging, and data logging are more convenient on the ground computer compared to onboard implementation. However, off-board computation poses high requirement on the communication latency between the aerial robot and the ground station. The control command computed by the ground station computer needs to be first sent to the blimp wirelessly, and then executed by the onboard electronics to drive the actuators. Chapter 6.1 has analyzed the impact of latency on the attitude control of the blimp. The results pinpointed that low latency is highly required for the fast roll and pitch dynamics of the GT-MAB. The key characteristics of both onboard and off-board computation are compared in Table 3.4.

Table 3.4: Comparison between onboard and offboard computation

	Onboard computation	Off-board computation
Size and weight	High	Low
Power consumption	High	Low
Accessibility to positioning system	Poor	Good
Support computationally intensive algorithms	Poor	Good
Convenience for algorithm and functionality development	Poor	Good
Requirement on communication latency and update rate	Low	High

The off-board control scheme of GT-MAB 2.0 is developed with the goal of low latency, high update rate, low power consumption, and good reliability. Bluetooth and Zigbee are widely used among indoor robotic platforms due to their convenience of implementation. However, the latency of these communication technologies is usually over 15ms, making

them less desirable for off-board control. Therefore, we minimize the length of the control command and incorporate a basic radio-frequency (RF) transceiver without a heavy protocol stack for lower latency. As shown in Figure 3.6, it takes an average of 387us to update the terminal voltages of the onboard thruters, after the controller outputs are received by the ground station transceiver.

As demonstrated in Figure 3.7, the blimp functions like a transponder for the convenience of time synchronization and fail-safe protection. Upon the reception of the control command from the ground station, the onboard electronics immediately executes the command and sends sensor data back. Zero-order-hold is implemented in case of corrupted or missing packet. All thrusters on the blimp will be turned off for safety if no valid packet is received for more than half a second. To reduce potential interference, the frequency range of the blimp is selected aside from that of WiFi or Bluetooth devices. Shown in the same figure, the bi-directional communication between the blimp and the ground station supports update rate up to 2000Hz. When operated at maximum update rate with transmission power of +8dBm, the overall power consumption of the gondola is only less than 50mW. With low latency, high update rate, and low power consumption, the proposed off-board control scheme can well fulfil the requirements of GT-MAB, as well as many other robotic platforms.

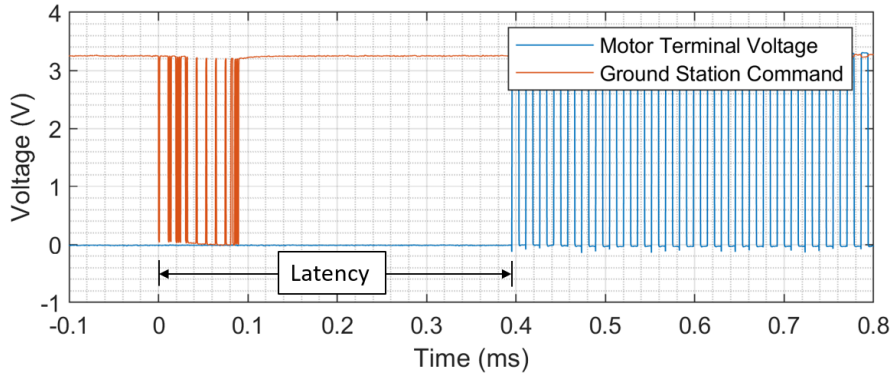

Figure 3.6: Waveform of the control command signal received by the ground station and and the corresponding motor terminal voltage. The waveform demonstrates low-latency feature of the off-board control scheme of GT-MAB 2.0.

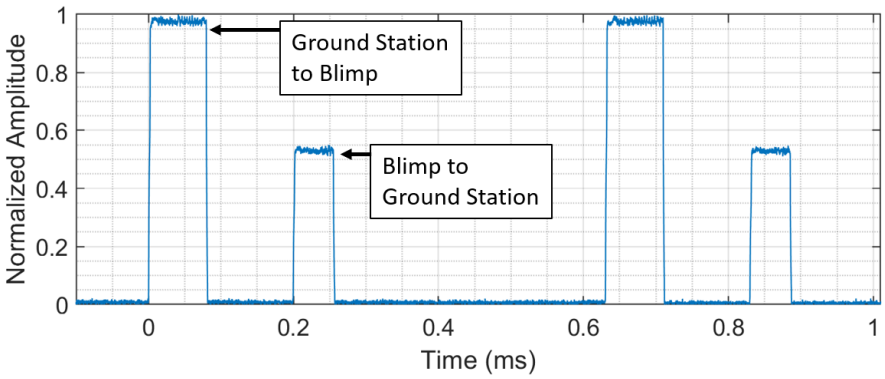

Figure 3.7: Wireless data packets between the blimp and the ground station. Two bi-directional communications can be accomplished within 1ms.

3.3.4 Light-weight Onboard Electronics Suite

The onboard electronics suite of GT-MAB 2.0 includes the core electronics board and the power module. These devices are designed with emphasis on compactness to reserve payload for actuators, battery, structure, and task-related devices such as sensors. The weights of the components are listed in Table 3.5.

The core electronics board is a compact integration of all essential functionalities of the GT-MAB. Components including an ARM processor, drivers for six motors, voltage regulator, multi-functional connector, wireless transceiver and antenna are integrated. The device also features high power density. The maximum power output is 50W, which is abundant for a wide range of miniature robots. As shown in Figure 3.8, the core electronics board has a compact form factor with area about 2 cm^2 and weight less than half a gram, making it the lightest design among devices with the same functionality.

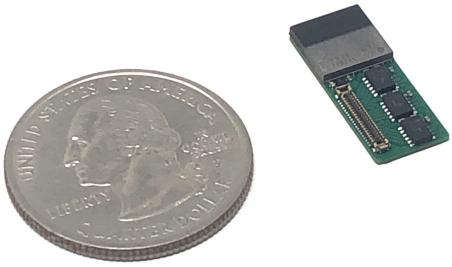

Figure 3.8: Core electronics board of GT-MAB 2.0. The device has area about 2 cm^2 and weight less than half a gram.

The power module provides constant voltage to the entire gondola despite the varying battery voltage over time. We developed two versions with power output of 10 and 20 watts. Photos of both devices are shown in Figure 3.4. The power module with 10W output is abundant for most flight scenarios and task payloads. The one with 20W output is developed for high-power task payloads and extreme operating conditions. DC-DC converters with high switching frequency are incorporated for high efficiency and reduced weight.

Table 3.5: Weights of the major onboard electronic components

Component	Core electronics board	Power module 10W	Power module 20W
Weight	0.49 grams	0.63 grams *	2.60 grams *

*Weights of the power modules do not include the power extension cable.

3.3.5 Improved Localization

Optical motion capture systems such as Vicon and Optitrack are usually incorporated to obtain the position and attitude of indoor miniature blimps in the GPS-denied environment. Such systems require infrared lamps to illuminate the capture volume, ensuring the visibility of the envelope-mounted passive reflective markers to the motion capture cameras. However, as shown in Figure 3.9, the undesired reflection from the surface of the envelope is much brighter than that from the passive markers. This undesirable reflection causes interference to the motion capture system.

We developed an active marker that eliminates the requirement for external infrared illumination [58]. With the active marker, as demonstrated in Figure 3.9, the interference due to the excessive reflection from the external illumination is resolved. Weight of the active marker is only approximately one gram. To the best of our knowledge, this active marker is the lightest implementation among such devices, and is the only design that accommodates the limited payload capacity of indoor miniature blimps.

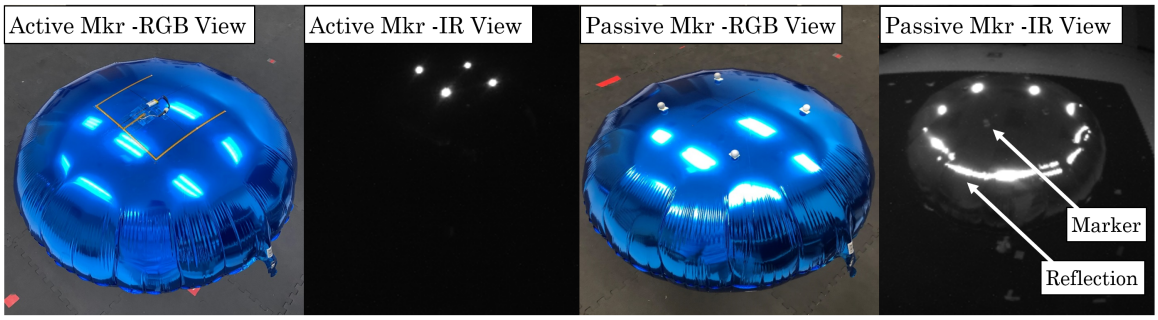

Figure 3.9: Comparison between active and passive motion capture markers.

3.3.6 Safety, Convenience and Expandability

GT-MAB is safe to fly indoors, and causes no threat to human and the surroundings even with collisions. As a result, no safety netting is necessary for flight in human-occupied environments, unlike quadcopters. The smooth helium-filled envelope provides a natural cushion for collisions. With the same density as the surrounding air, the blimp will safely descend in the event that the battery is fully depleted. As shown in Figure 3.10, all the propellers are protected by ducts. Moreover, all thrusters of the GT-MAB will be turned off if no valid command is received for over half a second.

As demonstrated in Figure 3.10, the gondola of GT-MAB features a modular design. The core electronics board integrates all essential functionalities, while the gondola chassis only provides mechanical support and basic electrical connections. The two parts can be conveniently mated with a single multipurpose connector. The modular design simplifies the assembly, maintenance, and future modification of the GT-MAB.

GT-MAB features outstanding expandability to a wide range of task payloads. Predecessors of GT-MAB 2.0 have been integrated with sensors including camera, inertial measurement unit (IMU), ultrasonic and laser range finder, ultra-wide-band (UWB) localization, anemometer, and light intensity meter. Devices including dot matrix display, airdrop actuator, and wireless charger are also tested. As illustrated in Figure 3.11, GT-MAB 2.0 enhances the expandability by allowing payload devices to be connected to an independent payload hub in addition to be directly integrated with the core electronics.

The existence of the payload hub decouples the development for payload integration, and allows wider range of devices to be installed.

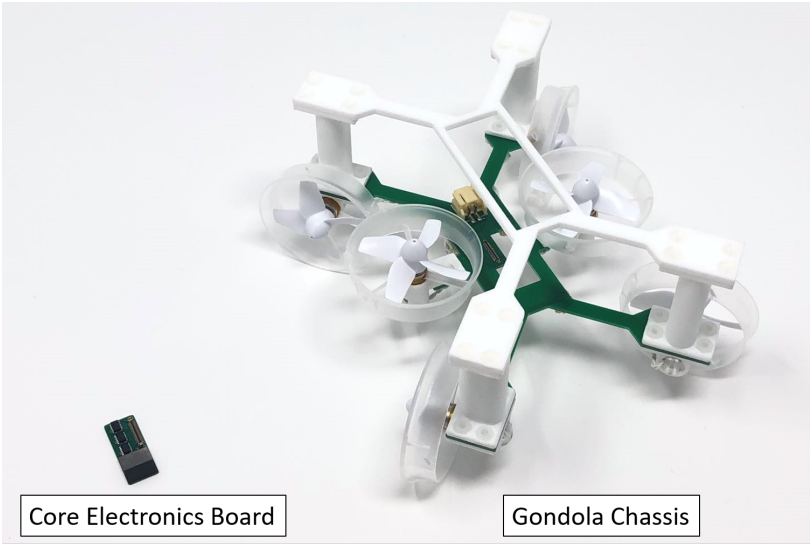

Figure 3.10: The gondola of GT-MAB 2.0 consists of a compact core electronics board and a mechanical chassis.

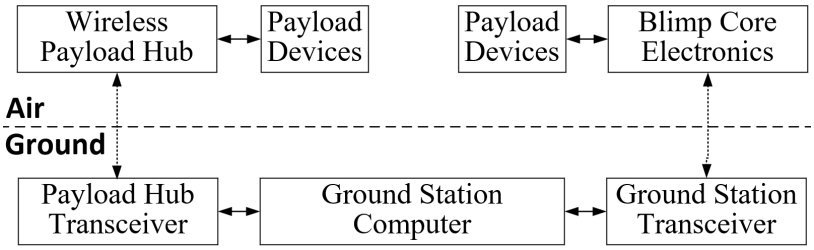

Figure 3.11: Functional block diagram of incorporating the wireless payload hub for enhanced expandability of GT-MAB 2.0.

CHAPTER 4

WAYPOINT NAVIGATION WITHOUT SWING STABILITZATION

In this chapter, we discuss the modeling and control of GT-MAB without swing stabilization feature. Non-holonomic waypoint navigation is achieved with GT-MAB 1.0. For the convenience of future comparison, we refer to this flight control system as FCS 1.0.

4.1 General Hypotheses

The kinematic and dynamic model of GT-MAB are derived based on the following assumptions. These assumptions are justified from the unique design and the indoor operating environments of miniature autonomous blimps.

Assumption 1. *The blimp operates at low velocity, usually less than half meter per second.*

Remark 1. *Most indoor environment has limited volume. Therefore, the station-holding capability and agile mobility over short distance is emphasized rather than high-speed cruising. Moreover, many applications of indoor blimps such as inspection and human-robot interaction require low speed but highly stable flight.*

Assumption 2. *Motor thrust is the sole cause of the movement of the GT-MAB*

Remark 2. *Control surfaces such as elevator and rudder usually have low efficiency under slow-speed flight and can cause damage in human-occupied indoor environment. Therefore, GT-MAB has fin-less design and the actuation of the blimp is solely from the thrusters. Moreover, since miniatures blimps usually operate in enclosed indoor spaces, we assume there is no disturbance from the environment.*

Assumption 3. *The envelope is considered as rigid body during flight.*

Remark 3. *The shape of the envelope is kept by the pressure of the internal helium gas. Owing to the slow-flying nature of indoor blimps and the non-elastic film incorporated by the GT-MAB, the deformation of the envelope is neglectably small. Thus, we assume the shape of the envelope is consistent during flight.*

Assumption 4. *The density of the blimp is identical to that of the surrounding air, and stays consistent during each flight.*

Remark 4. *Ballast weight will be added to fine trim the blimp before each flight. The ballasting process ensures the blimp can stay aloft without motor action. Therefore, the density of GT-MAB can be assumed to be equal to the surrounding air after ballasting.*

Due to the low molar mass of the internal helium gas, the density of GT-MAB tends to become lower with elevated temperature and vice versa. However, owing to the non-elastic envelope and small temperature variance in indoor environment, such density change can be omitted. Moreover, the metal coating on the envelope reduces the gas permeability. Therefore, the density change due to gas leakage is neglectable within the flight duration of indoor miniature blimps.

Assumption 5. *The center of buoyancy (CB) is at the center of volume (CV) of the envelope. Both CB and the center-of-gravity (CG) are on the vertical axis of the blimp.*

Remark 5. *Given that the envelope dominates the volume of GT-MAB, we can assume that the CV of the envelope is the CB of the entire robot. The envelope features symmetrical saucer shape, which makes the CB located on the vertical axis of the blimp. Moreover, the gondola and other components of GT-MAB are carefully installed around the Z-axis of the blimp. Therefore, both CB and CG are located on the vertical axis of GT-MAB.*

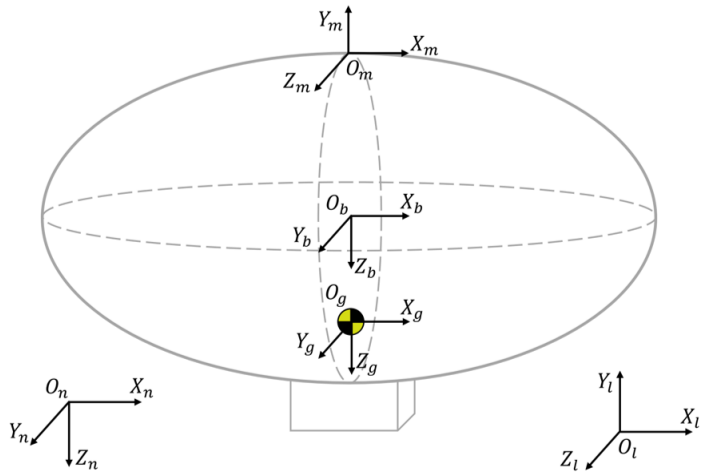

Figure 4.1: Illustration of the coordinate frames.

4.2 Kinematics and Coordinate Frames

4.2.1 Choice of Coordinate Frames

Figure 4.1 shows the definition of the inertial frame, the coordinates of the motion capture system, and the body-fixed frames that are separately attached at the center of buoyancy, center of gravity, and the localization markers. The inertial frame is denoted by $\{n\}$ with north-east-down (NED) convention. Given the fact that indoor blimps always operate in confined environments at low speed, we apply flat-earth approximation and neglect the movement of the earth. Positioning devices usually have different coordinate systems other than $\{n\}$. Therefore $\{l\}$ is defined to represent the frames used in the motion capture system. The definition of $\{l\}$ will help convert the pose of the blimp to $\{n\}$. Given that most localization devices have fixed installation, we assume $\{l\}$ is also earth-fixed. In this thesis, we use the OptiTrack system with Y-up convention. For simplicity, O_n is defined at the same position as O_l, and the x-axes of both frames are aligned. The body frame $\{b\}$ is established at the CB of GT-MAB, which is the geometric center of the envelope. We use forward-right-down convention for $\{b\}$. Similarly, the frame $\{g\}$ is attached at the CG position and is parallel to $\{b\}$. The localization markers are installed at the top of the envelope for the best visibility to the ceiling-mounted motion tracking system. The frame

attached at the marker position is denoted as $\{m\}$. The marker frame has the same Y-up convention as $\{l\}$ for the convenience of pose calibration in the motion capture system.

4.2.2 Kinematics

The pose of GT-MAB is denoted as $\boldsymbol{\eta}_{b/n}^{n} = [\boldsymbol{p}_{b/n}^{n\top}, \boldsymbol{\Theta}_{nb}^{\top}]^{\top}$, which is the pose of $\{b\}$ with respect to $\{n\}$ expressed in the inertial frame. $\boldsymbol{p}_{b/n}^{n} \in \mathbb{R}^3$ and $\boldsymbol{\Theta}_{nb} \in \mathbb{S}^3$ represent the position and orientation separately. The instantaneous velocity of the blimp decomposed in the body frame $\{b\}$ is described by $\boldsymbol{\nu}_{b/n}^{b} = [\boldsymbol{v}_{b/n}^{b\top}, \boldsymbol{\omega}_{b/n}^{b\top}]^{\top}$, where $\boldsymbol{v}_{b/n}^{b} \in \mathbb{R}^3$ and $\boldsymbol{\omega}_{b/n}^{b} \in \mathbb{R}^3$ are the linear and angular velocities. From [59], the relationship between $\boldsymbol{\nu}_{b/n}^{b}$ and the rate of change of $\boldsymbol{\eta}_{b/n}^{n}$ is given by:

$$\dot{\boldsymbol{\eta}}_{b/n}^{n} = \begin{bmatrix} \dot{\boldsymbol{p}}_{b/n}^{n} \\ \dot{\boldsymbol{\Theta}}_{nb} \end{bmatrix} = \begin{bmatrix} \boldsymbol{R}_{b}^{n}(\boldsymbol{\Theta}_{nb}) & \boldsymbol{0}_{3\times3} \\ \boldsymbol{0}_{3\times3} & \boldsymbol{T}_{\Theta}(\boldsymbol{\Theta}_{nb}) \end{bmatrix} \begin{bmatrix} \boldsymbol{v}_{b/n}^{b} \\ \boldsymbol{\omega}_{b/n}^{b} \end{bmatrix} = \boldsymbol{J}_{\Theta}(\boldsymbol{\eta}_{b/n}^{n})\boldsymbol{\nu}_{b/n}^{b}, \tag{4.1}$$

where $\boldsymbol{R}_{b}^{n}(\boldsymbol{\Theta}_{nb})$ is the rotation matrix. $\boldsymbol{\Theta}_{nb} = [\phi, \theta, \psi]^{\top}$, and ϕ, θ, ψ are the Euler angles between $\{b\}$ and $\{n\}$. With the simplified notation $c\cdot = \cos(\cdot)$, $s\cdot = \sin(\cdot)$, and $t\cdot = \tan(\cdot)$, $\boldsymbol{R}_{b}^{n}(\boldsymbol{\Theta}_{nb})$ has the form of:

$$\boldsymbol{R}_{b}^{n}(\boldsymbol{\Theta}_{nb}) = \begin{bmatrix} \mathrm{c}\psi\mathrm{c}\theta & -\mathrm{s}\psi\mathrm{c}\phi + \mathrm{c}\psi\mathrm{s}\theta\mathrm{s}\phi & \mathrm{s}\psi\mathrm{s}\phi + \mathrm{c}\psi\mathrm{s}\theta\mathrm{c}\phi \\ \mathrm{s}\psi\mathrm{c}\theta & \mathrm{c}\psi\mathrm{c}\phi + \mathrm{s}\psi\mathrm{s}\theta\mathrm{s}\phi & -\mathrm{c}\psi\mathrm{s}\phi + \mathrm{s}\psi\mathrm{s}\theta\mathrm{c}\phi \\ -\mathrm{s}\theta & \mathrm{c}\theta\mathrm{s}\phi & \mathrm{c}\theta\mathrm{c}\phi \end{bmatrix}. \tag{4.2}$$

The term $\boldsymbol{T}_{\Theta}(\boldsymbol{\Theta}_{nb})$ in Eq. (4.1) can be represented as:

$$\boldsymbol{T}_{\Theta}(\boldsymbol{\Theta}_{nb}) = \begin{bmatrix} 1 & 0 & -\mathrm{s}\theta \\ 0 & \mathrm{c}\phi & \mathrm{s}\phi\mathrm{c}\theta \\ 0 & -\mathrm{s}\phi & \mathrm{c}\phi\mathrm{c}\theta \end{bmatrix}^{-1} = \begin{bmatrix} 1 & \mathrm{s}\phi\mathrm{t}\theta & \mathrm{c}\phi\mathrm{t}\theta \\ 0 & \mathrm{c}\phi & -\mathrm{s}\phi \\ 0 & s\phi/\mathrm{c}\theta & \mathrm{c}\phi/\mathrm{c}\theta \end{bmatrix}. \tag{4.3}$$

4.3 6-DOF Motion Model at CG

The position of the blimp is determined in a world-fixed inertial coordinate frame. But it is more convenient to represent the linear and angular velocities in a body-fixed coordinate frame, as seen in Figure 4.1. We follow the established procedures in the literature [25, 60] to derive the dynamic model equations.

Let $\boldsymbol{\tau}^g = [\boldsymbol{f}^{g\top}, \boldsymbol{m}^{g\top}]^\top = [f_x^g, 0, f_z^b, 0, 0, \tau_z^g]^\top$ represent the translational forces and steering torque generated by the thrusters on the blimp. Sideway thrust is not available on the early prototype of GT-MAB. The torque in pitch direction is also omitted due to the absence of attitude control.

Let $\boldsymbol{F}^g = [F_x^g, F_y^g, F_z^g]^\top$ be a vector representing the gravitational forces, the buoyancy forces, and other aerodynamic forces acting on the blimp in the body-fixed frame. Let $\boldsymbol{M}^g = [M_x^g, M_y^g, M_z^g]^\top$ be a vector representing all the external moments exerted on the blimp except for those generated by the propellers. Let m be the total mass of the blimp. Here we assume the added mass is identical for movement in all directions. Then we let

$$\boldsymbol{I}^{CG} = \begin{bmatrix} I_x^{CG} & -I_{xy}^{CG} & -I_{xz}^{CG} \\ -I_{yx}^{CG} & I_y^{CG} & -I_{yz}^{CG} \\ -I_{zx}^{CG} & -I_{zy}^{CG} & I_z^{CG} \end{bmatrix}$$

be the total inertia matrix about the center of gravity. The 6-DOF equations of motion of the blimp can be derived as

$$m(\dot{\boldsymbol{v}}_{g/n}^b + \boldsymbol{\omega}_{g/n}^b \times \boldsymbol{v}_{g/n}^b) = \boldsymbol{F}^g + \boldsymbol{f}^g \tag{4.4}$$

$$\boldsymbol{I}^{CG}\dot{\boldsymbol{\omega}}_{g/n}^b + \boldsymbol{\omega}_{g/n}^b \times (\boldsymbol{I}^{CG}\boldsymbol{\omega}_{g/n}^b) = \boldsymbol{M}^g + \boldsymbol{m}^g. \tag{4.5}$$

4.4 Motion Primitives

The 6-DOF model described by Equations (4.4) and (4.5) is nonlinear and coupled. A general controller design for such system is difficult, especially when some of the parameters of the model are unknown. Therefore, we need to find simplified models to achieve controllable flight. Here we decouple the movement of GT-MAB into three motion primitives:

1. Maintaining speed. The blimp should be able to maintain a desired constant speed along its longitudinal direction while having zero vertical speed, and zero steering velocity, e.g.,

$$\boldsymbol{v}_{g/n}^{b} = [v_{x,g/n,0}^{b}, 0, 0]^{\top}, \boldsymbol{\omega}_{g/n}^{b} = [0, 0, 0]^{\top}. \tag{4.6}$$

2. Changing altitude. The blimp should be able to ascend or descend to a desired height, while maintaining zero forward speed and zero steering velocity e.g.,

$$\boldsymbol{v}_{g/n}^{b} = [0, 0, v_{z,g/n}^{b}]^{\top}, \boldsymbol{\omega}_{g/n}^{b} = [0, 0, 0]^{\top}. \tag{4.7}$$

3. Changing orientation. The blimp should be able to spin in place so that its yaw angle can be stabilized at any desired value, while maintaining zero forward speed, and zero vertical speed e.g.,

$$\boldsymbol{v}_{g/n}^{b} = [0, 0, 0]^{\top}, \boldsymbol{\omega}_{g/n}^{b} = [0, 0, \omega_{z,g/n}^{b}]^{\top}. \tag{4.8}$$

These motion primitives can be combined to achieve stable flights that allow the blimp to move in 3D space. The design goals for the autopilot are now reduced to stabilizing these three motion primitives.

4.5 Model Reduction

In order to simplify the dynamics, we make the following assumptions that hold for all three motion primitives.

Assumption 1. *The roll angle and the roll angular velocity, the pitch angle and the pitch angular velocity, and the side-slipping velocity are negligibly small during the transient phase of the flight and zero during the steady-state flight e.g.,*

$$\begin{aligned} \boldsymbol{\Theta}_{ng} &= \dot{\boldsymbol{\Theta}}_{ng} = [0, 0, \theta]^\top \\ \boldsymbol{v}^b_{g/n} &= [v^b_{x,g/n}, 0, v^b_{z,g/n}]^\top. \end{aligned} \tag{4.9}$$

Remark 1. *This assumption is justified because the GT-MAB is under the influence from the restoring forces due to its bottom-heavy design. The restoring forces induced by gravity and buoyancy effectively damp out roll and pitch motion. Since the blimp is very light with a large envelope, the side-slipping velocity of the blimp will vanish quickly due to air drag when the blimp flies forward. We understand that a sideway force will be generated by the term $\boldsymbol{\omega}^b_{g/n} \times \boldsymbol{v}^b_{g/n}$ while the blimp is spinning and flying forward at the same time. However, this term is viewed as a vanishing disturbance force that is damped out by air drag. The force can also be ignored under the assumption that the spinning speed is almost zero during forward flight, and the forward speed is almost zero during the spinning motion.*

Therefore, with roll and pitch angles and their rate of change assumed to be zero, the angular velocities in the body-fixed frame can be found as:

$$\boldsymbol{\omega}^b_{g/n} = \boldsymbol{T}^{-1}_{\Theta}(\boldsymbol{\Theta}_{ng})\dot{\boldsymbol{\Theta}}_{ng} = \begin{bmatrix} 1 & 0 & 0 \\ 0 & 1 & 0 \\ 0 & 0 & 1 \end{bmatrix}^{-1} \begin{bmatrix} \dot{0} \\ 0 \\ \psi \end{bmatrix} = \begin{bmatrix} 0 \\ 0 \\ \dot{\psi} \end{bmatrix}. \tag{4.10}$$

Remark 2. *Due to the symmetry of the blimp envelope, the inertia matrix $\boldsymbol{I}^{CG}$ can be assumed as diagonal. One advantage of the "saucer-shaped" envelope is that $I^{CG}_x = I^{CG}_y$,*

which further simplifies the dynamics. The term $\boldsymbol{\omega}^b_{g/n} \times (\boldsymbol{I}^{CG}\boldsymbol{\omega}^b_{g/n})$ *in Eq.* (4.4) *does not generate rotation moments if the roll and pitch angular velocities are zero. In the case when roll and pitch moments are not zero, the contribution from the term* $\boldsymbol{\omega}^b_{g/n} \times (\boldsymbol{I}^{CG}\boldsymbol{\omega}^b_{g/n})$ *to the roll and pitch moments are also small allowing them to be easily damped out by the restoring force from the gravity.*

Therefore, the 6-DOF motion model in Equations (4.4) and (4.5) can be simplified as:

$$\begin{aligned} m\dot{v}^b_{x,g/n} &= f^g_x + F^g_x \\ m\dot{v}^b_{z,g/n} &= f^g_z + F^g_z \\ I^{CG}_z \dot{\omega}^b_{z,g/n} &= \tau^g_z + M^g_z. \end{aligned} \tag{4.11}$$

Remark 3. *Note that the motion models described in Eq.* (4.11) *are still nonlinear because the external forces* F^g_x, F^g_z *and the external moment* M^g_z *include the forces and moments generated by the gravity and the ambient air. These forces are nonlinear functions of accelerations and velocities and are quite difficult to model. This is different from the modeling of teh quad-rotors and multi-copters with powerful thrusters, which generate forces* f^g_x, f^g_z *and moment* τ^g_z *at least a magnitude larger than the influences from ambient air, and allows* F^g_x, F^g_z *and* M^g_z *to be ignored. For the blimp, because of the relatively large envelope and the low-power thrusters, the aerodynamics need to be considered, which is very similar to the modeling of underwater vehicles.*

4.6 System Identification

The simplified models can be further linearized for each motion primitive. For flight at constant heading, we linearize the model around a desired forward speed, zero vertical speed, and zero yaw angular speed. For a change of altitude, we linearize the model around the desired height, zero forward speed and zero yaw angular speed. For a change of orientation, we linearize the model around a desired yaw angle, zero forward speed, and zero

vertical speed. These models can be viewed as open-loop plants. The model for maintaining forward speed has f_x^g as its input and the forward speed $v_{x,g/n}^b$ as its output. The model for changing altitude has f_z^g as its input and the height in inertial frame, $p_{z,g/n}^n$, as its output. Since $p_{z,g/n}^n$ is positive downward, the height of the blimp has negative value. And the model for changing orientation has the torque τ_z^g as its input and the yaw angle ψ as its output. For each motion primitive, we commanded GT-MAB's motors to a certain throttle to excite the open-loop plant. This experiment is repeated for multiple times with different throttle levels. With MATLAB system identification toolbox [61], the transfer function of each motion primitive is identified as:

$$\begin{aligned} P_1(s) &= \frac{0.9624s^2 + 0.5787s + 12.26}{s^3 + 0.7634s^2 + 14.62s + 4.691} e^{-0.17s} \\ P_2(s) &= \frac{1.9535}{s^2 + 0.1267s} e^{-0.17s} \\ P_3(s) &= \frac{10.9365}{s^2 + 0.1855s} e^{-0.17s}. \end{aligned} \tag{4.12}$$

We use the first order Pade approximation to approximate the time delays in the transfer functions. The Pade approximation $e^{-\tau s} = \frac{1}{\tau s+1}$ [62] leads to approximated open loop transfer functions. The transfer functions is approximated by:

$$\begin{aligned} P_1(s) &= \frac{5.6612s^2 + 3.4041s + 72.1176}{s^4 + 6.6471s^3 + 19.1118s^2 + 90.7059s + 27.5941} \\ P_2(s) &= \frac{11.4912}{s^3 + 6.0088s^2 + 0.7453s} \\ P_3(s) &= \frac{64.3324}{s^3 + 6.0676s^2 + 1.0912s}. \end{aligned} \tag{4.13}$$

The locations of open loop poles and zeros of the transfer function $P_1(s)$ are plotted in blue in Figure 4.2. For transfer functions $P_1(s)$, $P_2(s)$ and $P_3(s)$, there are no poles on the right half of the complex plane, but there are poles on the imaginary axis or the origin. This implies that forward speed and orientation systems are marginally stable. Therefore, the desired speed, height, and yaw angle can not be achieved by open loop control.

In particular, the forward speed model $P_1(s)$ has one pair of complex conjugate poles very close to the imaginary axis, which are generated by the coupling between the forward motion and pitch oscillation that are ignored when deriving the theoretical model. These poles will lead to very slowly vanishing oscillatory modes in the pitch angle when the blimp flies forward.

4.7 Controller Design

Based on the identified linear input-output motion models represented by Eq. (4.13), we design controllers to achieve the three motion primitives: maintaining speed, changing altitude, and changing orientation. The goal is to make the three closed-loop systems asymptotically stable, and to compensate for the oscillations in the speed system.

The three controllers are designed as the PID controllers. The forward speed controller uses $v^b_{x,g/n}$ as feedback and f^g_x as control input. The altitude controller uses $p^n_{z,g/n}$ as feedback and use f^g_z as the control. The heading controller uses ψ as feedback and τ^g_z as the control. The PID gains for the controllers are tuned based on the identified open-loop transfer functions. The closed-loop transfer functions under PID controllers are:

$$\begin{aligned} G_1(s) &= \frac{6.1988s^3 + 9.9265s^2 + 82.6865s + 78.9594}{s^5 + 6.6459s^4 + 25.3141s^3 + 100.6424s^2 + 110.2788s + 78.9594} \\ G_2(s) &= \frac{7.5382s + 0.1}{s^4 + 6.0088s^3 + 9.1935s^2 + 7.5382s + 0.1} \\ G_3(s) &= \frac{12.5771}{s^3 + 6.0676s^2 + 13.4429s + 12.5771}. \end{aligned} \tag{4.14}$$

where $G_1(s)$, $G_2(s)$ and $G_3(s)$ are closed-loop transfer function of speed, altitude, and yaw angle separately.

For two closed-loop transfer functions, all poles are on the left half plane, hence all the closed-loop transfer functions are asymptotically stable. Furthermore, there is no steady-state errors under step function input. The poles and zeros of the closed-loop transfer function $G_1(s)$ are plotted in red in Figure 4.2. The oscillatory complex poles in $P_1(s)$ are

compensated by a pair of complex conjugate zeros, which help reduce the oscillation.

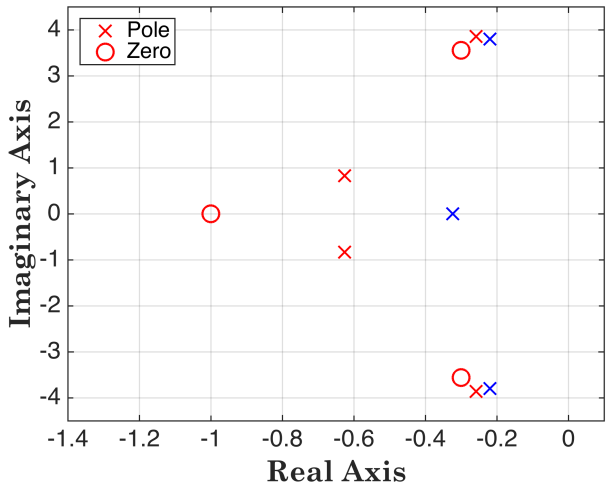

Figure 4.2: Poles and zeros of the open loop transfer function $P_1(s)$ and the closed-loop transfer function $G_1(s)$ for forward speed control. Blue markers represent poles and zeros of the open-loop transfer function. Red markers represent poles and zeros of the closed-loop transfer function. One one open-loop pole located at $(-5.88, 0)$ and one closed-loop pole located at $(-4.88, 0)$ are omitted in the figure.

Figure 4.3 shows the comparison between the simulated and measured closed-loop step response of each motion primitive. The altitude and heading controller perform similarly to the simulated response and has good rise and settling time. However, small oscillation is observed in the speed controller, due to the lack of direct control input for the pitch motion.

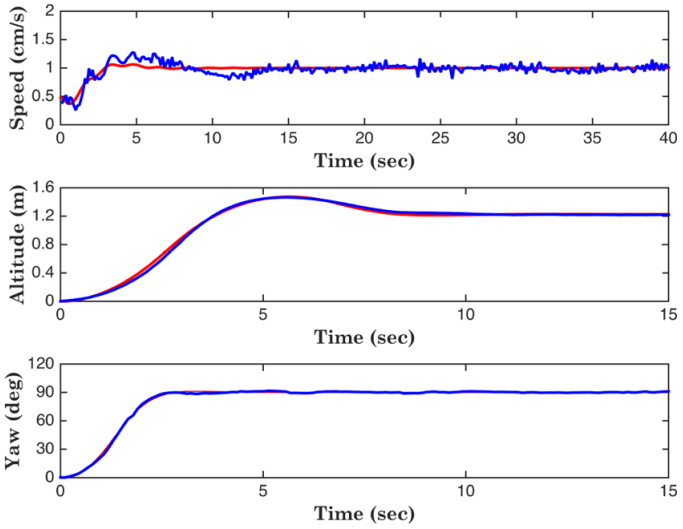

Figure 4.3: Simulated (red) and measured (blue) closed-loop step response of the motion primitives.

4.8 Waypoint Navigation

The motion primitives are then combined to implement a waypoint following behavior for the blimp to reach a location specified as a waypoint in 3D space. The altitude controller will control the blimp to reach the desired altitude where the waypoint is located, the heading controller will control the heading of the blimp to always point towards the waypoint. A distance controller will use the distance to the waypoint as feedback and f_x^g as control input. The plant model will be $\frac{P_1(s)}{s}$. Again, a PID controller is designed so that the blimp will slow down when it gets close to the waypoint. The distance, altitude, and heading controller work together to control the blimp to reach the desired waypoint in 3D space.

A sequence of waypoints can be specified to define a piecewise linear path for the blimp to follow. When the blimp comes within a specified distance (i.e., 0.4 meters) of a waypoint, the blimp will then navigate towards the next waypoint in the sequence. Figure 4.4 demonstrates that GT-MAB follows a set of waypoints, achieving a spiral trajectory. The waypoints can also be updated in real time, which helps applications such as which helps applications such as source-seeking, adaptive sampling and swarming.

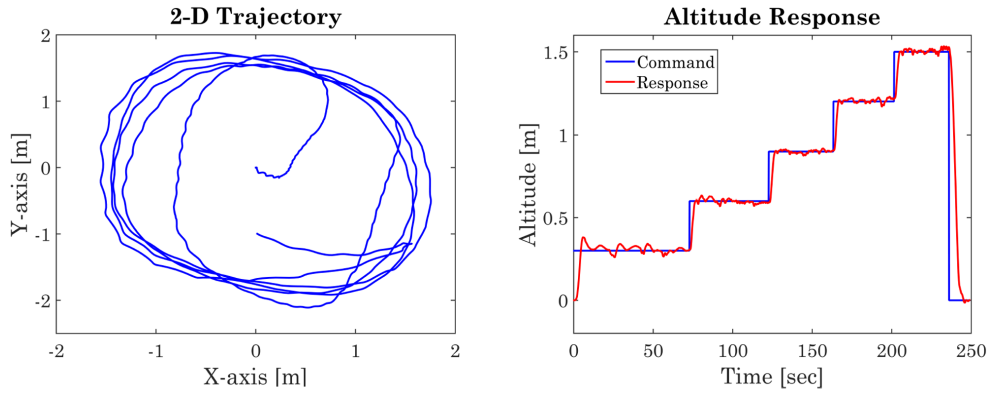

Figure 4.4: GT-MAB follows waypoints in 3D space with FCS 1.0. The blimp started at the origin, and visited waypoints with horizontal positions of (1.2, 1.2), (-1,1.2), (-1,-1.2), and (1.2,-1.2), and height of 0.3, 0.6, 0.9, and 1.2 meters.

CHAPTER 5
MODELING AND IDENTIFICATION OF SWING OSCILLATION OF GT-MAB

5.1 Motion Model for Swing Oscillation during Hovering Flight

The modeling and control effort presented in Chapter 4 decomposes the movements of GT-MAB into a set of motion primitives. This decoupled modeling and control approach has successfully supported many applications of GT-MAB including 3D field mapping [20, 36], human-robot interaction [9, 19], and testbed for deep-learning-based localization and multi-agent path planning [52, 53].

However, this decoupled modeling and control approach does not investigate all of the rotational dynamics, namely the pitch and roll movement of GT-MAB. As a consequence, lateral and longitudinal oscillation is often observed while the GT-MAB is in flight. This undesirable oscillation has impacts on many applications of GT-MAB. The onboard sensors usually have directionality, and oscillation could cause inaccurate readings. Moreover, the quality of the video stream from the onboard camera is affected by the oscillatory movement. Mechanical gimbals can be installed on aerial robots to stabilize the sensors [63], but such a device may exceed the payload capacity of indoor miniature blimps. Besides the interference to the sensors, the oscillation consumes more energy and might cause people to feel less comfortable interacting with the robot. Therefore, it is crucial to study the dynamic model of the swing oscillation, and design controllers to reduce this undesirable motion.

In this section, we extend the existing efforts by identifying the rotation-related dynamics of GT-MAB through swing motion. A nonlinear pendulum-like grey box model is constructed for the swing motion to identify the parameters. Physical measurements, computer-aided design (CAD) software, and system identification experiments are used to

obtain the parameters of the grey box model. The pendulum-like grey box model is linearized with identified parameters for controller design. The linearized dynamics model is then validated with experimental data.

The swing oscillation is a shared issue among indoor miniature blimps. For most indoor blimps such as [37], the center of gravity is located below the center of buoyancy (CB) for better stability [20]. Moreover, the thrusters are usually installed beneath the envelope for weight reduction. As a consequence, the undesired pitching or rolling torque, and thus swing oscillation is inevitable once the thrusters are on. Therefore, the identification methods discussed in this section could be applied to other indoor miniature blimps.

5.1.1 Model Construction

We first recall the 6-DOF motion model of GT-MAB from Chapter 4,

$$m(\dot{\boldsymbol{v}}^b_{g/n} + \boldsymbol{\omega}^b_{g/n} \times \boldsymbol{v}^b_{g/n}) = \boldsymbol{F}^g + \boldsymbol{f}^g \tag{5.1}$$

$$\boldsymbol{I}^{CG}\dot{\boldsymbol{\omega}}^b_{g/n} + \boldsymbol{\omega}^b_{g/n} \times (\boldsymbol{I}^{CG}\boldsymbol{\omega}^b_{g/n}) = \boldsymbol{M}^g + \boldsymbol{m}^g. \tag{5.2}$$

This motion model is nonlinear and coupled, which is hard to identify the parameters without simplification. Therefore, we make the following practical assumptions that holds for the hovering flight of GT-MAB.

Assumption 1. *The center of gravity of GT-MAB is the pivot of the swing oscillation. the translational velocity at CG in the inertial frame is zero during hovering flight. e.g.,*

$$\dot{\boldsymbol{p}}^n_{g/n} = [0, 0, 0]^\top. \tag{5.3}$$

Remark 1. *Due to effects such as added mass, the pivot of rotation could have slight deviation from the CG position. However, they are relatively small compare to the rigid-body mass of the blimp. Therefore, CG position can be approximated as the pivot of the*

oscillation. Thus, while the blimp is hovering, the CG position remains constant in the inertial frame.

Assumption 2. *The dynamics of the roll and pitch movements are independent*

Remark 2. *With the diagonal inertia matrix $\boldsymbol{I}^{CG}$, the roll and pitch dynamics described in Eq.* (5.2) *can be found as:*

$$\begin{aligned} I_x^{CG}\dot{\omega}_{x,g/n}^b + I_z^{CG}\omega_{y,g/n}^b\omega_{z,g/n}^b - I_y^{CG}\omega_{y,g/n}^b\omega_{z,g/n}^b &= M_x^g + m_x^g \\ I_y^{CG}\dot{\omega}_{y,g/n}^b + I_x^{CG}\omega_{x,g/n}^b\omega_{z,g/n}^b - I_z^{CG}\omega_{x,g/n}^b\omega_{z,g/n}^b &= M_y^g + m_y^g. \end{aligned} \tag{5.4}$$

Given the heading of GT-MAB is usually constant during station-keeping flight, we assume $\omega_{z,g/n}^b = 0$. Therefore, we get independent roll and pitch dynamics during hovering:

$$\begin{aligned} I_x^{CG}\dot{\omega}_{x,g/n}^b &= M_x^g + m_x^g \\ I_y^{CG}\dot{\omega}_{y,g/n}^b &= M_y^g + m_y^g. \end{aligned} \tag{5.5}$$

Due to the symmetric design of GT-MAB, pitching and rolling dynamics of the robot are almost identical. Therefore the investigation of the swing motion can be simplified as studying the pitching oscillation. With $\boldsymbol{\Theta}_{ng} = [0, \theta, 0]^\top$, Eq. (4.2) and Eq. (4.3) can be simplified as:

$$\boldsymbol{R}_g^n(\boldsymbol{\Theta_{ng}}) = \begin{bmatrix} \mathrm{c}\theta & 0 & \mathrm{s}\theta \\ 0 & 1 & 0 \\ -\mathrm{s}\theta & 0 & \mathrm{c}\theta \end{bmatrix}, \boldsymbol{T}_\Theta(\boldsymbol{\Theta}_{ng}) = \begin{bmatrix} 1 & 0 & \mathrm{t}\theta \\ 0 & 1 & 0 \\ 0 & 0 & 1/\mathrm{c}\theta \end{bmatrix}. \tag{5.6}$$

Then, with the assumption of $\boldsymbol{v}_{g/n}^n = [0, 0, 0]^\top$, we can find:

$$\begin{aligned} \boldsymbol{v}_{g/n}^b &= \boldsymbol{R}_g^n(\boldsymbol{\Theta}_{ng})^{-1}\boldsymbol{v}_{g/n}^n = [0, 0, 0]^\top \\ \boldsymbol{\omega}_{g/n}^b &= \boldsymbol{T}_\Theta(\boldsymbol{\Theta}_{ng})^{-1}\dot{\boldsymbol{\Theta}}_{ng} = [0, \dot{\theta}, 0]^\top. \end{aligned} \tag{5.7}$$

Therefore, the motion model of the pitch movement can be represented as:

$$I_y^{CG}\dot{\omega}_{y,g/n}^b = I_y^{CG}\ddot{\theta} = M_y^g + m_y^g. \tag{5.8}$$

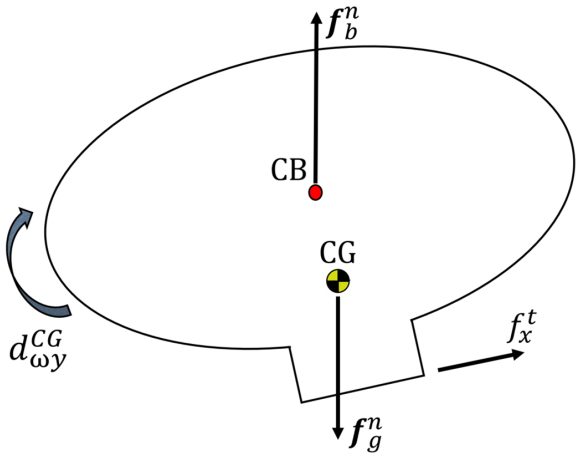

Figure 5.1: Side view of GT-MAB. Forces and moments that contribute to the pitching oscillation are annotated on the plot.

Force and torque analysis

Figure 5.1 demonstrates the major forces and moments while GT-MAB is pitching. The pair of forces, $\boldsymbol{f}_b^n$ and $\boldsymbol{f}_g^n$, are the buoyancy and gravitational force at CV and CG. The motor thrust force is represented as f_x^t. The thruster-induced torque about the CG is denoted as τ_y^g. The moment of inertia, air damping moment and gravitational restoring torque the CG are represented as I_y^{CG}, $d_{\omega y}^{CG}$, and g_y^{CG} separately. The position of CG in the body frame $\{b\}$ is denoted as $\boldsymbol{r}_{g/b}^b = [r_{x,g/b}^b, r_{y,g/b}^b, r_{z,g/b}^b]^\top$. Similarly, the position of the surge thruster relative to CG in $\{b\}$ is $\boldsymbol{r}_{t/g}^b = [r_{x,t/g}^b, r_{y,t/g}^b, r_{z,t/g}^b]^\top$. The distance between the between CB and the surge thruster is represented as $\boldsymbol{r}_{t/b}^b = [r_{x,t/b}^b, r_{y,t/b}^b, r_{z,t/b}^b]^\top$. Then, the pitching oscillation about the CG can be written as:

$$I_y^{CG}\ddot{\theta} + d_{\omega y}^{CG} + g_y^{CG} = \tau_y^g. \tag{5.9}$$

The aerodynamic damping term, $d_{\omega y}^{CG}$, can be assumed to be linear to angular velocity $\dot{\theta}$ for the low-speed indoor blimps [26]. Denote $D_{\omega y}^{CG}$ as the damping coefficient, and $d_{\omega y}^{CG}$ can be found as:

$$d_{\omega y}^{CG} = D_{\omega y}^{CG}\dot{\theta}. \tag{5.10}$$

The gravitational restoring torque, g_y^{CG}, stabilizes the blimp given that CG is below CB. GT-MAB is neutrally ballasted prior to each flight, thus we can assume that the total buoyancy has the same magnitude as the total gravitational force. Since both $\boldsymbol{f}_b^n$ and $\boldsymbol{f}_g^n$ are vertical in the inertial frame, we have $\boldsymbol{f}_g^n = -\boldsymbol{f}_b^n = [0, 0, m_{RB}g]^\top$, where g is the gravitational constant. Therefore, the stabilization moment, g_y^{CG}, can be represented as:

$$\begin{aligned} g_y^{CG} &= r_{z,g/b}^b f_{gz}^n \sin(\theta) = -r_{z,g/b}^b f_{bz}^n \sin(\theta) \\ &= r_{z,g/b}^b m_{RB} g \sin(\theta). \end{aligned} \tag{5.11}$$

The pitching moment induced by the thrusters, τ_{y}^g, can be found as $\tau_{\mathrm{y}}^g = r_{z,t/g}^b f_x^t$. As illustrated in Figure 5.1, the term $r_{z,t/g}^b$ can be written as $r_{z,t/g}^b = r_{z,t/b}^b - r_{z,g/b}^b$, where $r_{z,t/b}^b$ is a constant parameter from the dimension measurements. Thus, the thruster-induce torque can be represented as:

$$\tau_{\mathrm{y}}^g = r_{z,t/g}^b f_x^t \quad = (r_{z,t/b}^b - r_{z,g/b}^b) f_x^t. \tag{5.12}$$

Therefore, the dynamics model in Eq. (5.9) can be expanded as:

$$I_y^{CG}\ddot{\theta} + D_{\omega y}^{CG}\dot{\theta} + r_{z,g/b}^b m_{RB} g \sin(\theta) = (r_{z,t/b}^b - r_{z,g/b}^b) f_x^t. \tag{5.13}$$

Grey box model in state space form

The relationship between the forces and torques in Eq. (5.13) can be written into state-space form. We define the state variables $\boldsymbol{x}_\theta = [\theta, \dot{\theta}]^\top$, which are the angle and angular

rate of the pitching motion separately. Then, Eq. (5.13) can be represented as:

$$\begin{aligned}\dot{x}_{\theta 1} &= x_{\theta 2} \\ \dot{x}_{\theta 2} &= (-D_{\omega y}^{CG} x_{\theta 2} - m_{RB} g r_{z,g/b}^{b} \sin(x_{\theta 1}) + (r_{z,t/b}^{b} - r_{z,g/b}^{b}) f_{x}^{t}) / I_{y}^{CG}.\end{aligned} \tag{5.14}$$

The terms $r_{z,t/b}^{b}$, $r_{z,g/b}^{b}$, m_{RB}, and f_{x}^{t} in Eq. (5.14) can be calculated or measured with relatively good accuracy. However, the air damping coefficient $D_{\omega y}^{CG}$ and the moment of inertia I_{y}^{CG} cannot be easily estimated due to the complex aerodynamics effects and the non-ideal geometry of the envelope. Therefore, the pitching dynamics described in Eq. (5.14) can be considered as a grey box model, where the model structure is explicitly specified, and the parameters are partially known.

5.1.2 Parameter Identification

The parameter $r_{z,t/b}^{b}$

$r_{z,t/b}^{b}$ is the distance between CB and the motor thrust force f_{x}^{t}, as demonstrated in Figure 5.1. In contrast to large outdoor airships which usually adjust their buoyancy by changing the volume of air and helium, GT-MAB uses thrusters to adjust its altitude to reduce the size and improve maneuverability. Therefore, the dimension of GT-MAB is consistent, and can be considered as a rigid body when inflated. Owing to this, $r_{z,t/b}^{b}$ is a constant parameter and can be calculated as:

$$r_{z,t/b}^{b} = H_{\mathrm{ENV}}/2 + H_{\mathrm{GON}}, \tag{5.15}$$

where H_{ENV} and H_{GON} are the thickness of the envelope and the height of the gondola, as illustrated in Figure 5.2. With the height measurements $H_{\mathrm{ENV}} = 0.44\mathrm{m}$ and $H_{\mathrm{GON}} = 0.04\mathrm{m}$, we have $r_{z,t/b}^{b} = 0.26\mathrm{m}$.

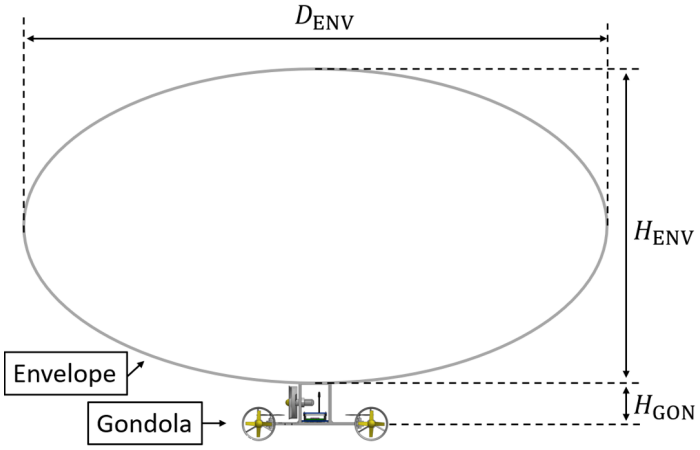

Figure 5.2: Dimension of the envelope and the gondola of GT-MAB.

The motor thrust force f_x^t

f_x^t represents the total surge thrust generated by the motors. The terminal voltage of the motor is determined by the duty cycle. Positive duty cycle will result the motor thrust along X_g direction, while negative value will generate force oppositely. Neglecting the resistance of the electronics such as H-bridge, we can approximate the voltage applied on the motor as:

$$V_{\text{mtr,i}} = V_{\text{batt}} \cdot d_{mtr,i}, \tag{5.16}$$

where V_{batt} is the battery voltage, which can be measured by the circuitry on the GT-MAB. $d_{mtr,i}$ and $V_{\text{mtr,i}}$ are the duty cycle and the resulting terminal voltage of the i-th motor. Similar to the work [26], we measure the motor thrust with a high-accuracy scale. The relationship between the motor thrust and the applied voltage can be seen in Figure 5.3.

The rigid-body mass m_{RB}

The total rigid-body mass of GT-MAB, m_{RB}, is hard to be directly measured since the helium gas inside the envelope cannot be easily gauged. Instead, by measuring the lifting force provided by the envelope, we can derive the total buoyancy of GT-MAB, and therefore find the total mass of the vehicle. Let $\boldsymbol{f}_l^n = [0, 0, f_{lz}^n]^\top$ be the lifting force provided

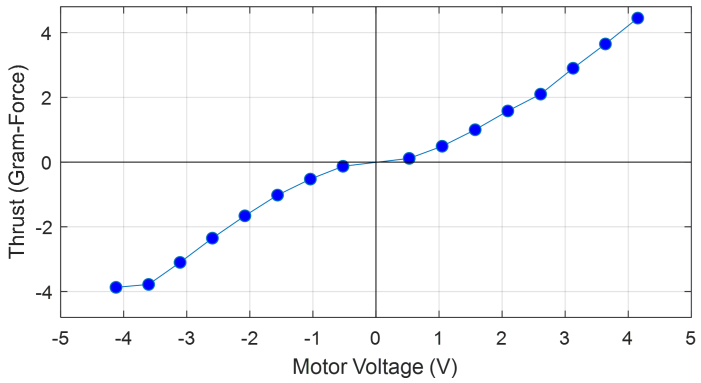

Figure 5.3: Motor thrust force versus the terminal voltage V_{mtr}.

by the envelope, which is equal to the total buoyancy $\boldsymbol{f}_b^n = [0, 0, f_{bz}^n]^\top$ minus the total gravitational force of the helium gas and the deflated envelope. Moreover, since GT-MAB is neutrally buoyant, f_{lz}^n equals to the gravitational force of all the components that are attached on the envelope: the gondola assembly, the ballast weight, and the localization markers. Therefore, f_{bz}^n and f_{lz}^n can be represented as follows:

$$\begin{aligned} f_{lz}^n &= f_{bz}^n + (m_{\text{envelope}} + m_{\text{helium}})g \\ &= -(m_{\text{gondola}} + m_{\text{marker}} + m_{\text{ballast}})g \end{aligned} \tag{5.17}$$

$$\begin{aligned} f_{bz}^n = &- (m_{\text{envelope}} + m_{\text{helium}})g \\ &- (m_{\text{gondola}} + m_{\text{marker}} + m_{\text{ballast}})g, \end{aligned} \tag{5.18}$$

where m_{envelope}, m_{helium}, m_{gondola}, m_{marker}, m_{ballast} are the mass of the deflated envelope, helium gas, gondola assembly, localization tackers, and the ballast weight to keep GT-MAB neutrally buoyant. Both f_{lz}^n and f_{bz}^n have negative value due to the Z-down coordinate convention.

According to Archimedes' principle, and assuming the envelope dominates the volume of GT-MAB, we can find that the total buoyancy f_{bz}^n is equal to the weight of air that the

envelope displaces. Then, Eq. (5.18) for f_{bz}^n can be written as:

$$\begin{aligned} f_{bz}^n &= -\rho_{\text{air}} V_{\text{envelope}} g \\ &= -(m_{\text{envelope}} + m_{\text{helium}} + m_{\text{gondola}} + m_{\text{marker}} + m_{\text{ballast}}) g, \end{aligned} \tag{5.19}$$

where ρ_{air} and V_{envelope} are the density of air and the volume of the envelope. Given that the mass of the helium gas is:

$$m_{\text{helium}} = \rho_{\text{helium}} V_{\text{helium}} = \rho_{\text{helium}} V_{\text{envelope}}, \tag{5.20}$$

the volume of the envelope can be calculated as:

$$V_{\text{envelope}} = \frac{m_{\text{gondola}} + m_{\text{marker}} + m_{\text{ballast}} + m_{\text{envelope}}}{\rho_{\text{air}} - \rho_{\text{helium}}}. \tag{5.21}$$

Assuming the temperature of the indoor environment is around 300K (26.85°C), density of both helium and air is known as $\rho_{\text{helium}} = 0.164\text{kg/m}^3$ and $\rho_{\text{air}} = 1.161\text{kg/m}^3$. With the total mass of the four components in Eq. (5.21) measured as 107.24 grams, the overall rigid-body mass of GT-MAB, m_{RB}, can be calculated as:

$$m_{RB} = \rho_{\text{air}} V_{\text{envelope}} = 0.1249\text{kg}. \tag{5.22}$$

The CG position $r_{z,g/b}^b$ and the initial approximation of I_y^{CG}

With the mass of all components of GT-MAB measured or calculated in previous sections, we use CAD software to calculate the position of the CG, namely $r_{z,g/b}^b$, and the rough estimation of the moment of inertia, I_y^{CG}. The estimated I_y^{CG} will be used as the initial approximation for future system identification experiments.

As illustrated in Figure 5.4, the envelope of GT-MAB is modeled as an ellipsoid in the CAD software. From the work [55], dimension of the inflated envelope can be calculated

by its deflated radius as:

$$\begin{aligned} r_{\text{inflated}} &\approx 0.7627 r_{\text{deflated}} \\ \tau_{\text{inflated}} &\approx 0.9139 r_{\text{deflated}}, \end{aligned} \tag{5.23}$$

where r_{deflated} is the radius of the deflated envelope, and r_{inflated} and τ_{inflated} are the radius and thickness of the envelope when inflated. Therefore, the ellipsoid CAD model with dimension r_{inflated} and τ_{inflated} is constructed with measurement $r_{\text{deflated}} = 0.457\text{m}$. With Autodesk Inventor software [64], we found that $r^b_{z,g/b} = 0.0971\text{m}$ and $I_y^{CG} = 0.00371\text{kg} \cdot \text{m}^2$.

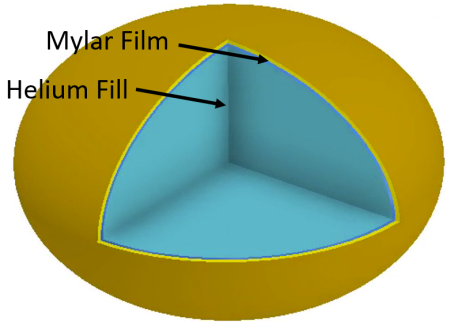

Figure 5.4: CAD model of the helium-filled envelope.

Rotational inertia I_y^{CG} and damping coefficient $D_{\omega y}^{CG}$

Now I_y^{CG} and $D_{\omega y}^{CG}$ are the only two unknown parameters in the grey box model described in Eq. (5.14). A series of system identification experiments are designed to obtain these parameters. The GT-MAB is released with an initial pitch angle, and the motion capture system (OptiTrack) logs the free response of the pitching oscillation. The experiment is repeated eight times with different initial angles. The first seven datasets are used for identifying the parameters and the last one is for validation.

As listed in Table 5.1, seven I_y^{CG} and $D_{\omega y}^{CG}$ pairs are identified from the first seven datasets with MATLAB system identification toolbox [61]. Figure 5.5 demonstrates both the logged pitch angle and the simulated response with the identified parameters from the first dataset. The fitting between the measured and modeled system is quantified as normalized root-mean-square error (NRMSE). The final estimations of I_y^{CG} and $D_{\omega y}^{CG}$ are

found as the average from the seven identified results in Table 5.1, which are $I_y^{CG} = 0.005821\text{kg} \cdot \text{m}^2$ and $b = 0.000980\text{N} \cdot \text{m} \cdot \text{s/rad}$.

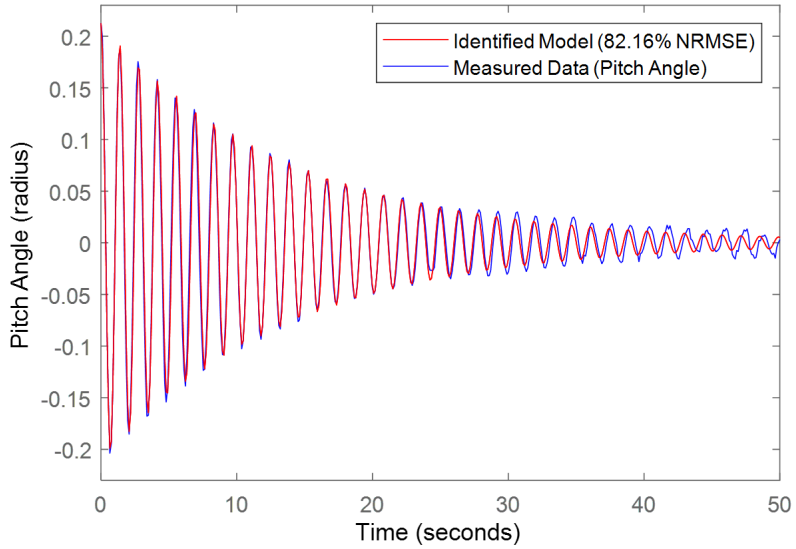

Figure 5.5: Measured pitching oscillation and the simulated response with the identified parameters from dataset 1.

Table 5.1: Rotational inertia and damping coefficient identified from the experiments

	I_y^{CG}	$D_{\omega y}^{CG}$	NRMSE Fit
Dataset 1	0.005782	0.000838	82.16%
Dataset 2	0.005847	0.000978	85.45%
Dataset 3	0.005835	0.000940	84.29%
Dataset 4	0.005828	0.001140	85.20%
Dataset 5	0.005851	0.001083	87.26%
Dataset 6	0.005750	0.001025	77.80%
Dataset 7	0.005855	0.000857	85.21%
Mean	0.005821	0.000980	83.91%

5.1.3 Identified Dynamics Model

Table 5.2 summarizes the parameters of the dynamics model obtained from the previous sections. Therefore, the pitching dynamics model of GT-MAB in Eq. (5.13) can be represented as:

$$\ddot{\theta} = -20.4284 \sin(\theta) - 0.1684\dot{\theta} + 27.9933 f_x^t. \tag{5.24}$$

Table 5.2: List of parameters for GT-MAB's pitching dynamics model

Parameters	Value
g	9.81 $\mathrm{m/s^2}$
I_y^{CG}	0.005821 $\mathrm{kg \cdot m^2}$
$D_{\omega y}^{CG}$	0.000980 $\mathrm{N \cdot m \cdot s/rad}$
m_{RB}	0.1249 kg
$r_{z,t/b}^b$	0.26 m
$r_{z,g/b}^b$	0.097051 m

5.1.4 Linearization and Validation

The identified model is then linearized around $\theta = \dot{\theta} = 0$ for future controller design. State-space form of the linearized model can be written as:

$$\begin{bmatrix} \dot{\theta} \\ \ddot{\theta} \end{bmatrix} = \begin{bmatrix} 0 & 1 \\ -20.4284 & -0.1684 \end{bmatrix} \begin{bmatrix} \theta \\ \dot{\theta} \end{bmatrix} + \begin{bmatrix} 0 \\ 27.9933 \end{bmatrix} f_x^t, \tag{5.25}$$

This linearized model is compared with the eighth dataset discussed in Chapter 5.1.2 for validation. The linearized model has a satisfying 88.37% NRMSE fit with the validation data, which can be seen in Figure 5.6.

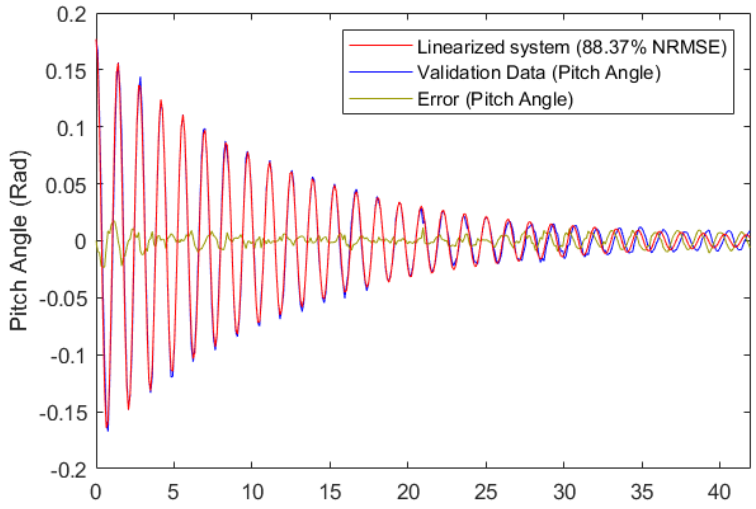

Figure 5.6: Measured pitching oscillation from the validation dataset and the simulated response with the linearized dynamics model.

5.2 Motion Model for Swing Oscillation during Cruising Flight

Chapter 5.1 has investigated the swing oscillation of indoor blimps by modeling and identifying the rotational motion of GT-MAB. However, this work only considers motion model during the hovering flight. The dynamics of the swing motion becomes significantly more complicated for cruising, since there is a strong coupling between the translational and rotational motion. In this section, we extend our previous efforts on modeling the swing motion of GT-MAB by including the coupling between the translational and rotational movements into consideration. We incorporate the generic kinematics and dynamic model of underwater vehicles given that the density of GT-MAB is identical to the surrounding air. The 6-DOF motion model of GT-MAB is derived based on its mechanical design. The full model is then reduced to 3-DOF given the symmetry of GT-MAB around its vertical axis. Parameters of the simplified model are identified and verified with experimental data. The swing oscillation is a common problem among indoor miniature blimps. Finless bottom-heavy underactuated design is widely adopted by many indoor MABs such as [8, 23]. Therefore, the proposed methods in this section could be applied to other indoor miniature blimps.

5.2.1 Model Construction

6-DOF dynamic model and simplification for GT-MAB

Indoor MABs are usually ballasted to the same density as the surrounding fluid to enable altitude control solely with motor thrust. Thus, the volume-to-mass ratio of an indoor blimp is very large compare to other types of aerial robots. As a result, the aerodynamic damping and the added mass cannot be neglected. Moreover, there exists restoring torque due to the displacement between the center-of-buoyancy (CB) and the center-of-gravity (CG). Therefore, given the similar operating conditions between MABs and underwater

vehicles, the generic 6-DOF motion model from [59] is described as:

$$\boldsymbol{\tau}^b = \boldsymbol{M}^{CB}\dot{\boldsymbol{\nu}}^b_{b/n} + \boldsymbol{C}^{CB}(\boldsymbol{\nu}^b_{b/n})\boldsymbol{\nu}^b_{b/n} + \boldsymbol{D}^{CB}(\boldsymbol{\nu}^b_{b/n})\boldsymbol{\nu}^b_{b/n} + \boldsymbol{g}^{CB}(\boldsymbol{\eta}^n_{b/n}), \tag{5.26}$$

where $\boldsymbol{\tau}^b$ represents the external forces and torques. $\boldsymbol{M}^{CB}$ is the total system inertia matrix. $\boldsymbol{C}^{CB}(\boldsymbol{\nu}^b_{b/n})$ represents the matrix of the Coiolis and centripetal terms. $\boldsymbol{D}^{CB}(\boldsymbol{\nu}^b_{b/n})$ is the damping matrix. $\boldsymbol{g}^{CB}(\boldsymbol{\eta}^n_{b/n})$ is the restoring forces and moments. The above-mentioned terms in Eq. (5.26) are defined as follows:

External forces and moments

$\boldsymbol{\tau}^b \in \mathbb{R}^6$ is the summary of all external forces and moments asserted at CB. In this work, $\boldsymbol{\tau}^b$ is induced solely by the motor thrusts:

$$\boldsymbol{\tau}^b = [f^b_x, f^b_y, f^b_z, \tau^b_x, \tau^b_y, \tau^b_z]^\top. \tag{5.27}$$

Inertia matrix

$\boldsymbol{M}^{CB}_{6\times6}$ is the total inertia matrix at CB:

$$\boldsymbol{M}^{CB} = \boldsymbol{M}^{CB}_{RB} + \boldsymbol{M}^{CB}_{A}, \tag{5.28}$$

where $\boldsymbol{M}^{CB}_{RB}$ and $\boldsymbol{M}^{CB}_{A}$ represent the rigid-body and added inertia matrix. Given that the gondola has neglectable volume and CB is at the center of the symmetric envelope, the added inertia matrix can be simplified with only diagonal terms:

$$\boldsymbol{M}^{CB}_{A} = \mathrm{diag}(m_{Ax}, m_{Ay}, m_{Az}, I_{Ax}, I_{Ay}, I_{Az}). \tag{5.29}$$

With the symmetric design of GT-MAB, we have $m_{Ax} = m_{Ay}$ and $I_{Ax} = I_{Ay}$. Moreover, the rigid-body inertia matrix of GT-MAB is diagonal at CG, which is defined as:

$$\boldsymbol{M}_{RB}^{CG} = \mathrm{diag}(m_{RB}, m_{RB}, m_{RB}, I_{RBx}, I_{RBy}, I_{RBz}), \tag{5.30}$$

where m_{RB} is the rigid-body mass of GT-MAB. Owing to the symmetric design of GT-MAB, we have $I_{RBx} = I_{RBy}$. Since $\boldsymbol{M}_{RB}^{CG}$ is defined at CG, it needs to be transformed to CB with the system transformation matrix discussed in [59]:

$$\begin{aligned} \boldsymbol{M}_{RB}^{CB} &= \boldsymbol{H}^{\top}(\boldsymbol{r}_{g/b}^{b})\boldsymbol{M}_{RB}^{CG}\boldsymbol{H}(\boldsymbol{r}_{g/b}^{b}) \\ \boldsymbol{H}(\boldsymbol{r}_{g/b}^{b}) &= \begin{bmatrix} \boldsymbol{I}_{3\times3} & \boldsymbol{S}^{\top}(\boldsymbol{r}_{g/b}^{b}) \\ \boldsymbol{0}_{3\times3} & \boldsymbol{I}_{3\times3} \end{bmatrix}, \end{aligned} \tag{5.31}$$

where $\boldsymbol{S}(\cdot)$ is the skew-symmetric cross-product operator. $\boldsymbol{r}_{g/b}^{b}$ is the position of CG in body frame $\{b\}$. Owing to the symmetric design of GT-MAB, $\boldsymbol{r}_{g/b}^{b} = [0, 0, r_{z,g/b}^{b}]^{\top}$. Therefore, the system inertia matrix at CB can be derived as:

$$\begin{aligned} \boldsymbol{M}^{CB} &= \boldsymbol{M}_{RB}^{CB} + \boldsymbol{M}_{A}^{CB} \\ &= \begin{bmatrix} m_x & 0 & 0 & 0 & m_{RB}r_{z,g/b}^{b} & 0 \\ 0 & m_y & 0 & -m_{RB}r_{z,g/b}^{b} & 0 & 0 \\ 0 & 0 & m_z & 0 & 0 & 0 \\ 0 & -m_{RB}r_{z,g/b}^{b} & 0 & I_x & 0 & 0 \\ m_{RB}r_{z,g/b}^{b} & 0 & 0 & 0 & I_y & 0 \\ 0 & 0 & 0 & 0 & 0 & I_z \end{bmatrix}, \end{aligned} \tag{5.32}$$

where the diagonal terms contain both the rigid-body and added-mass components. Thus, $m_i = m_{RB} + m_{Ai}$, $i \in \{x, y, z\}$. $I_i = I_{RBi} + m_{RB}(r_{z,g/b}^{b})^2 + I_{Ai}$, $i \in \{x, y\}$; and $I_z = I_{RBz} + I_{Az}$.

Coriolis-centripetal matrix

$\boldsymbol{C}_{6\times6}^{CB}$ also contains components from both rigid-body and added inertia. With the operator $\boldsymbol{C}(\boldsymbol{M},\boldsymbol{\nu})$ defined in [59], $\boldsymbol{C}^{CB}$ can be found as:

$$\boldsymbol{C}^{CB} = \boldsymbol{C}(\boldsymbol{M}_{RB}^{CB}, \boldsymbol{\nu}_{b/n}^{b}) + \boldsymbol{C}(\boldsymbol{M}_{A}^{CB}, \boldsymbol{\nu}_{b/n}^{b}). \tag{5.33}$$

Aerodynamic damping

The aerodynamic damping can be approximated as proportional to the linear and angular velocities for low-speed indoor blimps [26]. Moreover, owing to the symmetric envelopes used in most indoor MABs, the damping matrix is diagonal at CB:

$$\boldsymbol{D}^{CB}(\boldsymbol{\nu}_{b/n}^{b}) = \mathrm{diag}(D_{vx}^{CB}, D_{vy}^{CB}, D_{vz}^{CB}, D_{\omega x}^{CB}, D_{\omega y}^{CB}, D_{\omega z}^{CB}). \tag{5.34}$$

Restoration torque

Given that CG is below the center of buoyancy, there exists restoring torque that stabilizes the blimp back to the leveled attitude. Denote $\boldsymbol{r}_g^b$ and $\boldsymbol{r}_b^b$ be the position of CG and CB in the body-frame, and $\boldsymbol{f}_g^b = -\boldsymbol{f}_b^b$ be the gravitational and buoyancy force decomposed in $\{b\}$, the restoring torque can be simplified from [59] as:

$$\boldsymbol{g}^{CB}(\boldsymbol{\eta}_{b/n}^{n}) = -\begin{bmatrix} \boldsymbol{f}_g^b + \boldsymbol{f}_b^b \\ \boldsymbol{r}_g^b \times \boldsymbol{f}_g^b + \boldsymbol{r}_b^b \times \boldsymbol{f}_b^b \end{bmatrix} = -\begin{bmatrix} \boldsymbol{0} \\ \boldsymbol{r}_g^b \times \boldsymbol{f}_g^b \end{bmatrix}. \tag{5.35}$$

5.2.2 3-DOF Model Reduction

As discussed in Chapter 3.3, GT-MAB has a symmetric envelope about the vertical axes, and capability of pointing the thrust vector all planar directions. Therefore, we can reduce the 6-DOF motion of GT-MAB to 3-DOF movement on a vertical plane. As demonstrated

in Figure 5.7, if the blimp starts from rest at position A, and targets at waypoint B, the ideal trajectory can be contained within a vertical plane that includes both points. For the convenience of parameter identification, we assume there is no initial lateral velocity, and the initial heading of the blimp is aligned with the inertial frame. Therefore, the 3-DOF motion on the vertical plane can be written as:

$$\begin{aligned} \dot{\boldsymbol{p}}^n_{b/n} &= [\dot{p}^n_{x,b/n}, 0, \dot{p}^n_{z,b/n}]^\top \\ \boldsymbol{\Theta}_{nb} &= [0, \theta, 0]^\top \\ \boldsymbol{\tau}^b &= [f^b_x, 0, f^b_z, 0, \tau^b_y, 0]^\top. \end{aligned} \tag{5.36}$$

With $\boldsymbol{\Theta}_{nb} = [0, \theta, 0]^\top$, Eq. (4.2) and Eq. (4.3) can be simplified as:

$$\boldsymbol{R}^n_b(\boldsymbol{\Theta_{nb}}) = \begin{bmatrix} \mathrm{c}\theta & 0 & \mathrm{s}\theta \\ 0 & 1 & 0 \\ -\mathrm{s}\theta & 0 & \mathrm{c}\theta \end{bmatrix}, \boldsymbol{T}_\Theta(\boldsymbol{\Theta}_{nb}) = \begin{bmatrix} 1 & 0 & \mathrm{t}\theta \\ 0 & 1 & 0 \\ 0 & 0 & 1/\mathrm{c}\theta \end{bmatrix}. \tag{5.37}$$

Then, the velocities in the body-fixed frame $\{b\}$ are:

$$\begin{aligned} \boldsymbol{v}^b_{b/n} &= \boldsymbol{R}^n_b(\boldsymbol{\Theta}_{nb})^{-1} \boldsymbol{v}^n_{b/n} = [v^b_{x,b/n}, 0, v^b_{z,b/n}]^\top \\ \boldsymbol{\omega}^b_{b/n} &= \boldsymbol{T}_\Theta(\boldsymbol{\Theta}_{nb})^{-1} \dot{\boldsymbol{\Theta}}_{nb} = [0, \dot{\theta}, 0]^\top. \end{aligned} \tag{5.38}$$

Therefore, the equations of the simplified 3-DOF movement can be derived from the 6-DOF motion model in Eq. (5.26) as:

$$
\begin{aligned}
&(m_{RB} + m_{Ax})\dot{v}^b_{x,b/n} + m_{RB} r^b_{z,g/b} \dot{\omega}^b_{y,b/n} \\
&+ (m_{RB} + m_{Az}) v^b_{z,b/n} \omega^b_{y,b/n} + D^{CB}_{vx} v^b_{x,b/n} = f^b_x \\
&(m_{RB} + m_{Az})\dot{v}^b_{z,b/n} - m_{RB} r^b_{z,g/b} (\omega^b_{y,b/n})^2 \\
&- (m_{RB} + m_{Ax}) v^b_{x,b/n} \omega^b_{y,b/n} + D^{CB}_{vz} v^b_{z,b/n} = f^b_z \\
&I_y \dot{\omega}^b_{y,b/n} + m_{RB} r^b_{z,g/b} (\dot{v}^b_{x,b/n} + v^b_{z,b/n} \omega^b_{y,b/n}) + D^{CB}_{\omega y} \omega^b_{y,b/n} \\
&+ (m_{Ax} - m_{Az}) v^b_{x,b/n} v^b_{z,b/n} + r^b_{z,g/b} m_{RB} g \sin(\theta) = \tau^b_y.
\end{aligned}
\tag{5.39}
$$

Due to the underactuated design of most indoor blimps including GT-MAB, $\tau^b_y = r^b_{z,t/b} f^b_x$, where $r^b_{z,t/b}$ is the vertical position of the longitudinal propulsion in $\{b\}$.

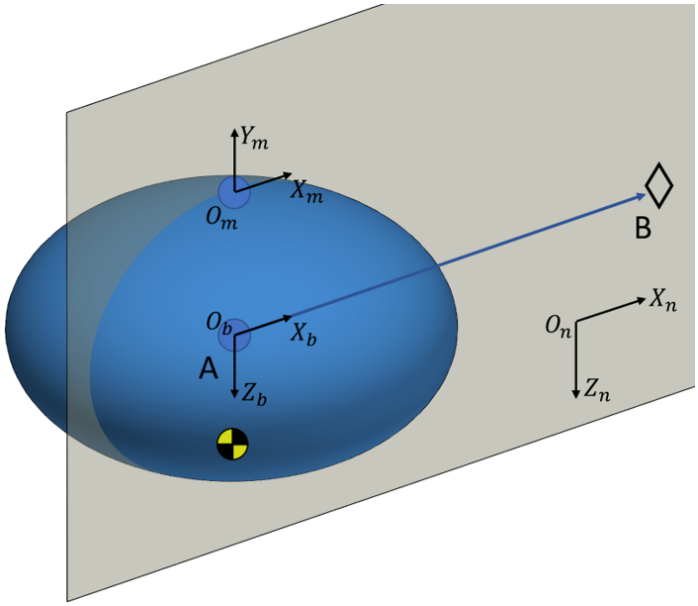

Figure 5.7: Motion of GT-MAB reduced to 3-DOF on a vertical plane.

5.2.3 Parameter Identification

This section identifies the parameters of the motion model described in Eq. (5.39). Specifically, we aim to find the parameters m_{RB}, m_{Ax}, m_{Az}, I_y, D^{CB}_{vx}, D^{CB}_{vz}, $D^{CB}_{\omega y}$, and $r^b_{z,g/b}$.

Data preparation

Miniature blimps use indoor localization systems due to the GPS-denied environment. These devices usually have different coordinate systems compare to the desired inertial frame. Therefore, measurements from the positioning systems need to be first converted to the inertial frame. The detailed derivation for converting the pose from $\{l\}$ to $\{n\}$ can be seem in Appendix B.

Parameters m_{RB}, m_{Ax}, m_{Az}, D_{vx}^{CB}, and D_{vz}^{CB}

The added mass and aerodynamic damping coefficients of GT-MAB are both diagonal at CB owing to the symmetric envelope. These parameters characterize the motion along body-frame axes. System identification experiments are designed to estimate these parameters from the motion of GT-MAB along X_b and Z_b axes separately.

In the scenario where the movement of GT-MAB is solely along X_b or Z_b axis, the motion model described in Eq. (5.39) can be represented as:

$$\begin{aligned} f_x^b &= f_{gx}^b + f_{bx}^b = (m_{RB} + m_{Ax})\dot{v}_{x,b/n}^b + D_{vx}^{CB} v_{x,b/n}^b \\ f_z^b &= f_{gz}^b + f_{bz}^b = (m_{RB} + m_{Az})\dot{v}_{z,b/n}^b + D_{vz}^{CB} v_{z,b/n}^b. \end{aligned} \tag{5.40}$$

Furthermore, if the movements in Eq. (5.40) are both along Z_n, as demonstrated in Figure 5.8, we can describe the motion in the inertial frame as:

$$\begin{bmatrix} \dot{p}_{z,b/n}^n \\ \ddot{p}_{z,b/n}^n \end{bmatrix} = \begin{bmatrix} 0 & 1 \\ 0 & -D_{vi}^{CB}/m_i \end{bmatrix} \begin{bmatrix} p_{z,b/n}^n \\ \dot{p}_{z,b/n}^n \end{bmatrix} + \begin{bmatrix} 0 \\ 1/m_i \end{bmatrix} (f_{gz}^n + f_{bz}^n), \tag{5.41}$$

where $p_{z,b/n}^n$ is the vertical position of the blimp in $\{n\}$. $m_i = m_{RB} + m_{Ai}$, $i \in \{x, z\}$. f_{gz}^n and f_{bz}^n are the total gravitational and buoyancy forces expressed in the inertial frame.

As illustrated in Figure 5.8, system identification experiments are designed to create the motion solely along X_b or Z_b axis. We adjust the position of the gondola to ensure that

CG is on the X_b or Z_b axis. After the gondola is ballasted to neutral buoyancy, we add test weights on the gondola to create accurate and constant traction force with direction along Z_n axis. The test weights are pre-calibrated such that the total gravity is exactly one and two gram-force larger than the buoyancy for the movements along X_b and Z_b separately. The blimp is then released with zero velocity and the initial attitude of GT-MAB is demonstrated in Figure 5.8. The experiments are conducted inside a laboratory with neglectable airflow perturbation. A total of 10 ceiling-mounted OptiTrack cameras capture the movement of the localization markers at the top of the envelope. The raw measurements from the motion tracking system are recorded and then converted to the position of the blimp in the inertial frame with the method discussed in Appendix B.

The experiments for the motion along X_b and Z_b axes are both repeated 21 times where the GT-MAB is released from different altitudes. Total flight duration is 152.73 seconds for the motion along X_b, and 143.88 seconds for the movement along Z_b. All flight data is captured at sampling rate of 120Hz. We use the first 20 datasets for parameter identification and reserve the last one for validation. The average estimate for the parameters in Eq. (5.41) are listed in Table 5.3. The standard deviation of each identified parameter is approximately one magnitude smaller than the mean value. Figure 5.9 demonstrates the close alignment between the validation data and the reconstructed response with the identified model. Given that m_{RB} was identified to be 0.1249kg in Chapter 5.1, we get $m_{Ax} = 0.0466\text{kg}$, and $m_{Az} = 0.0545\text{kg}$.

Table 5.3: Parameters of the translational motion identified from the experiments

Parameter	Mean	Standard Deviation	Avg. NRMSE Fit
m_x	0.1715	0.0111	99.34%
D_{vx}^{CB}	0.0125	0.0019	
m_z	0.1794	0.0102	98.09%
D_{vz}^{CB}	0.0480	0.0037	

The parameters and the normalized root mean square error (NRMSE) are obtained from 20 datasets for the motion along X_b and Z_b separately.

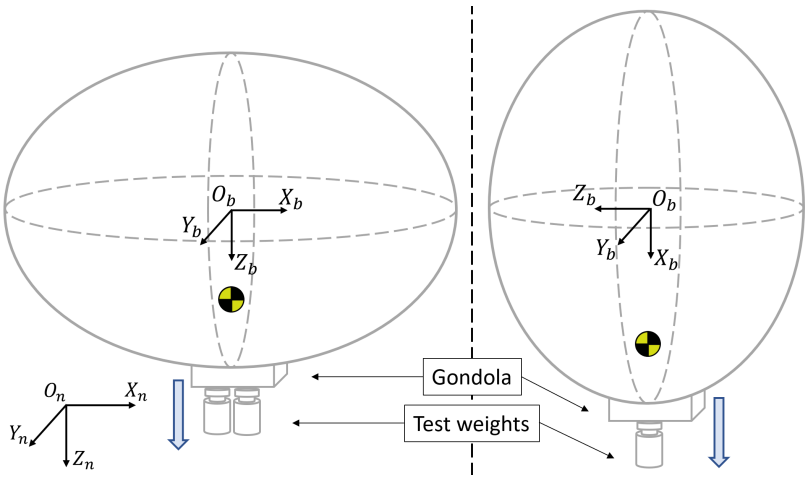

Figure 5.8: Experimental setup for identifying the added mass and the drag coefficients for the motion along GT-MAB's body axes. The direction of the movement is annotated with blue arrow.

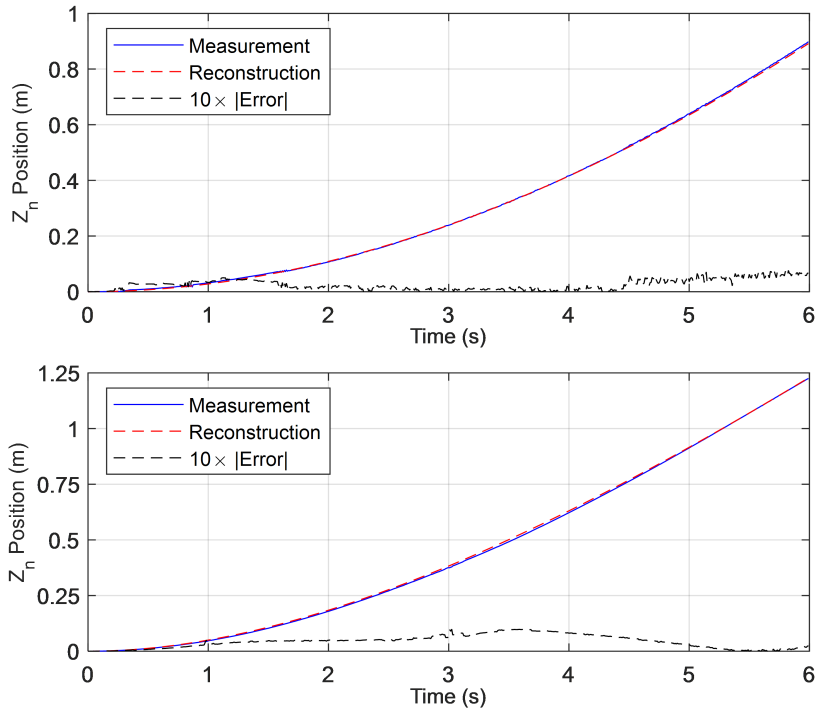

Figure 5.9: Comparison between the validation data and the reconstructed response with identified model parameters. NRMSE fit is 98.61% for the motion along Z_b (upper), and 98.82% for the movement along X_b (lower). The magnitude of the error is enlarged 10 times for better illustration.

5.2.4 Parameters $r^b_{z,g/b}$, I_y, and $D^{CB}_{\omega y}$

Chapter 5.1 has identified the center-of-gravity position, and the rotational inertia and damping coefficient at CG:

$$\begin{aligned} r^b_{z,g/b} &= 0.09705\text{m} \\ I^{CG}_y &= 0.005821\text{kg}\cdot\text{m}^2 \\ D^{CG}_{\omega y} &= 0.000980\text{N}\cdot\text{m}\cdot\text{s/rad}. \end{aligned} \tag{5.42}$$

Thus, the rotational inertia at CB, I_y, can be derived from the above-mentioned parameters. With the system transformation matrix described in Eq. (5.31), we first represent the inertia at CG as:

$$\begin{aligned} \boldsymbol{M}^{CG} &= \boldsymbol{M}^{CG}_{RB} + \boldsymbol{H}^{-\top}(\boldsymbol{r}^b_{g/b})\boldsymbol{M}^{CB}_A\boldsymbol{H}^{-1}(\boldsymbol{r}^b_{g/b}) \\ I^{CG}_y &= m_{Ax}(r^b_{z,g/b})^2 + I_{Ay} + I_{RBy}. \end{aligned} \tag{5.43}$$

From Eq. (5.32), we know that the rotational inertia at CB is:

$$I_y = I^{CB}_y = I_{RBy} + m_{RB}(r^b_{z,g/b})^2 + I_{Ay}, \tag{5.44}$$

Then, the parameter I_y can be calculated as:

$$\begin{aligned} I_y &= I^{CG}_y - m_{Ax}(r^b_{z,g/b})^2 + m_{RB}(r^b_{z,g/b})^2 \\ &= 0.0066\text{kg}\cdot\text{m}^2. \end{aligned} \tag{5.45}$$

Similarly, $D^{CB}_{\omega y}$ can be found by representing the rotational aerodynamic damping coefficient at CG as:

$$\begin{aligned} \boldsymbol{D}^{CG} &= \boldsymbol{H}^{-\top}(\boldsymbol{r}^b_{g/b})\boldsymbol{D}^{CB}\boldsymbol{H}^{-1}(\boldsymbol{r}^b_{g/b}) \\ D^{CG}_{\omega y} &= D^{CB}_{\omega y} + D^{CB}_{vx}(r^b_{z,g/b})^2. \end{aligned} \tag{5.46}$$

Therefore, from the damping coefficient at CG in Eq. (5.42), we can find

$D^{CB}_{\omega y} = 0.000862\text{N}\cdot\text{m}\cdot\text{s/rad}.$

CHAPTER 6

SWING-REDUCING CONTROLLER DESIGN FOR GT-MAB

6.1 Swing-Reducing for Station-Keeping Flight

This section presents the flight control system that stabilizes the swing motion of the GT-MAB during hovering flight. For the convenience of future comparison, this flight control system is referred as FCS 1.5.

As discussed in Chapter 1.3, the underactuated design, fluctuated position measurement, and control system latency are the major difficulties in stabilizing the swing oscillation of GT-MAB. In this section, we first discuss the impact of the control system latency, and the proposed approaches to reduce it. Then, the center-of-gravity position of GT-MAB is incorporated for less fluctuated position measurement. Next, feedback controllers are designed to reduce the swing oscillation of this underactuated robot. Lastly, the proposed flight control system is experimentally validated for reducing the swing oscillation of GT-MAB during hovering flight.

6.1.1 System Overview

Figure 6.1 demonstrates the overall setup of the flight control system. The pose of the GT-MAB is estimated by tracking the localization markers on top of the envelope. A ground station computer interfaces with the motion capture system, and runs the flight control software. The control commands are transmitted to the GT-MAB via wireless communication, and the onboard electronics of the blimp drive the thrusters once a command is received.

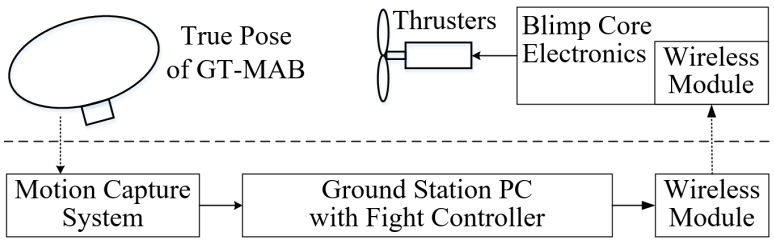

Figure 6.1: System overview of the flight control system (FCS 1.5) for reducing the swing oscillation during hovering flight.

6.1.2 System Latency Analysis and Reduction

The fast dynamics of the swing motion requires low latency from the flight control system. We first recall the dynamics model of the open-loop system identified in Chapter 5.1:

$$\begin{bmatrix} \dot{\theta} \\ \ddot{\theta} \end{bmatrix} = \begin{bmatrix} 0 & 1 \\ -20.4284 & -0.1684 \end{bmatrix} \begin{bmatrix} \theta \\ \dot{\theta} \end{bmatrix} + \begin{bmatrix} 0 \\ 27.9933 \end{bmatrix} f_x^t. \tag{6.1}$$

The linear system can be written as transfer function with the addition of overall system latency τ_{sys}:

$$\frac{27.99}{s^2 + 0.1684s + 20.43} e^{-\tau_{sys}s}, \tag{6.2}$$

where the system input is the forward motor thrust f_x^t and the output is the pitch angle of the blimp in radians. Then we incorporate the swing-stabilization controller discussed in Chapter 6.1.4, and the overall open-loop transfer function becomes

$$k_\omega(1 + \frac{k_\alpha}{k_\omega}s)\frac{27.99s}{s^2 + 0.1684s + 20.43} e^{-\tau_{sys}s}, \tag{6.3}$$

where k_ω and k_α are the controller gains for angular velocity and acceleration separately.

Figure 6.2 demonstrates the Nyquist diagrams of the overall system described in Eq. (6.3) under different amount of latency. The systems with zero latency, and delay of 0.06 seconds will be closed-loop stable. However, the system with latency of 0.15 seconds has the point $-1+0j$ within the clockwise cycle, which indicates closed-loop unstable. Though

larger tolerance on system latency can be achieved by lowering the controller gains, here we set the goal for the overall latency of 0.06 seconds for better controller performance.

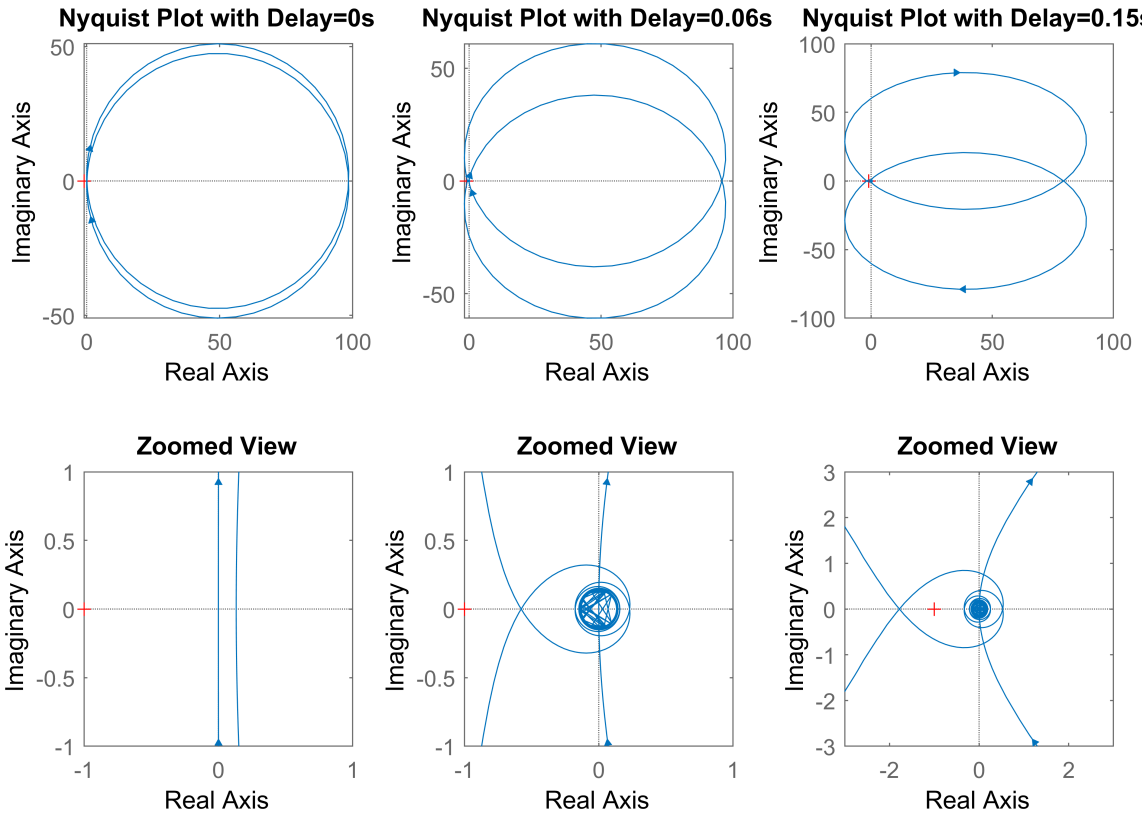

Figure 6.2: Nyquist diagram of the system under different latency. The system is closed-loop stable when delay is zero and 0.06s, but is unstable when delay is 0.15s.

The system latency comes from multiple sources. We divide the overall system latency into two groups, and conduct experiments to ensure the overall system latency is within the margin. The first portion of system latency is due to the motion capture system, the ground station computer, the wireless communication with the blimp, and the time needed for the onboard electronics to decode the control command and drive the motors. This group of latency is reduced by implementing the flight controller software with higher update rate, incorporating faster interface to the motion capture system, minimizing the response time of the onboard electronics and firmware, and enhancing the wireless communication. As shown in Figure 6.3, an experiment is designed to measure the delay of this part. We use a rotational plate with markers to emulate the attitude of GT-MAB during swing oscillation.

By comparing the rotation angle from the rotary encoder, and the voltage applied on the thruster, we observed the average delay of 30.5ms.

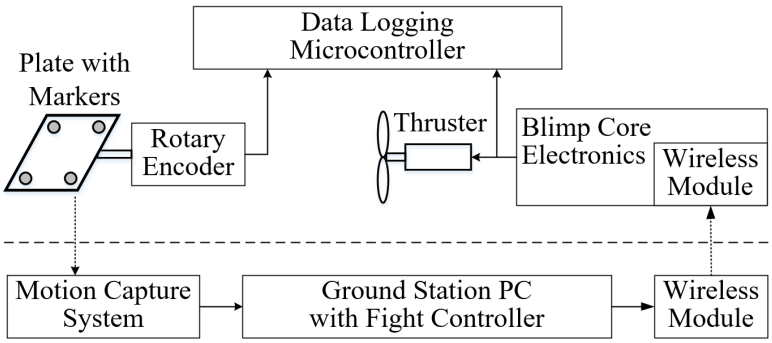

Figure 6.3: Experimental setup for measuring the latency of the control system.

The second portion of system latency is the time needed for the motor to reach the desired shaft speed. For faster actuator response, coreless DC motors and small-diameter multi-blade propellers are chosen for lower rotor inertia. To evaluate the response time of the thrusters, we establish a second-order model that is simplified from [65].

$$\begin{bmatrix} \dot{\Phi}_{\mathrm{mtr,i}} \\ \dot{\omega}_{\mathrm{mtr,i}} \end{bmatrix} = \begin{bmatrix} 0 & 1 \\ 0 & -1/\tau_{\mathrm{mtr}} \end{bmatrix} \begin{bmatrix} \Phi_{\mathrm{mtr,i}} \\ \omega_{\mathrm{mtr,i}} \end{bmatrix} + \begin{bmatrix} 0 \\ \beta_{\mathrm{mtr}}/\tau_{\mathrm{mtr}} \end{bmatrix} V_{\mathrm{mtr,i}}, \tag{6.4}$$

where Φ, ω represent the shaft angle and angular velocity of the thruster. The terminal voltage on the motor is denoted as $V_{\mathrm{mtr,i}}$. τ_{mtr} and β_{mtr} are time constant and static gain that characterize the response of the i-th motor. With the experimental setup shown in Figure 6.4, the step response of the thruster is collected. We fit the DC motor model to the measured response, and obtain the time constant $\tau_{\mathrm{mtr}} = 28\mathrm{ms}$. Therefore, the overall latency is reduced to approximately 0.06 seconds.

6.1.3 Center-of-gravity Position Calculation

Existing flight control systems for indoor miniature blimps usually assume zero pitch and roll angle. In such cases, the planar position of the motion capture marker is used to repre-

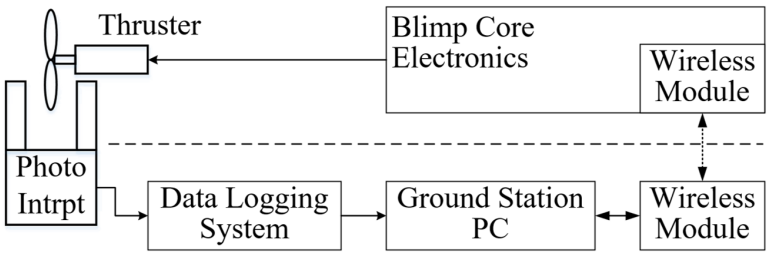

Figure 6.4: Experimental setup for measuring the thruster response of GT-MAB. A photo interrupter measures the angular velocity of the thruster without contacting the motor shaft.

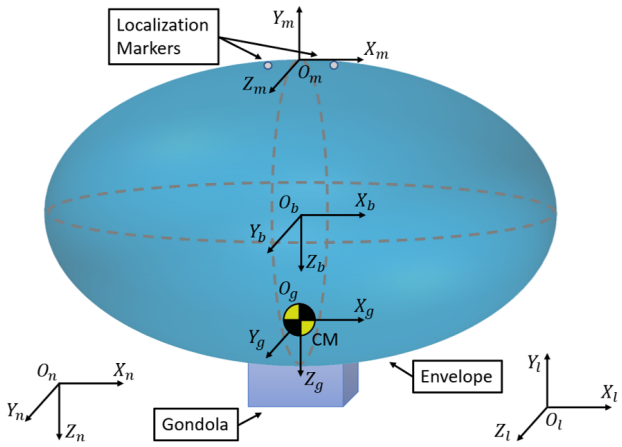

Figure 6.5: Demonstration of offset between the localization makers O_m, and the CG of GT-MAB.

sent that of the blimp in the inertial frame. However, as shown in Figure 6.5, the markers are usually installed on top of the envelope for the best visibility to the ceiling-mounted motion capture cameras, and the thrusters are often mounted on the gondola at the bottom of the envelope. With this widely applied configuration, the center of gravity, which is the pivot of rotation, is located between the markers and the actuators. As a consequence, the markers will first move toward the opposite direction of the motor thrust, and then towards the same direction. This undesired behavior is demonstrated with experimental data shown in Figure 6.6. The fluctuated measurement of the marker position may impact the feedback control of the translational motion of GT-MAB including station-keeping. In contrast, as illustrated in Figure 6.6, the CG position always moves towards the same direction as the thrust force. Therefore, we use the CG position of the blimp as the input of the station-

keeping controller. Since CG is located inside the envelope, its position cannot be directly measured. Instead, position of CG can be calculated from the pose measurement of the localization markers given the motion model identified in Chapter 5.1. Detailed derivation of CG position can be found in Appendix B.

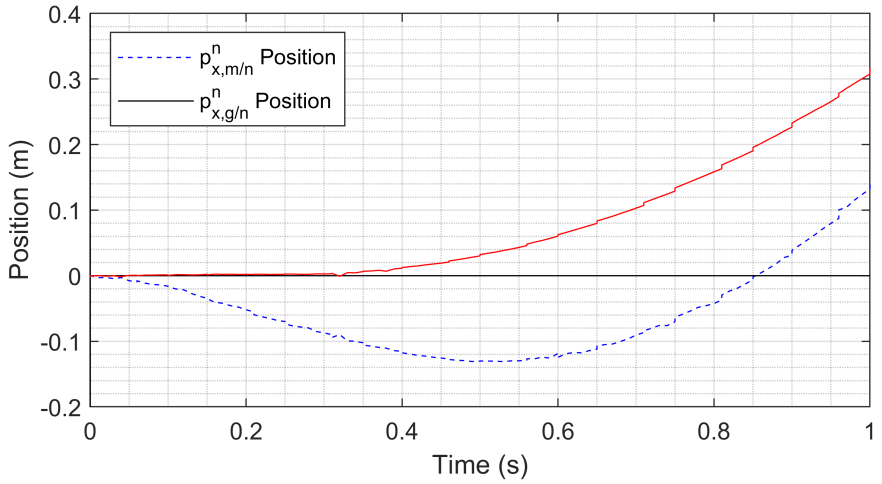

Figure 6.6: Position measurement of the marker and the center of gravity when constant forward thrust is applied.

6.1.4 Feedback Controller Design

Station keeping is one of the most common operating scenarios of GT-MAB. A flight controller is designed to keep GT-MAB at the desired position while simultaneously compensate the swing oscillation. As shown in Figure 6.7, the proposed method consists of a station-keeping controller that tracks the position and heading of GT-MAB, and a swing-reducing controller which reduces the roll and pitch oscillation of the robot.

Station-keeping controller

The station-keeping controller is an extension of Chapter 4. The controller keeps GT-MAB at the desired position $\boldsymbol{r}^n_{p,b/n} = [r^n_{px,b/n}, r^n_{py,b/n}, r^n_{pz,b/n}]^\top$ and holds its heading at r_ψ. As discussed in Chapter 6.1.3, the CG position of GT-MAB has significantly less fluctuation

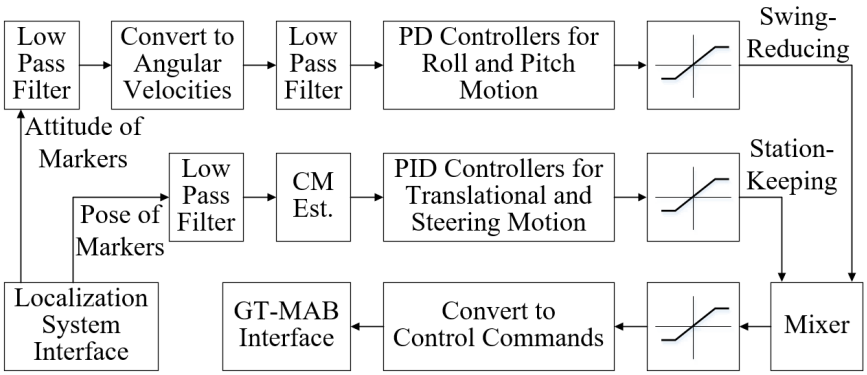

Figure 6.7: Functional block diagram of the flight control system (FCS 1.5).

compared to that of the localization markers. Therefore, we use $\boldsymbol{p}^n_{g/n}$ to represent the position of GT-MAB. Hence, the distance and heading error can be calculated as:

$$\begin{aligned} \boldsymbol{e}^n_{p,g/n} &= \boldsymbol{r}^n_{p,g/n} - \boldsymbol{p}^n_{g/n} \\ e_\psi &= r_\psi - \psi. \end{aligned} \tag{6.5}$$

Three PID controllers are implemented to minimize the position error. The controller outputs are denoted as f^n_x, f^n_y, f^n_z and τ^g_z, which can then be calculated separately by:

$$f^n_j = k^n_{pj} e^n_{pj,g/n} + k^n_{ij} \int_0^t e^n_{pj,g/n} dt' + k^n_{dj} \frac{de^n_{pj,g/n}}{dt}, \tag{6.6}$$

where $j = \{x, y, z\}$. f^n_j and $e^n_{pj,g/n}$ denote the output and error of each controller. k^n_{pj}, k^n_{ij}, k^n_{dj} represent the PID gains of the individual controllers. Since the position errors are defined in the inertial frame, the controller outputs for the translational motion is then transferred to GT-MAB's body frame as:

$$[f^g_x, f^g_y, f^g_z]^\top = \boldsymbol{R}^n_g(\boldsymbol{\Theta}_{ng})^{-1}[f^n_x, f^n_y, f^n_z]^\top, \tag{6.7}$$

where $\boldsymbol{R}^n_g(\boldsymbol{\Theta}_{ng})$ is the rotation matrix between the inertial frame and the body frame at-

tached at CG. Similarly, the heading control is designed as follows:

$$\tau_z^g = k_{p\psi} e_\psi + k_{i\psi} \int_0^t e_\psi dt' + k_{d\psi} \frac{de_\psi}{dt}, \tag{6.8}$$

where $k_{p\psi}$, $k_{i\psi}$ and $k_{d\psi}$ are the controller gains for the steering motion.

Swing-reducing controller

The swing-reducing controller stabilizes the roll and pitch motion of GT-MAB during hovering flight. Given the roll and pitch dynamics of the blimp are decoupled and almost identical, we first design the controller for pitch motion, and then apply the same control law to stabilize both pitch and roll movement.

From the linearized model of the pitch motion described in Eq. (5.25), there are two poles in the open-loop dynamics. As shown in Figure 6.8, the poles are located at $-0.0842 \pm 4.5190i$, indicating the open-loop dynamics is highly oscillatory with very limited damping. As a consequence, the undesired swing oscillation occurs once the GT-MAB cannot damp the disturbance torque induced by its underactuated configuration. This issue becomes more significant when more powerful thrusters are installed for better maneuverability and flyability against airflow.

To reduce the oscillation of this stable but highly oscillatory system, a PD controller is designed to regulate the angular velocity of the pitch motion:

$$\tau_y^g = k_\omega e^b_{\omega y,g/n} + k_\alpha \frac{de^b_{\omega y,g/n}}{dt}, \tag{6.9}$$

where τ_y^g and $e^b_{\omega y,g/n}$ denote the output and angular rate error of the controller. k_ω and k_α represents the feedback gains for the angular rate and acceleration. As shown in Figure 6.8, the closed-loop system under the PD controller has poles at -1.34 and -13.5 and zeros at 0 and -125. This indicates the closed-loop system has fast damping without oscillatory component.

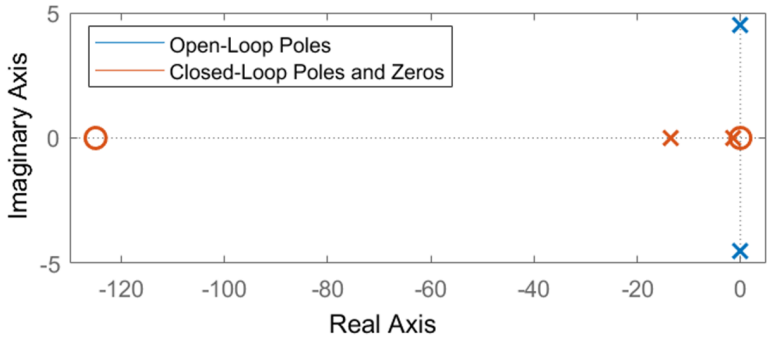

Figure 6.8: Pole and zero plot of both open-loop and closed-loop dynamics of GT-MAB's pitch motion.

The same control law is then applied to control the angular velocities of both pitch and roll motion, owing to the symmetrical design of GT-MAB. The setpoints of both controllers are set to zero for swing stabilization purpose. Therefore, the angular rate error of both controllers can be defined as:

$$\begin{aligned}[e^b_{\omega x,g/n}, e^b_{\omega y,g/n}]^\top &= [r^b_{\omega x,g/n} - \omega^b_{x,g/n}, r^b_{\omega y,g/n} - \omega^b_{y,g/n}]^\top \\ &= [-\omega^b_{x,g/n}, -\omega^b_{y,g/n}]^\top,\end{aligned} \tag{6.10}$$

where $\omega^b_{x,g/n}$ and $\omega^b_{y,g/n}$ are the angular velocities of GT-MAB around X_g and Y_g axes in the body frame. Detailed derivation of the angular velocities can be found in Appendix B. The outputs of the controllers are denoted as τ^g_x and τ^g_y for the roll and pitch motion separately.

6.1.5 Mixer Design

The outputs from both station-keeping and swing-reducing controllers are then mapped to the five gondola-mounted thrusters as shown in Figure 6.9. For simplicity, we assume all motors for the planar movement are installed on the same plane. Then, we denote the frame $\{t\}$ shown in Figure 6.9 to describe the positions of the gondola-mounted thrusters. Due to the underactuated design of GT-MAB, the desired force and torque in the frame $\{t\}$ can be

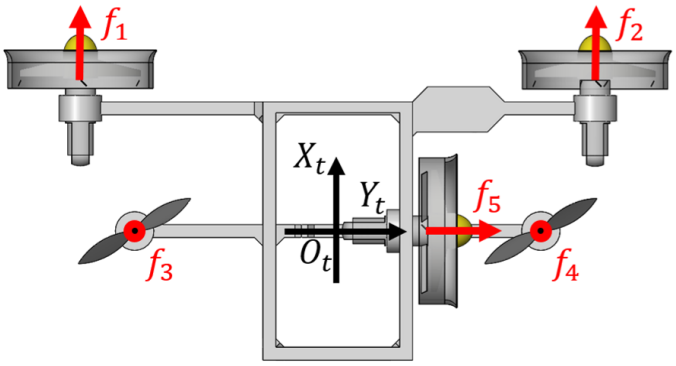

Figure 6.9: Top view of the gondola (GT-MAB 1.5) demonstrating the thruster configuration. Only the thrusters and the gondola frame are displayed for better illustration. We assume the forces f_1, f_2 and f_5 are all on the $O_tX_tY_t$ plane.

found as:

$$\begin{aligned} f_x^t &= f_x^g + \tau_y^g / r_{z,t/g}^b \\ f_y^t &= f_y^g - \tau_x^g / r_{z,t/g}^b \\ f_z^t &= f_z^g \\ \tau_z^t &= \tau_z^g, \end{aligned} \tag{6.11}$$

where $r_{z,t/g}^b$ is the vertical distance between thrusters and CG. Then the desired actuation is mapped to the five gondola-mounted thrusters. The mixer is designed as:

$$\begin{bmatrix} f_1 \\ f_2 \\ f_3 \\ f_4 \\ f_5 \end{bmatrix} = \begin{bmatrix} \frac{1}{2} & 0 & 0 & 0 & 0 & \frac{1}{2d_{1,f/t}} \\ \frac{1}{2} & 0 & 0 & 0 & 0 & \frac{-1}{2d_{2,f/t}} \\ 0 & 0 & -\frac{1}{2} & 0 & 0 & 0 \\ 0 & 0 & -\frac{1}{2} & 0 & 0 & 0 \\ 0 & 1 & 0 & 0 & 0 & 0 \end{bmatrix} \begin{bmatrix} f_x^t \\ f_y^t \\ f_z^t \\ \tau_x^t \\ \tau_y^t \\ \tau_z^t \end{bmatrix}, \tag{6.12}$$

where f_1 to f_5 are the propulsion force generated by the thrusters as denoted in Figure 6.9. $\boldsymbol{d}_{f/t} = [d_{1,f/t}, \ldots, d_{6,f/t}]^\top$ represents the orthogonal distance between each individual thrust force and the origin of $\{t\}$.

6.1.6 Experimental Results

An experiment is designed to compare the proposed method to the traditional station-keeping controller without swing reduction feature. The experiment is conducted in an indoor laboratory with perturbations including air conditioning and air flow from human movement. Ten ceiling-mounted localization cameras (OptiTrack) capture the pose of GT-MAB at 120Hz. The flight controllers and the ground-air communication also update at 120Hz.

We first fly the blimp using only the station-keeping controller by disabling the swing-reducing feature. Thus the control outputs τ_x^g and τ_y^g are both zero. The setpoints of the station-keeping controller are set to $\boldsymbol{r}_{p,g/n}^n = [0, 0, 1.4]^\top$ and $r_\psi = 0$ to keep GT-MAB hovering at the center of the indoor lab. As observed in Figure 6.10, GT-MAB starts swinging severely within 20 seconds. As discussed in Chapter 6.1.4, this swing oscillation is due to the damping in roll and pitch dynamics being insufficient to cancel the undesired torque from the underactuated configuration of GT-MAB.

With the same experimental setup, we conduct the test with the swing-reducing controller engaged. Figure 6.10 compares the roll and pitch angle of GT-MAB with and without the swing stabilization controller during the first 25 seconds of flight. The figure demonstrates the swing oscillation of GT-MAB is effectively stabilized after the swing-reducing controller is engaged. The variances of the roll and pitch angles of this flight test are also compared in Table 6.1.

The experiment is then repeated multiple times to further verify the purposed controller design. Ten un-stabilized tests with total flight time of 347 seconds, and three swing-stabilized tests with total of 1198 seconds are performed. As compared in Table 6.1, despite the increased environmental disturbances due to longer flight duration, the variances of both roll and pitch angles can be reduced by approximately two magnitudes with the engagement of the swing-reducing controller. A video demonstration of the flight test can be viewed at: `https://youtu.be/d5UKV-dcpZg`.

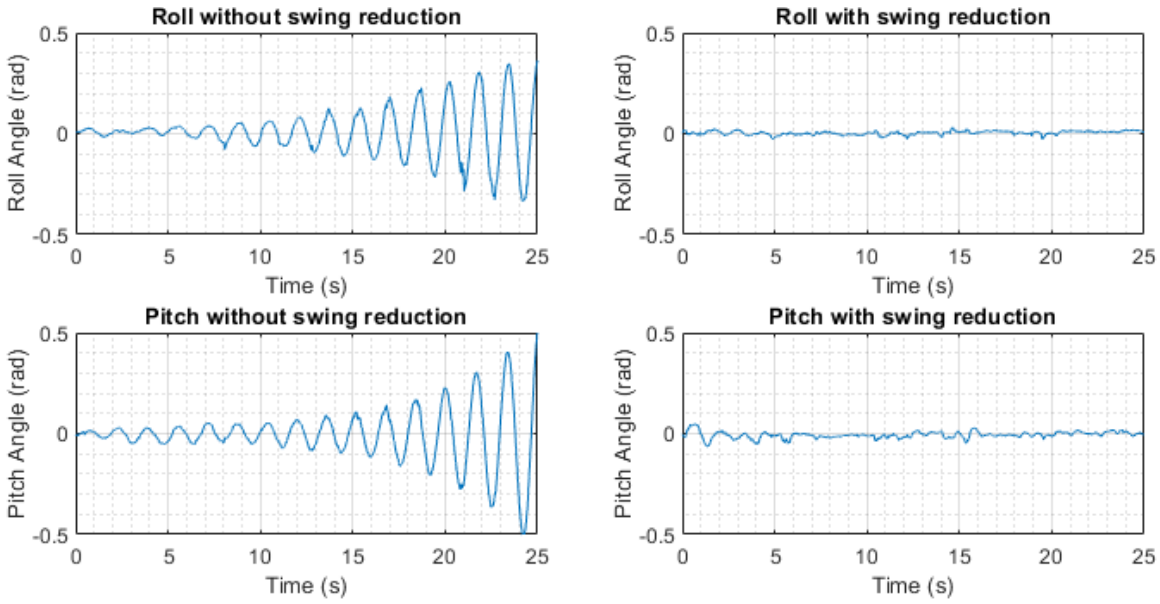

Figure 6.10: Comparison of the roll and pitch angle of GT-MAB with and without swing-reducing controller.

Table 6.1: Variance of the roll and pitch angles during hovering flight

Parameters	Without Swing-Reduction	With Swing-Reduction
Var. Roll (25s)	0.0133 rad^2	8.1502e-05 rad^2
Var. Pitch (25s)	0.0174 rad^2	2.5425e-04 rad^2
Var. Roll (Total of 347s)	0.0233 rad^2	5.5164e-04 rad^2
Var. Pitch (Total of 1198s)	0.0271 rad^2	3.1007e-04 rad^2

6.2 Swing-Reducing for Cruising Flight

Chapter 4.7 presents the waypoint navigation control of GT-MAB by decomposing its movement into a set of motion primitives (FCS 1.0). However, lateral and longitudinal oscillation is often observed due to the unique design of indoor blimps and the lack of swing-stabilization capability. To reduce this undesired oscillation, Chapter 6.1 discussed the control system design that stabilizes the swing oscillation during hovering flight (FCS 1.5). However, this control system cannot stabilize the oscillation in cruising flight. The dynamics of the swing motion becomes significantly more complicated for cruising, since there is a strong coupling between the translational and rotational movements.

In this section, the swing stabilization feature is expanded to cruising flight. The controller incorporates the latest motion model identified in Chapter 5.2, which includes the coupling between the translational and rotational movements into consideration. The flight controller can stabilize the swing oscillation while tracking the desired cruising velocity. Experimental results show that the control system is robust in the face of large disturbance. The proposed controller design establishes the foundation of the latest flight control system (FCS 2.0) discussed in Chapter 6.3.

6.2.1 Motion Model at CG

Chapter 5.2 has identified the motion model for the coupled translational and rotational movements of GT-MAB. Owing to the symmetrical design of GT-MAB around its vertical axis, the 6-DOF motion of the blimp can be simplified to 3-DOF movement on a vertical plane, as illustrated in Figure 6.11. Recall the results from Chapter 5.2, the identified

motion model of GT-MAB is:

$$
\begin{aligned}
&(m_{RB}+m_{Ax})\dot{v}^b_{x,b/n}+m_{RB}r^b_{z,g/b}\dot{\omega}^b_{y,b/n}\\
&+(m_{RB}+m_{Az})v^b_{z,b/n}\omega^b_{y,b/n}+D^{CB}_{vx}v^b_{x,b/n}=f^b_x\\
&(m_{RB}+m_{Az})\dot{v}^b_{z,b/n}-m_{RB}r^b_{z,g/b}(\omega^b_{y,b/n})^2\\
&-(m_{RB}+m_{Ax})v^b_{x,b/n}\omega^b_{y,b/n}+D^{CB}_{vz}v^b_{z,b/n}=f^b_z\\
&I_y\dot{\omega}^b_{y,b/n}+m_{RB}r^b_{z,g/b}(\dot{v}^b_{x,b/n}+v^b_{z,b/n}\omega^b_{y,b/n})+D^{CB}_{\omega y}\omega^b_{y,b/n}\\
&+(m_{Ax}-m_{Az})v^b_{x,b/n}v^b_{z,b/n}+r^b_{z,g/b}m_{RB}g\sin(\theta)=\tau^b_y.
\end{aligned}
\tag{6.13}
$$

In Chapter 5.1.1, we justified the assumption that center of gravity position is the pivot of the rotational motion. The advantages of incorporating CG position in controller design is discussed in Chapter 6.1.3. Therefore, with the system transformation matrix described in [59], we can represent the motion model of GT-MAB, Eq. (6.13), at the CG position as:

$$
\begin{aligned}
&(m_{RB}+m_{Ax})\dot{v}^b_{x,g/n}-m_{Ax}r^b_{z,g/b}\dot{\omega}^b_{y,g/n}+D^{CB}_{vx}v^b_{x,g/n}\\
&+(m_{RB}+m_{Az})v^b_{z,g/n}\omega^b_{y,g/n}-D^{CB}_{vx}\omega^b_{y,g/n}r^b_{z,g/b}=f^g_x\\
&(m_{RB}+m_{Az})\dot{v}^b_{z,g/n}+m_{Ax}r^b_{z,g/b}(\omega^b_{y,g/n})^2+D^{CB}_{vz}v^b_{z,g/n}\\
&-(m_{RB}+m_{Ax})v^b_{x,g/n}\omega^b_{y,g/n}=f^g_z\\
&I^{CG}_y\dot{\omega}^b_{y,g/n}-m_{Ax}v^b_{z,g/n}\omega^b_{y,g/n}r^b_{z,g/b}-D^{CB}_{vx}r^b_{z,g/b}v^b_{x,g/n}\\
&+(m_{Ax}-m_{Az})v^b_{x,g/n}v^b_{z,g/n}+(D^{CB}_{vx}{r^b_{z,g/b}}^2+D^{CB}_{\omega y})\omega^b_{y,g/n}\\
&-m_{Ax}r^b_{z,g/b}\dot{v}^b_{x,g/n}+gm_{RB}r^b_{z,g/b}\sin(\theta)=\tau^g_y.
\end{aligned}
\tag{6.14}
$$

The motion model in Eq. (6.14) needs to be written in the state-space form for future analysis and controller design. Thus, we define the state variables and system inputs as:

$$
\begin{aligned}
\boldsymbol{x}&=\left[v^b_{x,g/n},v^b_{z,g/n},\theta,\omega^b_{y,g/n}\right]^\top\\
\boldsymbol{u}&=\left[f^g_x,f^g_z,\tau^g_y\right]^\top.
\end{aligned}
\tag{6.15}
$$

Then, the state function at CG, $\dot{\boldsymbol{x}} = \boldsymbol{f}(\boldsymbol{x})$, can be found as:

$$
\begin{aligned}
\dot{x}_1 &= \frac{D_{vx}^{CB} m_{Ax} {r_{z,g/b}^b}^2 x_1 - D_{vx}^{CB} I_y^{CG} x_1 - {m_{Ax}}^2 r_{z,g/b}^b x_1 x_2 - I_y^{CG} m_z x_2 x_4 + {m_{Ax}}^2 {r_{z,g/b}^b}^2 x_2 x_4}{-{m_{Ax}}^2 {r_{z,g/b}^b}^2 + I_y^{CG} m_x} \\
&+ \frac{g m_{Ax} m_{RB} {r_{z,g/b}^b}^2 \sin(x_3) + D_{vx}^{CB} m_{Ax} {r_{z,g/b}^b}^3 x_4 - D_{vx}^{CB} I_y^{CG} r_{z,g/b}^b x_4 + D_{\omega y}^{CB} m_{Ax} r_{z,g/b}^b x_4}{{m_{Ax}}^2 {r_{z,g/b}^b}^2 - I_y^{CG} m_x} \\
&+ \frac{m_{Ax} m_{Az} r_{z,g/b}^b x_1 x_2 + I_y^{CG} u_1 + m_{Ax} r_{z,g/b}^b u_3}{-{m_{Ax}}^2 {r_{z,g/b}^b}^2 + I_y^{CG} m_x} \\
\dot{x}_2 &= \frac{(m_x x_1 x_4 - m_{Ax} r_{z,g/b}^b x_4^2) - D_{vz}^{CB} x_2 + u_2}{m_z} \\
\dot{x}_3 &= x_4 \\
\dot{x}_4 &= \frac{D_{vx}^{CB} m_{RB} r_{z,g/b}^b x_1 - m_x (m_x - m_z) x_1 x_2 + {m_{Ax}}^2 r_{z,g/b}^b x_2 x_4 - m_{Ax} m_{Az} r_{z,g/b}^b x_2 x_4}{-{m_{Ax}}^2 {r_{z,g/b}^b}^2 + I_y^{CG} m_x} \\
&+ \frac{-g m_x m_{RB} r_{z,g/b}^b \sin(x_3) - D_{vx}^{CB} m_{RB} {r_{z,g/b}^b}^2 x_4 - D_{\omega y}^{CB} m_x x_4}{-{m_{Ax}}^2 {r_{z,g/b}^b}^2 + I_y^{CG} m_x} \\
&+ \frac{m_{Ax} r_{z,g/b}^b u_1 + m_x u_3}{-{m_{Ax}}^2 {r_{z,g/b}^b}^2 + I_y^{CG} m_x}.
\end{aligned}
\tag{6.16}
$$

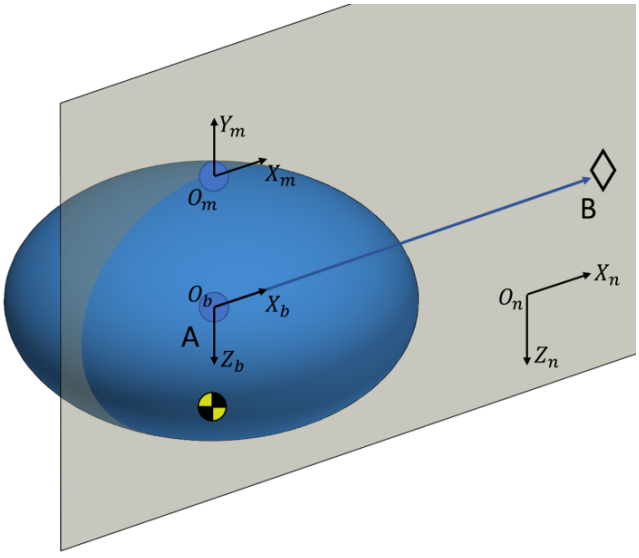

Figure 6.11: Motion of GT-MAB reduced to 3-DOF on a vertical plane.

6.2.2 Model Simplification

Given the limited ceiling heights in most indoor environments, miniature blimps usually stay at constant altitude inside a room. Therefore, we decouple the heave motion with the planar movement of the blimp. These two motions are analyzed and controlled independently, and combined together to navigate the blimp in 3D space.

- **Planar movement**. In this mode, blimp flies horizontally with zero vertical velocity:

$$v^b_{z,g/n} = \dot{v}^b_{z,g/n} = 0. \tag{6.17}$$

Therefore, the motion model from Eq. (6.14) can be simplified as:

$$\begin{aligned}
&(m_{RB} + m_{Ax})\dot{v}^b_{x,g/n} - m_{Ax} r^b_{z,g/b} \dot{\omega}^b_{y,g/n} \\
&+ D^{CB}_{vx} v^b_{x,g/n} - D^{CB}_{vx} \omega^b_{y,g/n} r^b_{z,g/b} = f^g_x \\
&I^{CG}_y \dot{\omega}^b_{y,g/n} + (D^{CB}_{vx} {r^b_{z,g/b}}^2 + D^{CB}_{\omega y}) \omega^b_{y,g/n} - m_{Ax} r^b_{z,g/b} \dot{v}^b_{x,g/n} \\
&- D^{CB}_{vx} r^b_{z,g/b} v^b_{x,g/n} + g m_{RB} r^b_{z,g/b} \sin(\theta) = \tau^g_y.
\end{aligned} \tag{6.18}$$

Next, we derive the state equations for the planar motion model. The system states and inputs of the planar movement are defined as:

$$\begin{aligned}
\boldsymbol{x}_p &= \left[v^b_{x,g/n}, \theta, \omega^b_{y,g/n} \right]^\top \\
\boldsymbol{u}_p &= \left[f^g_x, \tau^g_y \right]^\top .
\end{aligned} \tag{6.19}$$

Then, the state function of the planar motion at CG, $\dot{\boldsymbol{x}}_p = \boldsymbol{f}_p(\boldsymbol{x}_p)$, can be found as:

$$\begin{aligned}
\dot{x}_{p1} &= \frac{D_{vx}^{CB} m_{Ax} {r_{z,g/b}^b}^2 x_{p1} - D_{vx}^{CB} I_y^{CG} x_{p1} - g m_{Ax} m_{RB} {r_{z,g/b}^b}^2 \sin(x_{p2})}{-{m_{Ax}}^2 {r_{z,g/b}^b}^2 + I_y^{CG} m_x} \\
&\quad + \frac{D_{vx}^{CB} I_y^{CG} r_{z,g/b}^b x_{p3} - D_{vx}^{CB} m_{Ax} {r_{z,g/b}^b}^3 x_{p3} - D_{\omega y}^{CB} m_{Ax} r_{z,g/b}^b x_{p3}}{-{m_{Ax}}^2 {r_{z,g/b}^b}^2 + I_y^{CG} m_x} \\
&\quad + \frac{I_y^{CG} u_{p1} + m_{Ax} r_{z,g/b}^b u_{p2}}{-{m_{Ax}}^2 {r_{z,g/b}^b}^2 + I_y^{CG} m_x} \\
\dot{x}_{p2} &= x_{p3} \\
\dot{x}_{p3} &= \frac{D_{vx}^{CB} m_{RB} r_{z,g/b}^b x_{p1} - D_{\omega y}^{CB} m_x x_{p3} - D_{vx}^{CB} m_{RB} {r_{z,g/b}^b}^2 x_{p3}}{-{m_{Ax}}^2 {r_{z,g/b}^b}^2 + I_y^{CG} m_x} \\
&\quad + \frac{-g m_x m_{RB} r_{z,g/b}^b \sin(x_{p2}) + m_{Ax} r_{z,g/b}^b u_{p1} + m_x u_{p2}}{-{m_{Ax}}^2 {r_{z,g/b}^b}^2 + I_y^{CG} m_x}.
\end{aligned} \tag{6.20}$$

- **Vertical movement**. In this mode, the heave movement is the dominant motion of the blimp. Therefore, the motion model in Eq. (6.14) can be simplified as:

$$f_z^g = (m_{RB} + m_{Az}) \dot{v}_{z,g/n}^b + D_{vz}^{CB} v_{z,g/n}^b. \tag{6.21}$$

Next, we define the state variable and system input of the vertical motion as:

$$\begin{aligned}
x_v &= v_{z,g/n}^b \\
u_v &= f_z^g.
\end{aligned} \tag{6.22}$$

The state function can be represented as:

$$\dot{x}_v = \frac{-D_{vz}^{CB}}{m_{RB} + m_{Az}} x_v + \frac{1}{m_{RB} + m_{Az}} u_v. \tag{6.23}$$

6.2.3 Steady-State Analysis

Equilibrium condition calculation

Here we evaluate the steady-state operating condition of the blimp during cruising flight. We find the steady-state values of system states under constant inputs $f^g_{x,0}$, $f^g_{z,0}$, and $\tau^g_{y,0}$. Since the system states remain constant at the equilibrium, we have:

$$\begin{aligned} \boldsymbol{x}_0 &= \left[v^b_{x,g/n,0}, v^b_{z,g/n,0}, \theta_0, \omega^b_{y,g/n,0} \right]^\top \\ &= \left[v^b_{x,g/n,0}, v^b_{z,g/n,0}, \theta_0, 0 \right]^\top \\ \dot{\boldsymbol{x}}_0 &= \left[0, 0, 0, 0 \right]^\top . \end{aligned} \tag{6.24}$$

Substituting Eq. (6.24) to the 3-DOF motion model described in Eq. (6.14), we can find:

$$\begin{aligned} D^{CB}_{vx} v^b_{x,g/n,0} &= f^g_{x,0} \\ D^{CB}_{vz} v^b_{z,g/n,0} &= f^g_{z,0} \\ -D^{CB}_{vx} r^b_{z,g/b} v^b_{x,g/n,0} + r^b_{z,g/b} m_{RB} g \sin(\theta_0) &= \tau^g_{y,0}, \end{aligned} \tag{6.25}$$

where, $v^b_{x,g/n,0}$, $v^b_{z,g/n,0}$ and θ_0 are the equilibrium velocities and pitch angle given constant inputs. Due to the underactuated design of GT-MAB, we have

$$\tau^g_{y,0} = r^b_{z,t/g} f^g_{x,0}. \tag{6.26}$$

Then the relationship between the forward thrust, the equilibrium pitch angle, and the equilibrium velocity can be found as:

$$\begin{aligned} f^g_{x,0} &= \frac{r^b_{z,g/b} m_{RB} g}{r^b_{z,t/b}} \sin(\theta_0) \\ \theta_0 &= \arcsin\left(\frac{D^{CB}_{vx} r^b_{z,t/b}}{r^b_{z,g/b} m_{RB} g} v^b_{x,g/n,0}\right). \end{aligned} \tag{6.27}$$

Stability at equilibrium point

Now we investigate the stability of the system at the equilibrium point. We first define the deviation between the actual system state value and the equilibrium as:

$$\begin{aligned}\Delta \boldsymbol{x} &= \boldsymbol{x} - \boldsymbol{x}_0 \\ &= \left[v^b_{x,g/n} - v^b_{x,g/n,0}, v^b_{z,g/n} - v^b_{z,g/n,0}, \theta - \theta_0, \omega^b_{y,g/n} - \omega^b_{y,g/n,0} \right]^\top \\ \Delta \boldsymbol{u} &= \boldsymbol{u} - \boldsymbol{u}_0 \\ &= \left[f^g_x - f^g_{x,0}, f^g_z - f^g_{z,0}, \tau^g_y - \tau^g_{y,0} \right]^\top .\end{aligned} \tag{6.28}$$

Then we can linearize the state equations around the equilibrium:

$$\boldsymbol{f}(\boldsymbol{x}_0 + \Delta \boldsymbol{x}) = \partial \boldsymbol{f} / \partial \boldsymbol{x}|_{\boldsymbol{x}=\boldsymbol{x}_0} \Delta \boldsymbol{x} + \text{higher order terms} \cdot \tag{6.29}$$

The Jacobian matrix at equilibrium $\boldsymbol{x}_0$ can be defined as:

$$\boldsymbol{J} = \partial \boldsymbol{f} / \partial \boldsymbol{x}|_{\boldsymbol{x}=\boldsymbol{x}_0} = \begin{bmatrix} J_{11} & J_{12} & J_{13} & J_{14} \\ J_{21} & J_{22} & J_{23} & J_{24} \\ J_{31} & J_{32} & J_{33} & J_{34} \\ J_{41} & J_{42} & J_{43} & J_{44} \end{bmatrix}. \tag{6.30}$$

Each element of the Jacobian matrix is expanded in Eq. (C.2) of Appendix C. With the parameters identified from Chapter 5, the Jacobian matrix can be numerically calculated. All eigenvalues of the $\boldsymbol{J}$ have negative real parts, which indicates the system is stable at the equilibrium point.

Similarly, for the planar motion, we define the small derivation near the equilibrium as:

$$
\begin{aligned}
\Delta \boldsymbol{x}_p &= \boldsymbol{x}_p - \boldsymbol{x}_{p,0} \\
&= \left[v^b_{x,g/n} - v^b_{x,g/n,0}, \theta - \theta_0, \omega^b_{y,g/n} - \omega^b_{y,g/n,0} \right]^\top \\
\Delta \boldsymbol{u}_p &= \boldsymbol{u}_p - \boldsymbol{u}_{p,0} \\
&= \left[f^g_x - f^g_{x,0}, \tau^g_y - \tau^g_{y,0} \right]^\top .
\end{aligned}
\tag{6.31}
$$

Then we find the Jacobian matrix of the planar motion at equilibrium $\boldsymbol{x}_{p,0}$ as:

$$
\boldsymbol{J}_p = \partial \boldsymbol{f}_p / \partial \boldsymbol{x}_p |_{\boldsymbol{x}_p = \boldsymbol{x}_{p,0}} = \begin{bmatrix} J_{p,11} & J_{p,12} & J_{p,13} \\ J_{p,21} & J_{p,22} & J_{p,23} \\ J_{p,31} & J_{p,32} & J_{p,33} \end{bmatrix} . \tag{6.32}
$$

Each element of the Jacobian matrix is expanded in Eq. (C.1) of Appendix C. $\boldsymbol{J}_p$ can be numerically calculated with the parameters identified from Chapter 5. All eigenvalues of the $\boldsymbol{J}_p$ have negative real part, which indicates the system is stable at the operating point.

For the vertical movement, recall the state equation:

$$
\dot{x}_v = -\frac{D^{CB}_{vz}}{m_{RB} + m_{Az}} x_v + \frac{1}{m_{RB} + m_{Az}} u_v . \tag{6.33}
$$

With both D^{CB}_{vz} and $m_{RB} + m_{Az}$ greater than zero, this linear system is stable.

6.2.4 Planar Motion Control

Due to the underactuated design, the planar motion of GT-MAB is coupled with the rotational movement of the blimp. However, adjustment of the attitude is significantly faster than changing the translational velocity. Therefore, as shown in Figure 6.12, we design a control system with nested loops. The inner loop tracks the desired attitude calculated by the outer loop, while the outer loop adjusts the setpoint attitude to track the desired velocity.

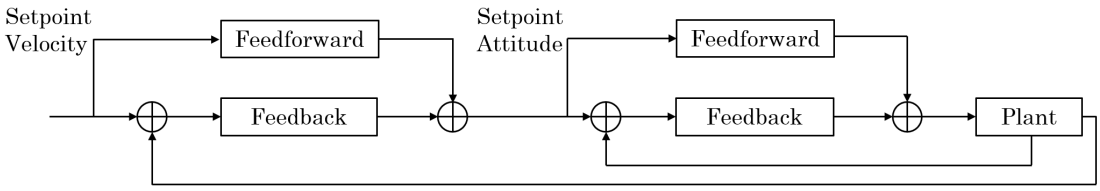

Figure 6.12: Block diagram of the nested-loop controller that tracks the attitude and planar motion velocity. The full diagram of the control system is shown in Figure 6.29.

Attitude tracking

Given that adjusting the attitude of GT-MAB is significantly faster than changing the translational velocity, we assume the velocity remains at constant for the inner loop design. Thus, the state equations of the planar motion, Eq. (6.20), can be simplified as:

$$\begin{aligned}
\dot{x}_{p1} &= 0 \\
\dot{x}_{p2} &= x_{p3} \\
\dot{x}_{p3} &= \frac{D_{vx}^{CB} m_{RB} r_{z,g/b}^{b} x_{p1,0} - D_{\omega y}^{CB} m_x x_{p3} - D_{vx}^{CB} m_{RB} {r_{z,g/b}^{b}}^2 x_{p3}}{-{m_{Ax}}^2 {r_{z,g/b}^{b}}^2 + I_y^{CG} m_x} \\
&\quad + \frac{-g m_x m_{RB} r_{z,g/b}^{b} \sin(x_{p2}) + m_{Ax} r_{z,g/b}^{b} u_{p1} + m_x u_{p2}}{-{m_{Ax}}^2 {r_{z,g/b}^{b}}^2 + I_y^{CG} m_x}.
\end{aligned} \tag{6.34}$$

As discussed in Chapter 6.2.3, we can find the equilibrium pitch angle while the GT-MAB is traveling at a constant surge velocity. This is the operating point of the attitude tracking controller. Then, we find the dynamics at the operating point regarding $\Delta \boldsymbol{x}_p$ by substituting Eq. (6.31) to the state equations Eq. (6.34):

$$\begin{aligned}
\Delta\dot{x}_{p2} &= \Delta x_{p3} \\
\Delta\dot{x}_{p3} &= -\frac{g m_x m_{RB} r_{z,g/b}^{b} \sin(\Delta x_{p2} + x_{p2,0}) + D_{\omega y}^{CB} m_x \Delta x_{p3} + D_{vx}^{CB} m_{RB} {r_{z,g/b}^{b}}^2 \Delta x_{p3}}{-{m_{Ax}}^2 {r_{z,g/b}^{b}}^2 + I_y^{CG} m_x} \\
&\quad + \frac{g m_x m_{RB} r_{z,g/b}^{b} \sin(x_{p2,0})}{-{m_{Ax}}^2 {r_{z,g/b}^{b}}^2 + I_y^{CG} m_x} + \frac{m_{Ax} r_{z,g/b}^{b} \Delta u_{p1} + m_x \Delta u_{p2}}{-{m_{Ax}}^2 {r_{z,g/b}^{b}}^2 + I_y^{CG} m_x}.
\end{aligned} \tag{6.35}$$

Since the pitch angle at the operating point is small, Eq. (6.35) can be simplified with $\sin(\theta) \approx \theta$:

$$\begin{aligned}
\Delta\dot{x}_{p2} &= \Delta x_{p3} \\
\Delta\dot{x}_{p3} &= -\frac{g m_x m_{RB} r^b_{z,g/b} \Delta x_{p2} + D^{CB}_{\omega y} m_x \Delta x_{p3} + D^{CB}_{vx} m_{RB} {r^b_{z,g/b}}^2 \Delta x_{p3}}{-{m_{Ax}}^2 {r^b_{z,g/b}}^2 + I^{CG}_y m_x} \\
&\quad + \frac{m_{Ax} r^b_{z,g/b} \Delta u_{p1} + m_x \Delta u_{p2}}{-{m_{Ax}}^2 {r^b_{z,g/b}}^2 + I^{CG}_y m_x}.
\end{aligned} \tag{6.36}$$

Due to the underactuated design of GT-MAB as described in Eq. (6.26), the system inputs Δu_{p1} and Δu_{p2} satisfy:

$$\Delta u_{p2} = r^b_{z,t/g} \Delta u_{p1}. \tag{6.37}$$

Then Eq. (6.36) can be written as:

$$\begin{aligned}
\Delta\dot{x}_{p2} &= \Delta x_{p3} \\
\Delta\dot{x}_{p3} &= -\frac{g m_x m_{RB} r^b_{z,g/b} \Delta x_{p2} + D^{CB}_{\omega y} m_x \Delta x_{p3} + D^{CB}_{vx} m_{RB} {r^b_{z,g/b}}^2 \Delta x_{p3}}{-{m_{Ax}}^2 {r^b_{z,g/b}}^2 + I^{CG}_y m_x} \\
&\quad + \frac{(m_{Ax} r^b_{z,g/b} + m_x r^b_{z,t/g}) \Delta u_{p1}}{-{m_{Ax}}^2 {r^b_{z,g/b}}^2 + I^{CG}_y m_x}.
\end{aligned} \tag{6.38}$$

Given that the system described in Eq. (6.38) is linear, we design a state feedback controller to keep the pitch angle at the desired operating point.

$$\Delta u_{p1} = -k_\theta \Delta x_{p2} - k_\omega \Delta x_{p3}, \tag{6.39}$$

where k_θ and k_ω are the feedback gains for the angle and angular rate error separately. As described in Eq. (6.25), actuation $f^g_{x,0}$ is required for the blimp to stay at the equilibrium.

Therefore, the overall output of the inner-loop controller is:

$$\begin{aligned} u_{p1} &= u_{p1,0} + \Delta u_{p1} \\ &= f^g_{x,0} - k_\theta \Delta x_{p2} - k_\omega \Delta x_{p3} \\ &= \frac{r^b_{z,g/b} m_{RB} g \sin(\theta_0)}{r^b_{z,t/b}} - k_\theta \Delta x_{p2} - k_\omega \Delta x_{p3}. \end{aligned} \tag{6.40}$$

The inner-loop attitude-tracking controller is validated experimentally as shown in Figure 6.13. External disturbance is added to evaluate the robustness of the proposed controller design. One video demonstration of the experiment is available at `https://youtu.be/jC5Q29GI0HY`.

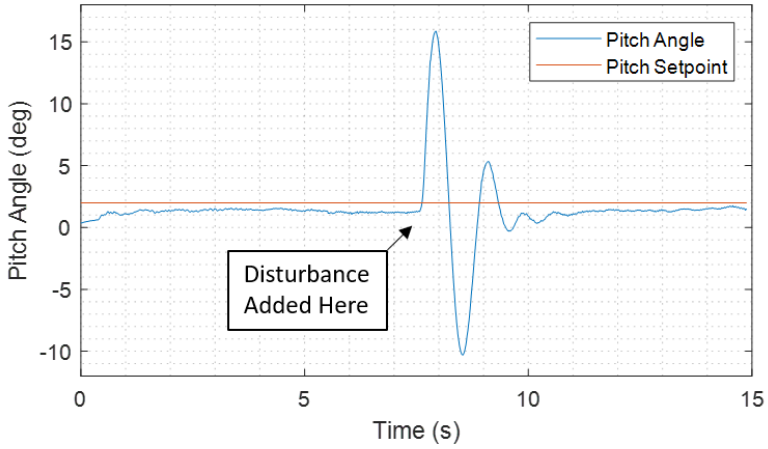

Figure 6.13: Attitude tracking of GT-MAB with added disturbance.

Velocity tracking

The velocity controller tracks the desired velocity of GT-MAB by adjusting the setpoint attitude of the inner-loop controller. Given that the inner loop is significantly faster compared to the outer loop, we assume the attitude is constant for velocity-tracking controller design. With this assumption, and the relationship between f^g_x and τ^g_y described in Eq. (6.26), the

planar motion model in Eq. (6.20), can be simplified as:

$$\dot{x}_{p1} = -\frac{D_{vx}^{CB} r_{z,g/b}^{b} + D_{vx}^{CB} r_{z,t/g}^{b}}{r_{z,t/g}^{b} m_x + r_{z,g/b}^{b} m_{Ax}} x_{p1} + \frac{g m_{RB} r_{z,g/b}^{b}}{r_{z,t/g}^{b} m_x + r_{z,g/b}^{b} m_{Ax}} \sin(x_{p2}). \tag{6.41}$$

Then, we linearize the dynamics at the operating point described in Eq. (6.31). With small angle approximation, $\sin(\theta) \approx \theta$, Eq. (6.41) can be linearized as:

$$\Delta\dot{x}_{p1} = -\frac{D_{vx}^{CB} r_{z,g/b}^{b} + D_{vx}^{CB} r_{z,t/g}^{b}}{r_{z,t/g}^{b} m_x + r_{z,g/b}^{b} m_{Ax}} \Delta x_{p1} + \frac{g m_{RB} r_{z,g/b}^{b}}{r_{z,t/g}^{b} m_x + r_{z,g/b}^{b} m_{Ax}} \Delta x_{p2}. \tag{6.42}$$

To track the desired velocity and eliminate steady-state error, a PI feedback controller is implemented:

$$\theta_{feedback} = -k_{pv} e_{vx,g/n}^{b} - k_{iv} \int_0^t e_{vx,g/n}^{b} dt', \tag{6.43}$$

where $e_{vx,g/n}^{b} = r_{vx,g/n}^{b} - v_{x,g/n}^{b}$ is the velocity error in X_g direction, and $r_{vx,g/n}^{b}$ is the setpoint velocity. k_{pv} and k_{iv} represent the gains of the PI controller. Therefore, the setpoint angle for the inner loop is:

$$\begin{aligned} \theta_0 &= \theta_{feedforward} + \theta_{feedback} \\ &= \arcsin\left(\frac{D_{vx}^{CB} r_{z,t/b}^{b}}{r_{z,g/b}^{b} m_{RB} g} r_{vx,g/n}^{b}\right) - k_{pv} e_{vx,g/n}^{b} - k_{iv} \int_0^t e_{vx,g/n}^{b} dt'. \end{aligned} \tag{6.44}$$

A series of experiments are designed to validate the proposed velocity-tracking controller. Test flights with setpoint velocities of 0.05m/s, 0.1m/s, 0.15m/s, 0.2m/s, 0.25m/s, and 0.3m/s are conducted. The experimental data with 0.1m/s setpoint velocity is shown in Figure 6.14, and the remaining test results can be seen in Appendix D. A video demonstration of the experiments can be seen at `https://youtu.be/XY_MQAcMWJE`. The proposed velocity-tracking controller is also validated with added disturbance. As shown in Figure 6.15, the controller can recover quickly from the disturbance. One video demonstration of this test is available at `https://youtu.be/b6KxRN2wAQs`.

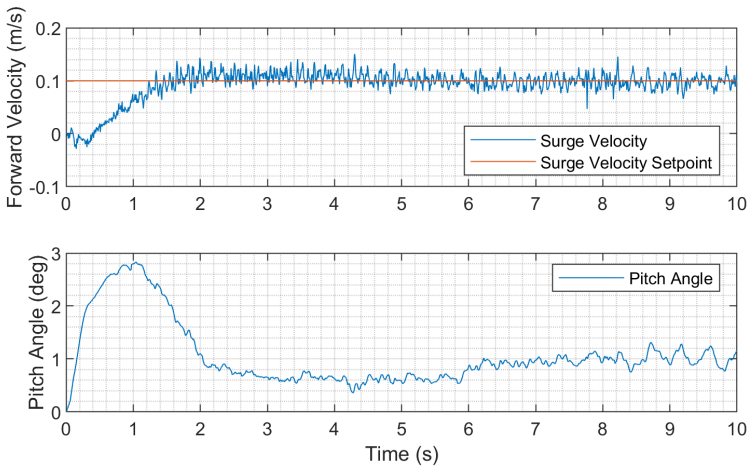

Figure 6.14: Forward velocity control with setpoint 0.1m/s.

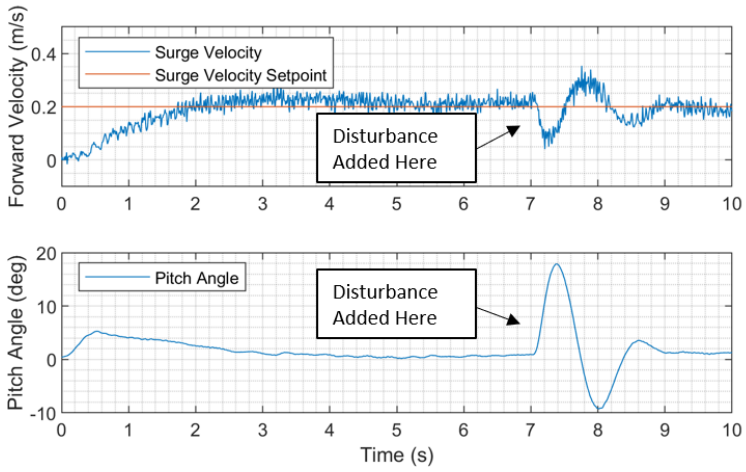

Figure 6.15: Forward velocity control with setpoint 0.2m/s and added disturbance.

6.2.5 Vertical Motion Control

The envelope of the GT-MAB has significant impact on its vertical thrusters. As illustrated in Figure 6.16, the actuation effort is highly asymmetrical for the vertical movement. When the vertical motors are propelling downward, the exhaust airflow will be blocked and deflected by the envelope, leading to loss in thrust. The exhaust is free from blockage when the vertical motors are propelling upward. Therefore, a model predictive controller (MPC) is designed that takes the asymmetrical actuation into consideration.

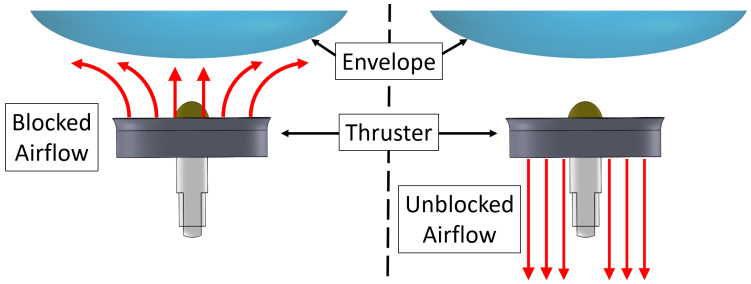

Figure 6.16: The thrust-hull interaction causes asymmetrical actuation in the vertical direction.

Motion model for altitude tracking

Recall the motion model of the heave movement of the GT-MAB described in Eq. (6.23):

$$\dot{x}_v = -\frac{D_{vz}^{CB}}{m_{RB} + m_{Az}} x_v + \frac{1}{m_{RB} + m_{Az}} u_v. \tag{6.45}$$

This model is defined in the body frame of GT-MAB, and needs to be converted to the inertial frame for altitude tracking. Given that the roll and pitch angles are small under the planar motion controller, we apply the approximations $\cos(\cdot) \approx 1$ and $\sin(\cdot) \approx 0$. Then, the vertical velocity in the inertial frame can be found as:

$$\begin{aligned} \dot{\boldsymbol{p}}_{g/n}^{n} &= \boldsymbol{R}_{g}^{n}(\boldsymbol{\Theta}_{ng}) \boldsymbol{v}_{g/n}^{b} = \begin{bmatrix} \cos(\psi), & -\sin(\psi), & 0 \\ \sin(\psi), & \cos(\psi), & 0 \\ 0, & 0, & 1 \end{bmatrix} \boldsymbol{v}_{g/n}^{b} \\ \dot{p}_{z,g/n}^{n} &= v_{z,g/n}^{b} = x_v. \end{aligned} \tag{6.46}$$

Therefore, we can describe the vertical motion in the inertial frame as:

$$\begin{bmatrix} \dot{p}_{z,g/n}^{n} \\ \ddot{p}_{z,g/n}^{n} \end{bmatrix} = \begin{bmatrix} 0 & 1 \\ 0 & -D_{vz}^{CB}/(m_{RB} + m_{Az}) \end{bmatrix} \begin{bmatrix} p_{z,g/n}^{n} \\ \dot{p}_{z,g/n}^{n} \end{bmatrix} + \begin{bmatrix} 0 \\ 1/(m_{RB} + m_{Az}) \end{bmatrix} u_v. \tag{6.47}$$

MPC controller design

The MPC controller is constructed with the cost function below:

$$J_{mpc}\left(\boldsymbol{U}_k\right) = J_y\left(\boldsymbol{U}_k\right) + J_{\Delta u}\left(\boldsymbol{U}_k\right), \tag{6.48}$$

where $J_y\left(\boldsymbol{U}_k\right)$ and $J_{\Delta u}\left(\boldsymbol{U}_k\right)$ are the cost terms for reference tracking and controller output smoothing. $\boldsymbol{U}_k$ is the quadratic program (QP) decision at controller time step k:

$$\boldsymbol{U}_k = \left[u_v(k), u_v(k+1), \cdots u_v(k+N_p-1)\right]^\top, \tag{6.49}$$

where u_v is the controller output for the vertical motion. N_p is the prediction horizon. The cost function term for the altitude tracking error is defined as:

$$J_y\left(\boldsymbol{U}_k\right) = \sum_{i=1}^{N_p} \left\{ w_y \left[r^n_{pz,g/n}(k+i) - p^n_{z,g/n}(k+i) \right] \right\}^2, \tag{6.50}$$

where $r^n_{pz,g/n}(k+i)$ and $p^n_{z,g/n}(k+i)$ are the setpoint and predicted altitude at i-th prediction horizon step. w_y is the tuning weight for this cost function term. The cost function term $J_{\Delta u}$ is defined to suppress the sudden change in controller output. This can help the thrusters to better follow the controller output, and save energy by reducing high frequency movements. $J_{\Delta u}$ can be written as:

$$J_{\Delta u}\left(\boldsymbol{U}_k\right) = \sum_{i=0}^{N_p-1} \left\{ w_{\Delta u} \left[u_v(k+i) - u_v(k+i-1) \right] \right\}^2, \tag{6.51}$$

where $w_{\Delta u}$ is the tuning weight of this cost function term. The predicted control output outside the control horizon N_c is set to constant. A hard constraint is applied to reflect the physical limitations on maximum thrust that can be generated, as seen in Figure 6.22. Since the vehicle dynamics is linear and the cost function is quadratic, the MPC optimization problem can be solved by the quadratic programming method.

An experiment is conducted to compare the performance of the MPC altitude tracking against a PID controller. The tuning weight w_y and $w_{\Delta u}$ are set to the same value. The prediction and control horizons are 5 and 0.5 seconds separately. As shown in Figure 6.17, altitude control with PID has larger overshoot than MPC, due to asymmetric thrust profile. Moreover, the blimp, with MPC, climbs faster compared to that with PID. As illustrated in Figure 6.18, the thruster generates full upward thrust for faster climbing during the first 2.6 seconds. Once the blimp reaches approximately half of the setpoint altitude, full downward thrust is incorporated for around 2.8 seconds to reduce the overshoot.

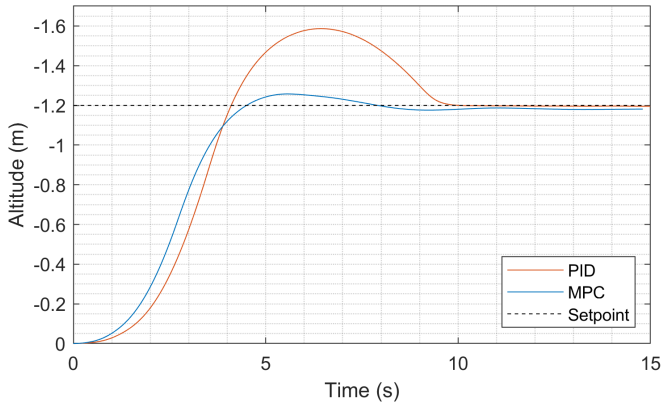

Figure 6.17: Step response of altitude control with MPC and PID controllers. Faster response and lower overshoot is observed with MPC. Vertical axis of the figure is reversed for better illustration.

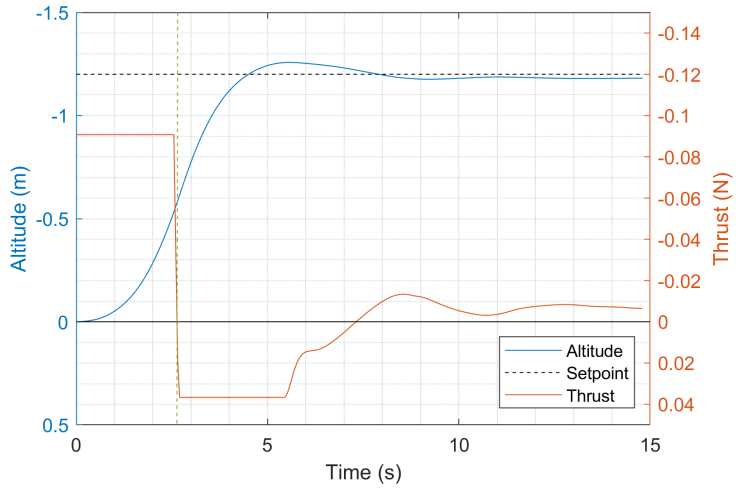

Figure 6.18: Controller output of the MPC controller. Full upward thrust is set for the first 2.6 seconds for faster climbing, and full downward propulsion is followed for 2.8 seconds to achieve lower overshoot.

6.2.6 Mixer and Thruster Compensation

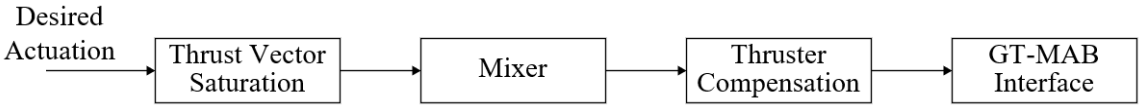

Figure 6.19: Block diagram illustrating major steps for generating the desired actuation.

The steps for generating the desired actuation $\boldsymbol{\tau}^g$ are shown in Figure 6.19. To begin with, we define the coordinate frame $\{t\}$ for the convenience of describing the force and torque generated by the gondola-mounted thrusters. As demonstrated in Figure 6.20, the origin of $\{t\}$ is defined on the plane that contains the shafts of the horizontal motors. Hence, due to the underactuated design of GT-MAB, the desired actuation in $\{t\}$ can be found from $\boldsymbol{\tau}^g$:

$$\begin{aligned} \boldsymbol{\tau}^t &= [f_x^t, f_y^t, f_z^t, \tau_x^t, \tau_y^t, \tau_z^t]^\top \\ &= [f_x^g, f_y^g, f_z^g, 0, 0, \tau_z^g]^\top. \end{aligned} \tag{6.52}$$

As discussed in Chapter 3.3, GT-MAB 2.0 features an unique X-shaped actuator configuration for symmetrical actuation that avoids reversing the motor direction. As shown in Figure 6.20, there are four horizontally-mounted thrusters generating forces f_1 to f_4 on the $O_tX_tY_t$ plane, and two vertically-mounted motors for propulsion f_5 to f_6 along Z_t axis. Given the thruster allocation of GT-MAB 2.0, we get the mapping between the propulsion force of individual thrusters and the desired actuation $\boldsymbol{\tau}^t$ as:

$$\begin{bmatrix} f_x^t \\ f_y^t \\ f_z^t \\ \tau_x^t \\ \tau_y^t \\ \tau_z^t \end{bmatrix} = \begin{bmatrix} -\frac{\sqrt{2}}{2} & \frac{\sqrt{2}}{2} & \frac{\sqrt{2}}{2} & -\frac{\sqrt{2}}{2} & 0 & 0 \\ \frac{\sqrt{2}}{2} & \frac{\sqrt{2}}{2} & -\frac{\sqrt{2}}{2} & -\frac{\sqrt{2}}{2} & 0 & 0 \\ 0 & 0 & 0 & 0 & -1 & -1 \\ 0 & 0 & 0 & 0 & 0 & 0 \\ 0 & 0 & 0 & 0 & 0 & 0 \\ d_{1,f/t} & -d_{2,f/t} & d_{3,f/t} & -d_{4,f/t} & 0 & 0 \end{bmatrix} \begin{bmatrix} f_1 \\ f_2 \\ f_3 \\ f_4 \\ f_5 \\ f_6 \end{bmatrix}, \tag{6.53}$$

where $\boldsymbol{d}_{f/t} = [d_{1,f/t}, \ldots, d_{6,f/t}]^\top$ represents the orthogonal distance between each thrust

force and O_t. Owing to the symmetrical design of the gondola, we have $d_{1,f/t} = d_{2,f/t} = d_{3,f/t} = d_{4,f/t} = 5.3$ cm.

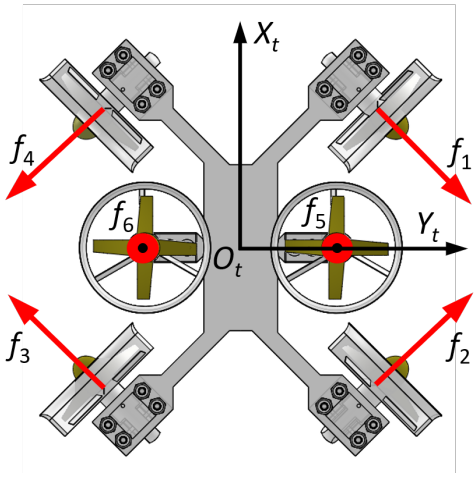

Figure 6.20: Top view of the gondola (GT-MAB 2.0) demonstrating the thruster configuration. Only the thrusters and the gondola frame are displayed for better illustration. The forces f_1, f_2, f_3 and f_4 are all on the $O_tX_tY_t$ plane.

Thrust vector saturation

GT-MAB 2.0 has flight controllers that track the heading, altitude, and the planar movement independently. Therefore, we design saturation functions for each controller output. From Eq. (6.53), f_z^t is the total thrust of the two vertically-mounted thrusters, thus

$$f_z^t = \Big[-1, -1\Big] \Big[f_5, f_6\Big]^\top. \tag{6.54}$$

Therefore, the saturation for f_z^t can be conveniently designed by examing the thrust range of the vertical motors as shown in Figure 6.22.

However, the actuation for the steering motion and the planar movement need to be generated from the combination of motor thrust forces f_1 to f_4. Given that GT-MAB 2.0 has symmetrical design with omnidirectional actuation, steering is not required for the blimp to fly towards a certain direction. As a result, the actuation requirement for steering motion is significantly reduced. Therefore, for each horizontally-mounted motor, we assign 20% of

its maximum thrust for steering maneuver, and the rest 80% is dedicated to the propulsion on $O_tX_tY_t$ plane. Thus, we group the motor thrust forces f_1 to f_4 into two groups as:

$$\begin{aligned}\begin{bmatrix} f_x^t \\ f_y^t \end{bmatrix} &= \begin{bmatrix} -\frac{\sqrt{2}}{2} & \frac{\sqrt{2}}{2} & \frac{\sqrt{2}}{2} & -\frac{\sqrt{2}}{2} \\ \frac{\sqrt{2}}{2} & \frac{\sqrt{2}}{2} & -\frac{\sqrt{2}}{2} & -\frac{\sqrt{2}}{2} \end{bmatrix} \left(0.8 \begin{bmatrix} f_1, f_2, f_3, f_4, \end{bmatrix}^\top \right) \\ \tau_z^t &= \begin{bmatrix} d_{1,f/t} & -d_{2,f/t} & d_{3,f/t} & -d_{4,f/t} \end{bmatrix} \left(0.2 \begin{bmatrix} f_1, f_2, f_3, f_4, \end{bmatrix}^\top \right).\end{aligned} \tag{6.55}$$

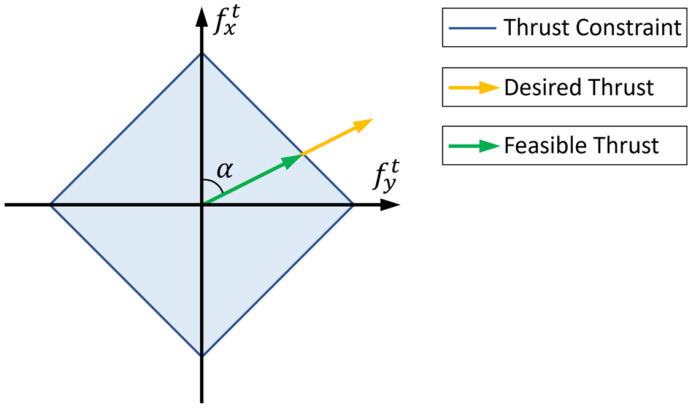

Figure 6.21: Maximum available thrust on $O_tX_tY_t$ plane.

The saturation for the steering torque τ_z^t can be designed from the thrust range of the horizontal motors shown in Figure 6.22. However, as seen in Figure 6.21, the maximum thrust envelope on $O_tX_tY_t$ plane is diamond-shaped. This indicates the maximum propulsion along X_t and Y_t axes will be larger than that in other directions on $O_tX_tY_t$. Therefore, a saturation function is designed to scale thrust vector $[f_x^t, f_y^t]^\top$ to the feasible magnitude, while maintaining the direction of propulsion. We first compute the angle α between the thrust vector $[f_x^t, f_y^t]^\top$ and the X_t axis:

$$\alpha = \text{atan2}(f_y^t, f_x^t). \tag{6.56}$$

Next, we compare the magnitude of the thrust vector $[f_x^t, f_y^t]^\top$ with the thrust envelope on

Figure 6.21. The maximum feasible thrust for a given angle α can be calculated as:

$$f_{constraint}(\alpha) = 0.8\frac{\sqrt{2}f_{1,max}}{|\cos\alpha| + |\sin\alpha|}, \tag{6.57}$$

where $f_{1,max}$ represents the maximum propulsion of the first thruster, as can be found in Figure 6.22. Owing to the symmetrical design of GT-MAB 2.0, $f_{1,max} = f_{2,max} = f_{3,max} = f_{4,max}$. In the scenario that the magnitude of the thrust vector $[f_x^t, f_y^t]^\top$ exceeds the constraint, $[f_x^t, f_y^t]^\top$ is scaled as:

$$\begin{bmatrix} f_x^t \\ f_y^t \end{bmatrix} = f_{constraint}(\alpha) \begin{bmatrix} \cos(\alpha) \\ \sin(\alpha) \end{bmatrix}, \text{if } \left\| [f_x^t, f_y^t]^\top \right\| > f_{constraint}(\alpha). \tag{6.58}$$

Mixer design

After the desired actuation $\boldsymbol{\tau}^t$ been rescaled to the feasible range, a mixer is designed to map $\boldsymbol{\tau}^t$ to the desired propulsion force from individual thrusters. Given that we only run the horizontal thrusters in forward direction, thus f_1 to f_4 are non-negative, the mixer matrix is designed as:

$$\begin{bmatrix} f_1 \\ f_2 \\ f_3 \\ f_4 \\ f_5 \\ f_6 \end{bmatrix} = \begin{bmatrix} 0 & \frac{\sqrt{2}}{2} & \frac{\sqrt{2}}{2} & 0 & 0 & \frac{1}{2d_{1,f/t}} & 0 \\ \frac{\sqrt{2}}{2} & 0 & \frac{\sqrt{2}}{2} & 0 & 0 & 0 & \frac{1}{2d_{2,f/t}} \\ \frac{\sqrt{2}}{2} & 0 & 0 & \frac{\sqrt{2}}{2} & 0 & \frac{1}{2d_{3,f/t}} & 0 \\ 0 & \frac{\sqrt{2}}{2} & 0 & \frac{\sqrt{2}}{2} & 0 & 0 & \frac{1}{2d_{4,f/t}} \\ 0 & 0 & 0 & 0 & -\frac{1}{2} & 0 & 0 \\ 0 & 0 & 0 & 0 & -\frac{1}{2} & 0 & 0 \end{bmatrix} \begin{bmatrix} f_x^t H(f_x^t) \\ -f_x^t H(-f_x^t) \\ f_y^t H(f_y^t) \\ -f_y^t H(-f_y^t) \\ f_z^t \\ \tau_z^t H(\tau_z^t) \\ -\tau_z^t H(-\tau_z^t) \end{bmatrix}, \tag{6.59}$$

where $H(\cdot)$ denotes Heaviside function, and is defined as $H(\cdot) = (sgn(\cdot) + 1)/2$.

Thruster compensation

The next step is to find the required duty cycle d_1 to d_6 given the desired thrust from each motor f_1 to f_6. Owing to the symmetrical design of GT-MAB 2.0, the mapping for the four horizontal motors, and for the two vertical thrusters are identical. The relationship for both types of motors are shown in Figure 6.22. The mappings for both groups of motors are measured by a pre-calibrated strain gauge sensor. Since the motor vibration induces noise in the measurement, we incorporate a signal acquisition device to collect large amounts of data, and estimate the propulsion force from the statistics. For convenience, linear interpolation is incorporated to find the corresponding duty cycle for a desired propulsion force.

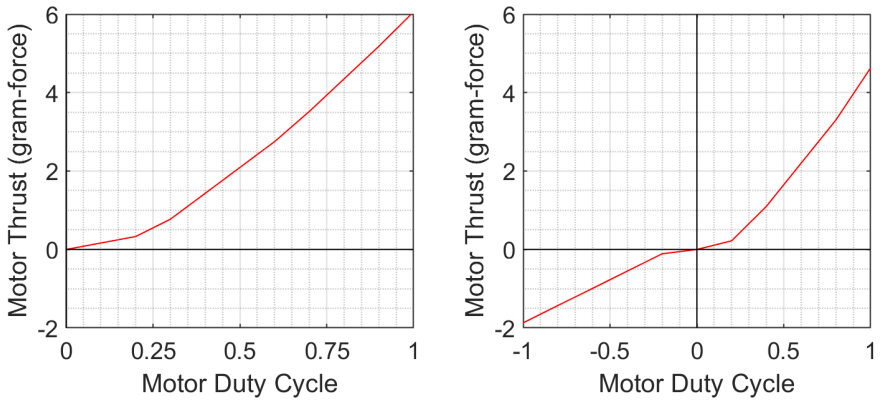

Figure 6.22: Thrust versus duty cycle curve for motors horizontally installed on $O_tX_tY_t$ plane (left), and vertically mounted along Z_t (right).

GT-MAB interface

The GT-MAB interface converts the duty cycle to a specific command format to drive the airborne robot. In order to cancel moments generated by the spinning motors, half of the motors spin in a clockwise fashion and the other half spin in the opposite direction. For instance, the two vertical motors are counter-rotating to cancel the undesired torque reaction about Z_t axis. Therefore, the polarity of the duty cycles are remapped to adapt the electrical connections for thrusters that run in opposite directions. Before the encapsulation of the

data packet, a checksum is calculated from the resulting duty cycle. Then, the command packet is delivered to the aerial blimp through the ground station transceiver.

6.3 Improved Station-keeping and Waypoint Navigation

A new flight control system is designed by incorporating the swing-reducing velocity controller developed in Chapter 6.2. Both waypoint navigation and station-keeping features are realized by expanding the underlying velocity controller with position feedback. We refer to this flight control system as FCS 2.0. Table 6.2 compares the key functionalities of FCS 2.0 with its predecessors.

The overall block diagram of FCS 2.0 is demonstrated in Figure 6.29. We first apply the velocity controller for both longitudinal and lateral movements of GT-MAB. Then, position tracking is added in an outer loop that provides the setpoints for the velocity controllers. The position tracking is combined with heading and altitude control to navigate the blimp to the desired 3D position and heading. Next, we implement a waypoint switching logic, which allows the GT-MAB to automatically follow a sequence of waypoints.

Table 6.2: Comparison among major generations of flight control systems

Term	FCS 1.0	FCS 1.5	FCS 2.0
Planar movement	Nonholonomic	Holonomic	Holonomic
Waypoint navigation	Yes	No	Yes
Station keeping	No	Yes	Yes
Swing stabilization	No	Yes	Yes
Target platform	GT-MAB 1.0	GT-MAB 1.5	GT-MAB 2.0
Underlying motion model	Decoupled	Decoupled	Coupled

Planar velocity control

Owing to the symmetrical design of GT-MAB, the velocity controller in Chapter 6.2 is applied to both longitudinal and lateral movements. Thus the planar velocities of the GT-MAB, $v^b_{x,g/n}$ and $v^b_{y,g/n}$, can be separately controlled for omnidirectional maneuverability.

A series of experiments are conducted to validate the simultaneous velocity tracking for both $v^b_{x,g/n}$ and $v^b_{y,g/n}$. Figure 6.23 demonstrates the result of one of these experiments. The setpoint velocities of surge and sway movements are both $0.2\mathrm{m/s}$. As seen in the plot, the blimp can track both longitudinal and lateral velocities as expected. The experiment is repeated by flying the blimp along different directions. Specifically, four directions forward and backward along body axes, and four additional orientations 45 $^\circ$ from the body axes. The experimental results for all eight directions are plotted in Appendix E. Video demonstrations of the flight tests are available at `https://youtu.be/RMQ4PWRr_Uw`.

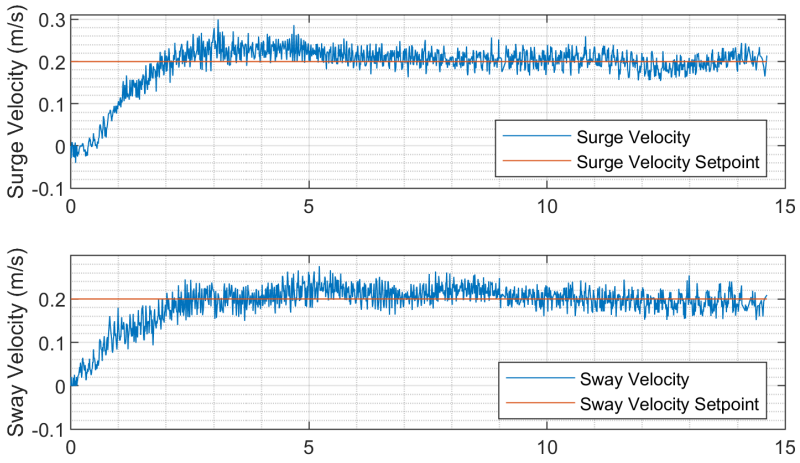

Figure 6.23: Simultaneous velocity control of both surge and sway movements. Both longitudinal and lateral motions can track the setpoint velocities.

Planar position tracking

The position tracking controller is designed to navigate the GT-MAB to the desired location in the inertial frame. As shown in Figure 6.29, the position tracking serves as an outer loop that provides the setpoints for the underlying velocity controllers. We denote $\boldsymbol{r}^n_{v,g/n} = [r^n_{vx,g/n}, r^n_{vy,g/n}, r^n_{vz,g/n}]^\top$ as the setpoint velocities in the inertial frame $\{n\}$. With the feedback gains for the position errors on the planar plane, k^n_{px} and k^n_{py}, the setpoint

velocities for the planar movement can be calculated as:

$$\begin{aligned} r^n_{vx,g/n} &= k^n_{px} e^n_{px,g/n} \\ r^n_{vy,g/n} &= k^n_{py} e^n_{py,g/n}. \end{aligned} \tag{6.60}$$

The desired velocities $r^n_{vx,g/n}$ and $r^n_{vy,g/n}$ are expressed in inertial frame, and need to be transformed to the setpoint longitudinal and lateral velocities of the blimp. With the rotation matrix $\boldsymbol{R}(\cdot)$ defined in Chapter 4.2, the relationship between the velocities in the inertial and the body frame can be found as:

$$\boldsymbol{r}^b_{v,g/n} = \boldsymbol{R}^n_g(\boldsymbol{\Theta}_{ng})^{-1} \boldsymbol{r}^n_{v,g/n}, \tag{6.61}$$

where the detailed derivation of the attitude $\boldsymbol{\Theta}_{ng}$ can be found in Appendix B.

Due to the confined indoor environments with human-occupation, the maximum cruising velocity for both longitudinal and lateral motion is limited to 0.3m/s. As demonstrated in Figure 6.24, the blimp will travel at the cruising velocity under large position error.

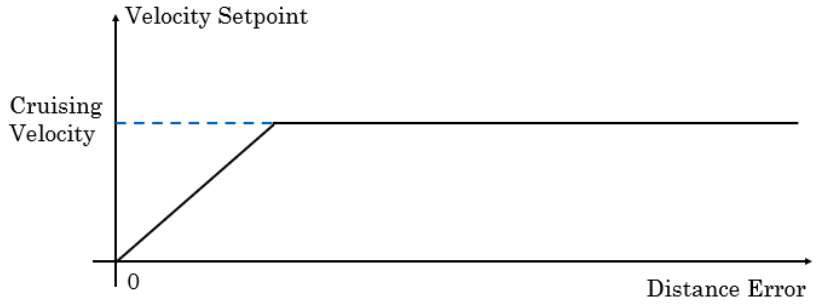

Figure 6.24: Relationship between the setpoint velocity and the position error. The GT-MAB will travel at the cruising velocity under large position error.

Improved station-keeping control

The planar position tracking controller is expanded to station-keeping flight by incorporating the altitude controller designed in Chapter 6.2.5. A series of experiments are designed to evaluate the performance improvements compared to the existing station-keeping func-

tionality developed in Chapter 6.1.

The performance improvements on the station-keeping flight is the result of both the controller design and the latest GT-MAB platform. Therefore, we first discuss the improvements due to the platform upgrade using the same controller, and then present the benefits of the new flight controller on the same platform. The first two subplots in Figure 6.25 compare the station-keeping trajectories with GT-MAB 1.5 and GT-MAB 2.0 under the same controller as developed in Chapter 6.1.4. As listed in Table 6.3, the standard deviation from the desired position is significantly smaller with GT-MAB 2.0. Moreover, due to the asymmetric actuation of GT-MAB 1.5, especially on the longitudinal direction, larger position drift is observed compare to that of GT-MAB 2.0 with symmetrical configuration. With the same GT-MAB platform, the station-keeping performance of FCS 2.0 and FCS 1.5 is compared with the last two subplots in Figure 6.25. As listed in Table 6.3, both the mean and standard deviation of the position drift under FCS 2.0 are reduce by approximately one magnitude compare to its predecessor. This experimental result indicates the new flight controller can better resist environmental disturbance to keep the blimp at the desired position. A video demonstration of the flight test is available at `https://youtu.be/qmfE4kUqfUs`.

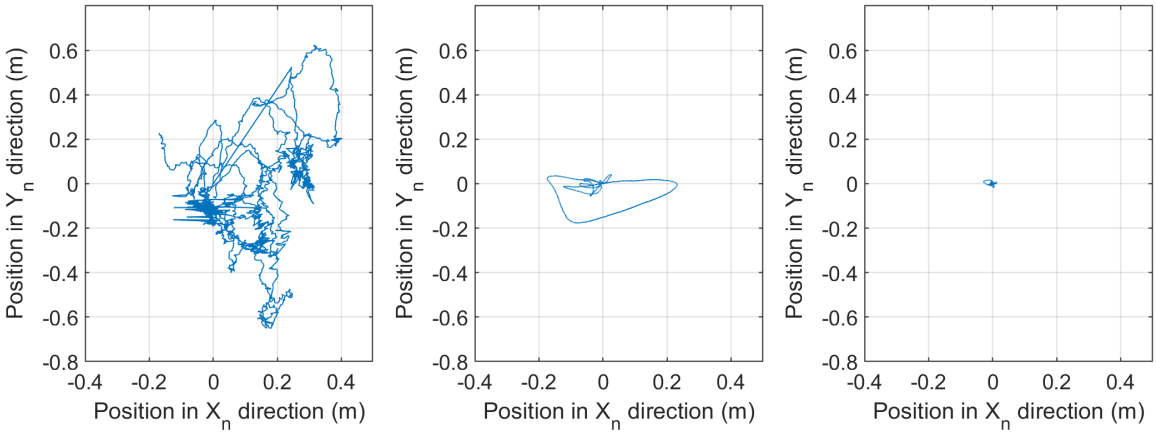

Figure 6.25: Station-keeping trajectories of FCS 1.5 with GT-MAB 1.5 (left), FCS 1.5 with GT-MAB 2.0 (middle), and FCS 2.0 with GT-MAB 2.0 (right).

Table 6.3: Station-keeping performance with different GT-MAB and FCS generations

Experimental Setup	Mean / Std. Dev. ($p^n_{x,g/n}$)	Mean / Std. Dev. ($p^n_{y,g/n}$)
FCS 1.5 with GT-MAB 1.5	0.1290 / 0.1207	-0.0395 / 0.2584
FCS 1.5 with GT-MAB 2.0	-0.0284 / 0.0757	-0.0136 / 0.0416
FCS 2.0 with GT-MAB 2.0	-0.0014 / 0.0059	0.0006 / 0.0055

Improved waypoint navigation

As illustrated in Figure 6.29, a waypoint switching logic is implemented on top of the position tracking controllers to navigate the blimp through a set of waypoints. Once the blimp comes within a specified distance to a waypoint, the blimp will then navigate towards the next waypoint in the sequence. Table 6.4 compares the key features of the proposed waypoint navigation with FCS 2.0, and those of its predecessor developed in Chapter 4.

Table 6.4: Comparison between the waypoint navigation with FCS 1.0 and FCS 2.0

Feature	FCS 1.0	FCS 2.0
Planar motion	Non-holonomic	Holonomic
Velocity control	No	Yes
Swing stabilization	No	Yes
Target platform	GT-MAB 1.0	GT-MAB 2.0
Trajectory consistency	Poor	Good
Typical waypoint switching radius	0.4m	0.2m

An experiment is designed to compare the trajectories of the waypoint navigation with FCS 2.0 and FCS 1.0. As shown in Figure 6.26, waypoints with the same altitude and horizontal positions of (1.2, 1.2), (-1,1.2), (-1,-1.2), and (1.2,-1.2) are assigned to both flight control systems. The waypoint-following trajectory with FCS 1.0 can be seen in the right subplot of Figure 6.26. With nonholonomic planar maneuverability, FCS 1.0 has to steer the blimp toward the corresponding waypoint, and then fly to the destination. However, the steering movement has non-neglectable settling time, typically 2-3 seconds for a 90-degree-turn. During the steering period, the forward momentum will carry the blimp beyond the already-reached waypoint. As a consequence, large overshot in trajectory will occur if the blimp performs sharp turns. Moreover, sideway drift of the blimp cannot be

corrected by FCS 1.0 due to the lack of lateral controllability, causing large cross-track error. In contrast, waypoint navigation with FCS 2.0 utilizes the holonomic maneuverability of the latest hardware platform. Longitudinal and lateral movements can be simultaneously controlled with the underlying position-tracking controller. As shown in Figure 6.26, more consistent and accurate trajectory can be achieved with the new waypoint controller. Moreover, owing to the omnidirectional mobility of GT-MAB 2.0, steering is not required for the waypoint navigation. Therefore, the user is able to control the heading of the blimp independently from the translational movement. This feature is particularly useful for inspection and human-robot interaction, where the heading of the blimp should be independently controlled to keep the camera always pointing to the object.

The waypoint navigation with FCS 2.0 is then expanded to follow 3D waypoints by incorporating the altitude-tracking controller designed in Chapter 6.2.5. As shown in Figure 6.27, GT-MAB can follow a sequence of waypoints with different altitudes. A video demonstration of the flight test can be seen at `https://youtu.be/1fNTU-4myms`. Moreover, the robustness of the waypoint navigation is validated with added airflow disturbance. As shown in Figure 6.28, airflow of 1m/s is applied perpendicular to the setpoint trajectory. Despite the ground speed for both surge and sway motion being set to 0.3m/s for indoor operation, the blimp is able to recover from the large airflow disturbance with acceptable cross-track deviation. A demonstration video of this experiment is available at `https://youtu.be/mKcZWja-UgM`.

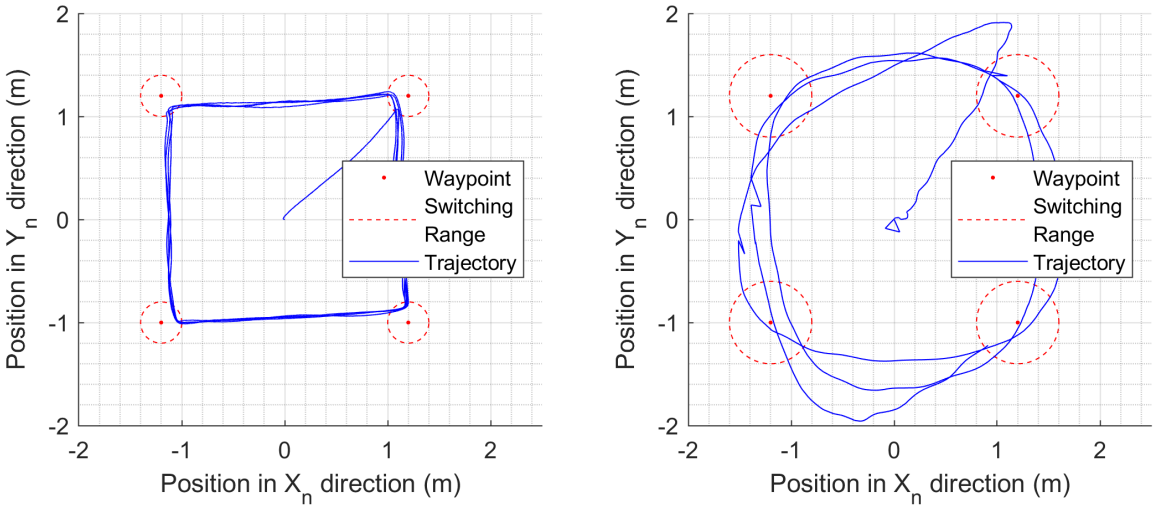

Figure 6.26: Waypoint navigation trajectory with FCS 2.0 (left) and FCS 1.0 (right). The blimp started at the origin, and visited waypoints with the same altitude and horizontal positions of (1.2, 1.2), (-1,1.2), (-1,-1.2), and (1.2,-1.2).

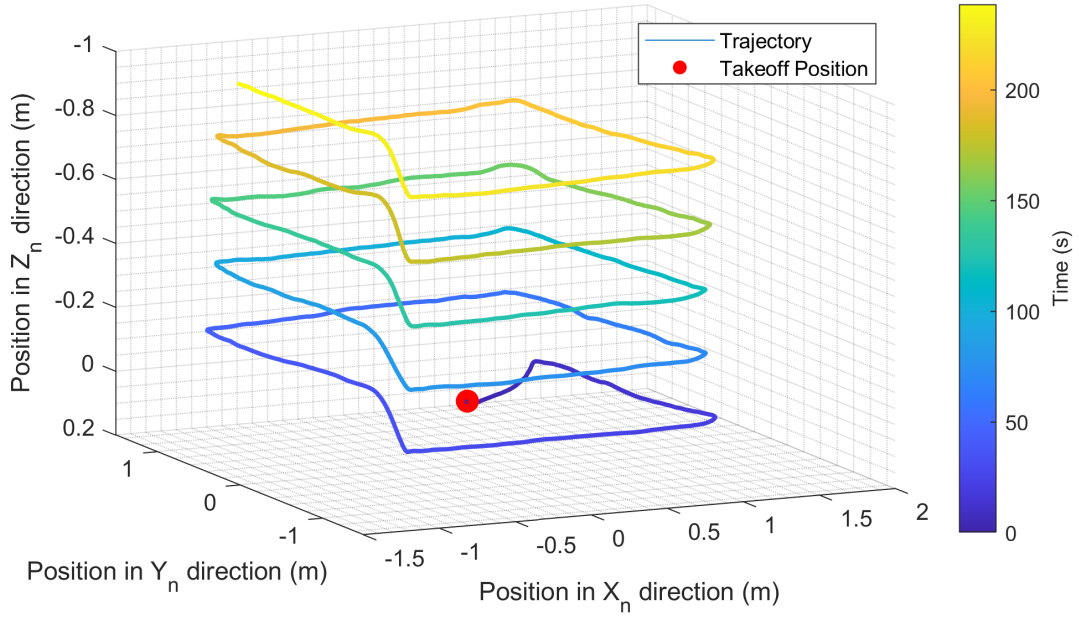

Figure 6.27: GT-MAB follows waypoints in 3D space with FCS 2.0. The blimp started at the origin, and visited waypoints with horizontal positions of (1.2, 1.2), (-1,1.2), (-1,-1.2), and (1.2,-1.2), and heights of 0, 0.2, 0.4, 0.6, 0.8 and 1.0 meters.

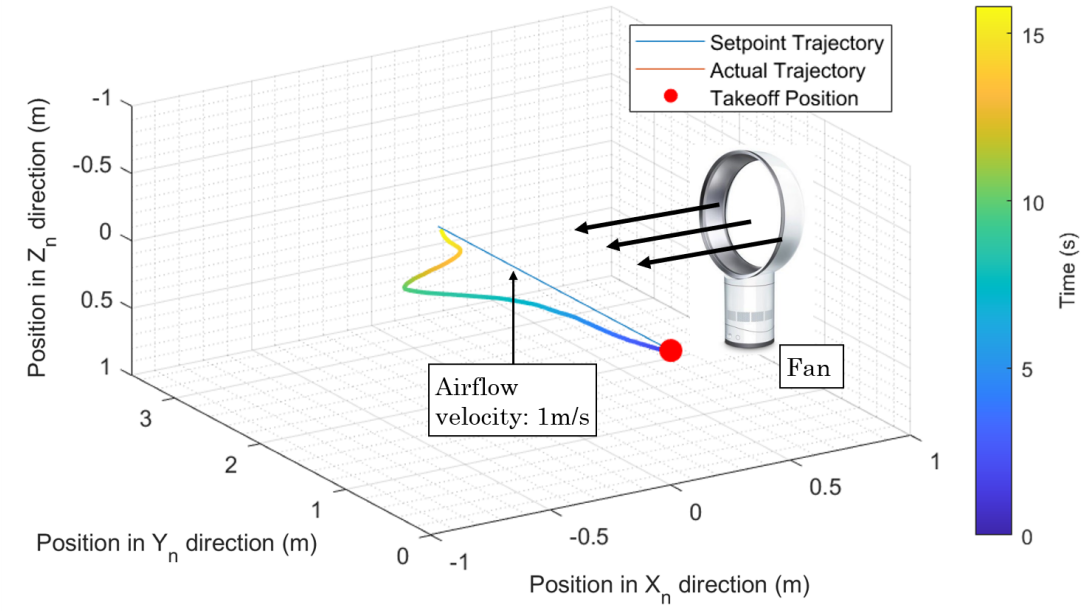

Figure 6.28: Waypoint navigation trajectory under airflow disturbance. The blimp started at the origin and travels along Y_n direction. Maximum cross-track error of 0.41m is observed.

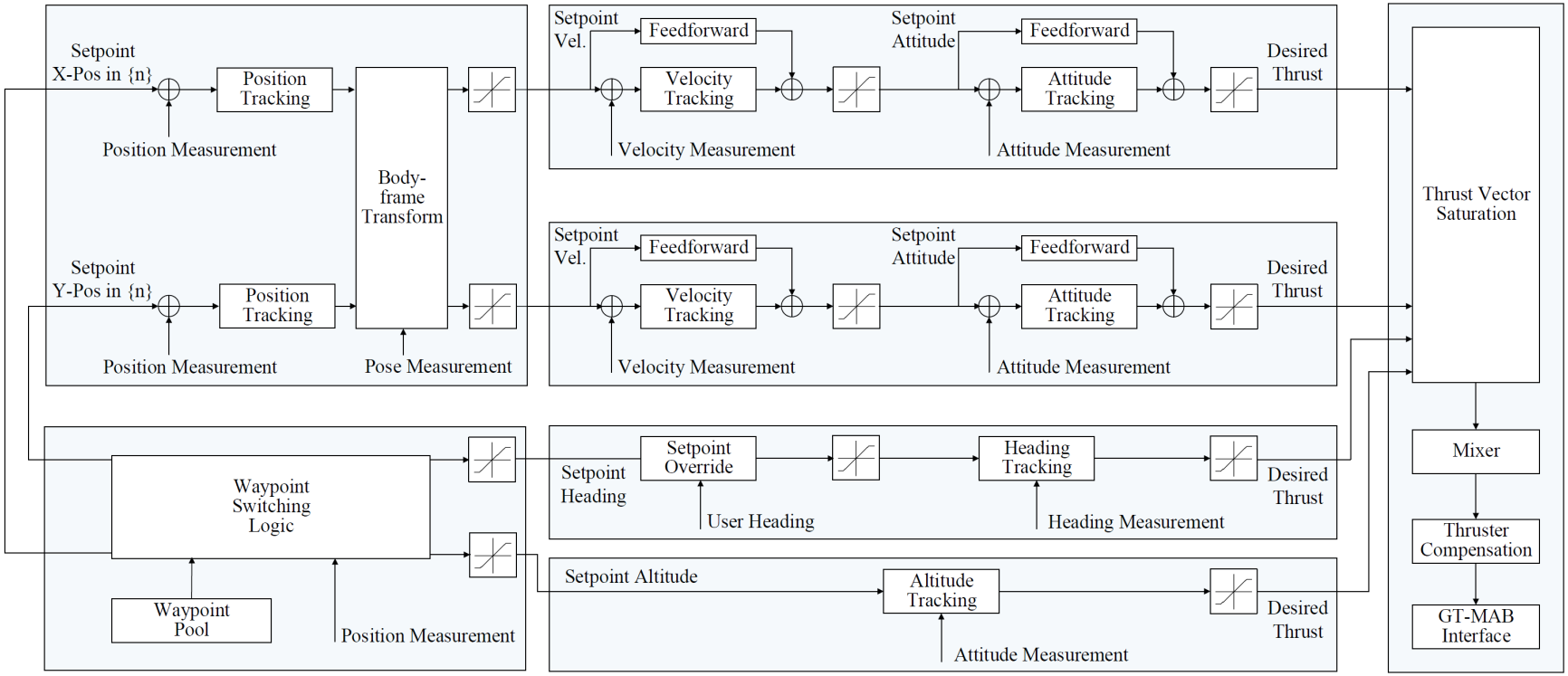

Figure 6.29: Functional block diagram of the second generation flight control system, FCS 2.0.

CHAPTER 7
CONCLUSIONS AND FUTURE WORK

7.1 Concluding Remarks

This thesis presents the development, modeling and control of an autonomous miniature blimp for indoor applications such as human-robot interaction and infrastructure inspection. Such applications require extended flight duration for sustained airborne presence, and safety for operating in close proximity to humans and surrounding objects.

We present the development of an autonomous miniature blimp that is safe to operate and can fly for multiple hours, solving the two biggest challenges for indoor aerial robots. The blimp prototype outlined in this work, the GT-MAB, is a synergistic integration of electromechanical design, control theory, and computer science. Exclusive features of the GT-MAB include a saucer-shaped design without tail fin, symmetrical planar actuation, a low-latency off-board control scheme, ultra-light-weight electronics and improved localization are discussed in this dissertation. The GT-MAB also features a compact design for good mobility in confined indoor spaces, making it one of smallest autonomous blimps in the world.

The modeling and controller design of the GT-MAB is presented with emphasis on the swing oscillation reduction. We incorporate the generic kinematics and dynamics model of underwater vehicles given that the density of the GT-MAB is identical to the surrounding air. The generic model is then simplified for both hovering and cruising flight. The model parameters for both flying scenarios are identified from multiple approaches including physical measurements, computer modeling and experimental data captured during flight. Next, a swing-reducing flight control system is first developed for the hovering case, and then extended for cruising flight by incorporating the coupling between the transla-

tional and rotational movements. Waypoint navigation and station-keeping in 3D space are also realized and experimentally validated with swing stabilization. This dissertation demonstrates the autonomous flight of saucer-shaped indoor blimp with no control surface or tail fin. The modeling and control methods for the swing stabilization feature is the first and only realization among indoor miniature blimps.

7.2 Future Directions

There exist many exciting directions for future work. In the following, we summarize three long-term goals of this project.

- **Vision-based localization:** External motion capture systems are required for most indoor miniature blimps including the GT-MAB. Such systems provide accurate measurements but are also expensive to purchase. Installation and calibration are also required for these localization systems, which limits the deployment of GT-MAB in uninstrumented environments. Therefore, we aim to develop algorithms and systems that allow for localization only using sensors that are onboard the blimp. Preliminary work has been done which develops a localization strategy that incorporates data from an onboard monocular camera and laser range finder [53]. Future works on this thread include exploring new neural network structures for better visual processing, and designing sensor fusion algorithms for additional onboard sensors.

- **Full 6-DOF maneuverability:** Existing miniature indoor blimps usually have one single gondola installed at the bottom of the envelope. The bottom heavy design contributes to the stability of roll and pitch motion, but also the reduced DOF of motion. Given the ultra-light-weight and modular onboard electronics of GT-MAB, it is feasible and beneficial to expand the maneuverability of the blimp to full 6-DOF. The CG position can also coincide with the center of buoyancy for agile mobility. The fully-actuated MAB will allow the generation of force and torque in all three

dimensions, which enables the tracking of arbitrary 6-DOF trajectories and expands the feasible flight maneuvers. The dynamics model and control system of the GT-MAB will also be extended to full 6-DOF in addition to the mechatronics design.

- **Online system identification and anomaly detection:** Though the consistency of the GT-MAB is considered in the design and further enhanced by incorporating automated production, its dynamics model can still deviate due to different payloads and ballast settings. Therefore online system identification is proposed to capture the deviations of model parameters, and provide adjustments to the flight controller accordingly. Moreover, by monitoring the model parameters and the motion trajectory of the blimp, anomalies such as a defective actuator, can be detected.

Appendices

APPENDIX A

ACRONYMS AND SYMBOLS

Table A.1: List of Abbreviations

Abbreviations	Explanation
3D	Three Dimensional
CB	Center of Buoyancy
CG	Center of Gravity
CV	Center of Volume
CAD	Computer Aided Design
CFD	Computational Fluid Dynamics
DOF	Degree of Freedom
IMU	Inertial Measurement Unit
LTAR	Lighter Than Air Robot
MAB	Miniature Autonomous Blimp
MPC	Model Predictive Control
PID	Proportional Integral Derivative
QP	Quadratic Program
RF	Radio Frequency
UWB	Ultra Wide Band

Table A.2: Symbols that related to the coordinate frames and kinematics

Symbol	Explanation
$\{l\}$	Earth-fixed frame of localization device
$\{n\}$	Earth-fixed inertial frame with NED convention
$\{b\}$	Body-fixed frame at the center of buoyancy
$\{g\}$	Body-fixed frame at the center of gravity
$\{m\}$	Body-fixed frame at the center of markers
$\{t\}$	Body-fixed frame at the center of thrusters
$\boldsymbol{\eta}^n_{b/n} = [\boldsymbol{p}^{n\top}_{b/n}, \boldsymbol{\Theta}^\top_{nb}]^\top$	Pose of CB in inertial frame $\{n\}$
$\boldsymbol{\eta}^n_{g/n} = [\boldsymbol{p}^{n\top}_{g/n}, \boldsymbol{\Theta}^\top_{ng}]^\top$	Pose of CG in inertial frame $\{n\}$
$\boldsymbol{\eta}^l_{m/l}$	Pose of markers $\{m\}$ in localization device $\{l\}$
$\boldsymbol{p}^n_{b/n} = [p^n_{x,b/n}, p^n_{y,b/n}, p^n_{z,b/n}]^\top$	Position of CB in inertial frame $\{n\}$
$\boldsymbol{p}^n_{g/n} = [p^n_{x,g/n}, p^n_{y,g/n}, p^n_{z,g/n}]^\top$	Position of CG in inertial frame $\{n\}$
$\boldsymbol{p}^l_{m/l}$	Position of O_m in $\{l\}$
$\boldsymbol{p}^n_{m/n}$	Position of O_m in $\{n\}$
$\boldsymbol{p}^n_{l/n}$	Position of O_l in inertial frame $\{n\}$
$\boldsymbol{p}^m_{b/m}$	Position of CB in $\{m\}$
$\boldsymbol{\Theta}_{nb} = [\phi, \theta, \psi]^\top$	Euler angles between $\{b\}$ and $\{n\}$
$\boldsymbol{\Theta}_{ng} = [\phi, \theta, \psi]^\top$	Euler angles between $\{g\}$ and $\{n\}$
$\boldsymbol{\Theta}_{nl}$	Euler angles between $\{l\}$ and $\{n\}$
$\boldsymbol{\Theta}_{nm}$	Euler angles between $\{m\}$ and $\{n\}$
$\boldsymbol{\Theta}_{lm}$	Euler angles between $\{m\}$ and $\{l\}$
$\boldsymbol{q}_{lm} = [q_x, q_y, q_z, q_w]^\top$	Quaternion angles between $\{m\}$ and $\{l\}$
$\boldsymbol{\nu}^b_{b/n} = [\boldsymbol{v}^{b\top}_{b/n}, \boldsymbol{\omega}^{b\top}_{b/n}]^\top$	Velocities of CB in body frame $\{b\}$
$\boldsymbol{\nu}^b_{g/n} = [\boldsymbol{v}^{b\top}_{g/n}, \boldsymbol{\omega}^{b\top}_{g/n}]^\top$	Velocities of CG in body frame $\{b\}$
$\boldsymbol{v}^b_{b/n} = [v^b_{x,b/n}, v^b_{y,b/n}, v^b_{z,b/n}]^\top$	Translational velocities of CB in $\{b\}$
$\boldsymbol{v}^b_{g/n} = [v^b_{x,g/n}, v^b_{y,g/n}, v^b_{z,g/n}]^\top$	Translational velocities of CG in $\{b\}$
$\boldsymbol{\omega}^b_{b/n} = [\omega^b_{x,b/n}, \omega^b_{y,b/n}, \omega^b_{z,b/n}]^\top$	Angular velocities of CB in $\{b\}$
$\boldsymbol{\omega}^b_{g/n} = [\omega^b_{x,g/n}, \omega^b_{y,g/n}, \omega^b_{z,g/n}]^\top$	Angular velocities of CG in $\{b\}$
$\boldsymbol{J}_{\boldsymbol{\Theta}}(\boldsymbol{\eta})$	Transformation matrix
$\boldsymbol{T}_{\boldsymbol{\Theta}}(\boldsymbol{\Theta})$	Translation matrix
$\boldsymbol{R}^n_b(\boldsymbol{\Theta})$	Rotation matrix
$\boldsymbol{S}(\cdot)$	Skew symmetric operator

Table A.3: Symbols that related to the characteristics of GT-MAB

Symbol	Explanation
$\boldsymbol{r}^b_{b/b} = [r^b_{x,b/b}, r^b_{y,b/b}, r^b_{z,b/b}]^\top$	CB position in body frame $\{b\}$
$\boldsymbol{r}^b_{g/b} = [r^b_{x,g/b}, r^b_{y,g/b}, r^b_{z,g/b}]^\top$	CG position in body frame $\{b\}$
$\boldsymbol{r}^b_{t/b} = [r^b_{x,t/b}, r^b_{y,t/b}, r^b_{z,t/b}]^\top$	Thruster position $\{t\}$ in body frame $\{b\}$
$\boldsymbol{r}^b_{t/g} = [r^b_{x,t/g}, r^b_{y,t/g}, r^b_{z,t/g}]^\top$	Thruster position $\{t\}$ in body frame $\{g\}$
$\boldsymbol{d}_{f/t} = [d_{1,f/t}, \ldots, d_{6,f/t}]^\top$	Distances between the thrusters and O_t
τ_{inflated}	Thickness of the inflated envelope
r_{inflated}	Radius of the inflated envelope
r_{deflated}	Radius of the deflated envelope
H_{ENV}	Measured thickness of the envelope
H_{GON}	Measured thickness of the gondola
V_{envelope}	Volume of the envelope
V_{helium}	Volume of helium gas inside the envelope
ρ_{helium}	Density of helium gas inside the envelope
ρ_{air}	Density of air surround the envelope
m_{RB}	Rigid-body mass of GT-MAB
m_{Ax}, m_{Ay}, m_{Az}	Added mass for motion along X_b, Y_b and Z_b axes
m_{gondola}	Mass of the gondola
m_{ballast}	Mass of the ballast weight
m_{envelope}	Mass of the deflated envelope
m_{marker}	Mass of the localization markers
m_{helium}	Mass of helium gas inside the envelope
$I_{RBx}, I_{RBy}, I_{RBz}$	Rigid-body inertia for rotation about X_b, Y_b and Z_b axes
I_{Ax}, I_{Ay}, I_{Az}	Added inertia for rotation about X_b, Y_b and Z_b axes
$\boldsymbol{I}^{CG}$	Total inertia matrix at CG
$\boldsymbol{M}^{CB}_{RB}$	Rigid-body system inertia matrix at CB
$\boldsymbol{M}^{CB}_{A}$	Added system inertia matrix at CB
$\boldsymbol{M}^{CB}$	Total system inertia matrix at CB
$\boldsymbol{C}^{CB}_{RB}$	Rigid-body Coriolis-centripetal matrix at CB
$\boldsymbol{C}^{CB}_{A}$	Added Coriolis-centripetal matrix at CB
$\boldsymbol{C}^{CB}$	Total Coriolis-centripetal matrix at CB
$D^{CB}_{vx}, D^{CB}_{vy}, D^{CB}_{vz}$	Drag coefficient for motion along X_b, Y_b and Z_b axes
$D^{CB}_{\omega x}, D^{CB}_{\omega y}, D^{CB}_{\omega z}$	Drag coefficient for rotation about X_b, Y_b and Z_b axes
$\boldsymbol{D}^{CB}$	Aerodynamic drag coefficient matrix

Table A.4: Symbols that related to the characteristics of GT-MAB (continued)

Symbol	Explanation
V_{batt}	Battery voltage
$d_{mtr,i}$	Duty cycle of the i-th motor
$V_{\mathrm{mtr,i}}$	Terminal voltage of the i-th motor
$\Phi_{\mathrm{mtr,i}}$	Shaft angle of the i-th motor
$\omega_{\mathrm{mtr,i}}$	Shaft velocity of the i-th motor
β_{mtr}	Static gain of the DC motor model
τ_{mtr}	Time constant of the DC motor model
$f_{i,max}$	Maximum thrust of the i-th motor
α	Angle between planar thrust vector and X_t axis
$f_{constraint}(\alpha)$	Maximum feasible thrust on $O_tX_tY_t$ at angle α
$\boldsymbol{f}_l^n = [f_{lx}^n, f_{ly}^n, f_{lz}^n]^\top$	Lifting force from the envelope in $\{n\}$
$\boldsymbol{f}_b^b = [f_{bx}^b, f_{by}^b, f_{bz}^b]^\top$	Total buoyancy from the envelope in $\{b\}$
$\boldsymbol{f}_b^n = [f_{bx}^n, f_{by}^n, f_{bz}^n]^\top$	Total buoyancy from the envelope in $\{n\}$
$\boldsymbol{f}_g^b = [f_{gx}^b, f_{gy}^b, f_{gz}^b]^\top$	Rigid-body gravitational force in $\{b\}$
$\boldsymbol{f}_g^n = [f_{gx}^n, f_{gy}^n, f_{gz}^n]^\top$	Rigid-body gravitational force in $\{n\}$
$\boldsymbol{g}^{CB} = [g_x^{CB}, g_y^{CB}, g_z^{CB}]^\top$	Restoring torque at CB
$\boldsymbol{g}^{CG} = [g_x^{CG}, g_y^{CG}, g_z^{CG}]^\top$	Restoring torque at CG
$\boldsymbol{F}^g = [F_x^g, F_y^g, F_z^g]^\top$	Sum of forces at CG except actuation
$\boldsymbol{M}^g = [M_x^g, M_y^g, M_z^g]^\top$	Sum of moments at CG except actuation

Table A.5: Symbols that related to the controller design of GT-MAB

Symbol	Explanation
$\boldsymbol{r}_{\boldsymbol{\Theta}} = [r_\phi, r_\theta, r_\psi]^\top$	Setpoint attitude
$\boldsymbol{e}_{\boldsymbol{\Theta}} = [e_\phi, e_\theta, e_\psi]^\top$	Attitude error
$\boldsymbol{r}^b_{\omega,g/n} = [r^b_{\omega x,g/n}, r^b_{\omega y,g/n}, r^b_{\omega z,g/n}]^\top$	Setpoint angular velocity at CG in $\{b\}$
$\boldsymbol{e}^b_{\omega,g/n} = [e^b_{\omega x,g/n}, e^b_{\omega y,g/n}, e^b_{\omega z,g/n}]^\top$	Angular velocity error at CG in $\{b\}$
$\boldsymbol{r}^n_{p,g/n} = [r^n_{px,g/n}, r^n_{py,g/n}, r^n_{pz,g/n}]^\top$	Setpoint position of CG in $\{n\}$
$\boldsymbol{e}^n_{p,g/n} = [e^n_{px,g/n}, e^n_{py,g/n}, e^n_{pz,g/n}]^\top$	Position error of CG in $\{n\}$
$\boldsymbol{r}^n_{v,g/n} = [r^n_{vx,g/n}, r^n_{vy,g/n}, r^n_{vz,g/n}]^\top$	Setpoint velocity of CG in $\{n\}$
$\boldsymbol{r}^b_{v,g/n} = [r^b_{vx,g/n}, r^b_{vy,g/n}, r^b_{vz,g/n}]^\top$	Setpoint velocity of CG in $\{b\}$
$\boldsymbol{e}^b_{v,g/n} = [e^b_{vx,g/n}, e^b_{vy,g/n}, e^b_{vz,g/n}]^\top$	Velocity error of CG in $\{b\}$
$\boldsymbol{f}^g = [f^b_x, f^b_y, f^b_z]^\top$	Total translational control effort in $\{g\}$
$\boldsymbol{m}^g = [\tau^b_x, \tau^b_y, \tau^b_z]^\top$	Total rotational control effort in $\{g\}$
$\boldsymbol{\tau}^b = [f^b_x, f^b_y, f^b_z, \tau^b_x, \tau^b_y, \tau^b_z]^\top$	Total control effort in $\{b\}$
$\boldsymbol{\tau}^g = [f^g_x, f^g_y, f^g_z, \tau^g_x, \tau^g_y, \tau^g_z]^\top$	Total control effort in $\{g\}$
$\boldsymbol{\tau}^t = [f^t_x, f^t_y, f^t_z, \tau^t_x, \tau^t_y, \tau^t_z]^\top$	Total control effort in $\{t\}$
$\boldsymbol{x} = [v^b_{x,g/n}, v^b_{z,g/n}, \theta, \omega^b_{y,g/n}]^\top$	System states for the coupled 3DOF motion
$\boldsymbol{x}_0 = [v^b_{x,g/n,0}, v^b_{z,g/n,0}, \theta_0, \omega^b_{y,g/n,0}]^\top$	System states at equilibrium
$\Delta\boldsymbol{x}_0$	Deviation from the equilibrium
$\boldsymbol{f}(\boldsymbol{x})$	System state functions
$\boldsymbol{J}$	Jacobian matrix at equilibrium
$\boldsymbol{u} = [f^g_x, f^g_z, \tau^g_y]^\top$	System inputs
$\boldsymbol{u}_0 = [f^g_{x,0}, f^g_{z,0}, \tau^g_{y,0}]^\top$	System inputs at equilibrium
$\Delta\boldsymbol{u}$	System inputs for deviation correction
$\boldsymbol{x}_p = [v^b_{x,g/n}, \theta, \omega^b_{y,g/n}]^\top$	System states for the planar motion
$\boldsymbol{x}_{p,0} = [v^b_{x,g/n,0}, \theta_0, \omega^b_{y,g/n,0}]^\top$	System states at equilibrium
$\Delta\boldsymbol{x}_p$	Deviation from the equilibrium
$\boldsymbol{f}_p(\boldsymbol{x}_p)$	System state functions
$\boldsymbol{J}_p$	Jacobian matrix at equilibrium
$\boldsymbol{u}_p = [f^g_x, \tau^g_y]^\top$	System inputs
$\boldsymbol{u}_{p,0} = [f^g_{x,0}, \tau^g_{y,0}]^\top$	System inputs at equilibrium
$\Delta\boldsymbol{u}_p$	System inputs for deviation correction
$\theta_{feedforward}$	Feedforward component of the setpoint attitude
$\theta_{feedback}$	Feedback component of the setpoint attitude
x_v	System state for the vertical motion
u_v	System input for the vertical motion

Table A.6: Symbols that related to the controller design of GT-MAB (continued)

Symbol	Explanation
τ_{sys}	Overall control system latency
$k^n_{px}, k^n_{py}, k^n_{pz}$	Proportional gains for position errors in $\{n\}$
$k^n_{ix}, k^n_{iy}, k^n_{iz}$	Integral gains for position errors in $\{n\}$
$k^n_{dx}, k^n_{dy}, k^n_{dz}$	Derivative gains for position errors in $\{n\}$
k^g_{pv}, k^g_{iv}	PI gains for velocity errors in $\{g\}$
$k_{p\psi}, k_{i\psi}, k_{d\psi}$	PID gains for the heading error
$k_\theta, k_\omega, k_\alpha$	Feedback gains for pitch angle, angular rate and acceleration
J_{mpc}	MPC cost function
J_y	MPC cost function term for tracking error
$J_{\Delta u}$	MPC cost function term for actuation change rate
w_y	Tuning weight for tracking error
$w_{\Delta u}$	Tuning weight for actuation change rate
$\boldsymbol{U}_k$	Quadratic program decision
N_p	Prediction horizon
N_c	Control horizon

APPENDIX B

DERIVATION OF POSE AND VELOCITY AT CB AND CG

Miniature blimps use indoor localization systems due to the GPS-denied environment. These devices usually have different coordinate systems compared to the desired inertial frame. Therefore, pose measurements from the motion capture systems need to be converted to the inertial frame.

B.1 Pose and Velocities at CB

We start with the raw measurements from the localization system. We define the pose of the markers measured by the motion capture system, thus the pose of $\{m\}$ in $\{l\}$ as:

$$\boldsymbol{\eta}_{m/l}^{l} = [\boldsymbol{p}_{m/l}^{l}, \boldsymbol{\Theta}_{lm}]^{\top}, \tag{B.1}$$

where $\boldsymbol{p}_{m/l}^{l}$ and $\boldsymbol{\Theta}_{lm}$ are the position and attitude separately. If the attitude is given in Euler angles, the rotation matrix can be calculated with $\boldsymbol{R}(\cdot)$ defined in Chapter 4.2. If the attitude is given in quaternion form, $\boldsymbol{q}_{lm} = [q_x, q_y, q_z, q_w]^{\top}$, the rotation matrix can be calculated by:

$$\begin{aligned} &\boldsymbol{R}_{m}^{l}(\boldsymbol{q}_{lm}) = \boldsymbol{R}_{m}^{l}(\boldsymbol{\Theta}_{lm}) = \\ &\begin{bmatrix} 1-2(q_y^2+q_z^2) & 2(q_xq_y - q_zq_w) & 2(q_xq_z + q_yq_w) \\ 2(q_xq_y + q_zq_w) & 1-2(q_x^2+q_z^2) & 2(q_yq_z - q_xq_w) \\ 2(q_xq_z - q_yq_w) & 2(q_yq_z + q_xq_w) & 1-2(q_x^2+q_y^2) \end{bmatrix}. \end{aligned} \tag{B.2}$$

Next, we calculate the rotation matrix between $\{m\}$ and $\{n\}$. The attitude of the markers in the inertial frame, $\boldsymbol{R}_{m}^{n}(\boldsymbol{\Theta}_{nm})$, can be presented as consecutive rotations among $\{n\}$,

$\{l\}$ and $\{m\}$:

$$\boldsymbol{R}_m^n(\boldsymbol{\Theta}_{nm}) = \boldsymbol{R}_l^n(\boldsymbol{\Theta}_{nl})\boldsymbol{R}_m^l(\boldsymbol{\Theta}_{lm}), \tag{B.3}$$

where $\boldsymbol{\Theta}_{nl}$ and $\boldsymbol{R}_l^n(\boldsymbol{\Theta}_{nl})$ denote the orientation and the corresponding rotation matrix between $\{l\}$ and $\{n\}$. The angles are usually constant due to the fixed installation of the motion capture systems. In our experimental setup, $\boldsymbol{p}_{l/n}^n = [0, 0, 0]^\top$ because origins of $\{l\}$ and $\{n\}$ are at the same position. Due to the Y-up convention used in the motion capture system, the rotation matrix between $\{l\}$ and $\{n\}$ is:

$$\boldsymbol{R}_l^n(\boldsymbol{\Theta}_{nl}) = \begin{bmatrix} 1 & 0 & 0 \\ 0 & 0 & 1 \\ 0 & -1 & 0 \end{bmatrix}. \tag{B.4}$$

Then, we find the positions of O_m and O_b in the inertial frame as:

$$\begin{aligned} \boldsymbol{p}_{m/n}^n &= \boldsymbol{p}_{l/n}^n + \boldsymbol{R}_l^n(\boldsymbol{\Theta}_{nl})\boldsymbol{p}_{m/l}^l \\ \boldsymbol{p}_{b/n}^n &= \boldsymbol{p}_{m/n}^n + \boldsymbol{R}_m^n(\boldsymbol{\Theta}_{nm})\boldsymbol{p}_{b/m}^m, \end{aligned} \tag{B.5}$$

where $\boldsymbol{p}_{b/m}^m$ is the position of CB in the body-fixed frame $\{m\}$. For indoor MABs, $\boldsymbol{p}_{b/m}^m$ is usually a constant that solely determined by the geometry of the blimp. For GT-MAB, this position is $\boldsymbol{p}_{b/m}^m = [0, -H_{ENV}/2, 0]^\top$. Thus, the position of $\{b\}$ in $\{n\}$ can be written as:

$$\boldsymbol{p}_{b/n}^n = \boldsymbol{p}_{l/n}^n + \boldsymbol{R}_l^n(\boldsymbol{\Theta}_{nl})(\boldsymbol{p}_{m/l}^l + \boldsymbol{R}_m^l(\boldsymbol{\Theta}_{lm})\boldsymbol{p}_{b/m}^m). \tag{B.6}$$

The orientation between $\{b\}$ and $\{n\}$, can be represented as rotation matrix of consecutive rotations among $\{b\}$, $\{m\}$, $\{l\}$ and $\{n\}$:

$$\boldsymbol{R}_b^n(\boldsymbol{\Theta}_{nb}) = \boldsymbol{R}_l^n(\boldsymbol{\Theta}_{nl})\boldsymbol{R}_m^l(\boldsymbol{\Theta}_{lm})\boldsymbol{R}_b^m(\boldsymbol{\Theta}_{mb}), \tag{B.7}$$

where $\boldsymbol{\Theta}_{mb}$ and $\boldsymbol{R}_b^m(\boldsymbol{\Theta}_{mb})$ denote the orientation and the corresponding rotation matrix

between $\{m\}$ and $\{b\}$. Due to the Y-up convention used for the localization markers, the rotation matrix $\boldsymbol{R}_b^m$ can be found as:

$$\boldsymbol{R}_b^m(\boldsymbol{\Theta}_{mb}) = \begin{bmatrix} 1 & 0 & 0 \\ 0 & 0 & -1 \\ 0 & 1 & 0 \end{bmatrix}. \tag{B.8}$$

Then, the Euler angle $\boldsymbol{\Theta}_{nb}$ can be calculated from the rotation matrix $\boldsymbol{R}_b^n(\boldsymbol{\Theta}_{nb})$. We use "ZYX" convention in this work, and assume both roll and pitch angle of the blimp are within the range of $(-\pi/2, \pi/2)$. For convenience, we define rotation matrix $\boldsymbol{R}_b^n(\boldsymbol{\Theta}_{nb})$ and euler angle $\boldsymbol{\Theta}_{nb}$ as:

$$\boldsymbol{R}_b^n(\boldsymbol{\Theta}_{nb}) = \begin{bmatrix} R_{11} & R_{12} & R_{13} \\ R_{21} & R_{22} & R_{23} \\ R_{31} & R_{32} & R_{33} \end{bmatrix}. \tag{B.9}$$

The euler angle $\boldsymbol{\Theta}_{nb} = [\phi, \theta, \psi]^\top$ can be found as:

$$\begin{aligned} \phi &= \operatorname{atan2}(R_{32}, R_{33}) \\ \theta &= -\sin^{-1}(R_{31}) \\ \psi &= \operatorname{atan2}(R_{21}, R_{11}). \end{aligned} \tag{B.10}$$

The translational and angular velocity in the body-fixed frame $\{b\}$ can then be found with the rotation $\boldsymbol{R}(\cdot)$ and transformation matrix $\boldsymbol{T}(\cdot)$ defined in Chapter 4.2.

$$\begin{aligned} \boldsymbol{v}_{b/n}^b &= \boldsymbol{R}_b^n(\boldsymbol{\Theta}_{nb})^{-1}\dot{\boldsymbol{p}}_{b/n}^n \\ \boldsymbol{\omega}_{b/n}^b &= \boldsymbol{T}_{\boldsymbol{\Theta}}(\boldsymbol{\Theta}_{nb})^{-1}\dot{\boldsymbol{\Theta}}_{nb}. \end{aligned} \tag{B.11}$$

B.2 Pose and Velocities at CG

The pose and velocities at CG can be derived from the results at CB. Since $\{g\}$ and $\{b\}$ are both attached on the blimp and aligned with each other, we get:

$$\begin{aligned} \boldsymbol{\Theta}_{bg} &= [0,0,0]^\top \\ \boldsymbol{R}_g^b(\boldsymbol{\Theta}_{bg}) &= \begin{bmatrix} 1 & 0 & 0 \\ 0 & 1 & 0 \\ 0 & 0 & 1 \end{bmatrix}. \end{aligned} \tag{B.12}$$

Therefore, the attitude at CG are the same as that at CB:

$$\begin{aligned} \boldsymbol{R}_g^n(\boldsymbol{\Theta}_{ng}) = \boldsymbol{R}_b^n(\boldsymbol{\Theta}_{nb})\boldsymbol{R}_g^b(\boldsymbol{\Theta}_{bg}) &= \boldsymbol{R}_b^n(\boldsymbol{\Theta}_{nb}) \\ \boldsymbol{\Theta}_{ng} &= \boldsymbol{\Theta}_{nb}. \end{aligned} \tag{B.13}$$

Then, the position and translational velocity of CG can be found as:

$$\boldsymbol{p}_{g/n}^n = \boldsymbol{p}_{l/n}^n + \boldsymbol{R}_l^n(\boldsymbol{\Theta}_{nl})(\boldsymbol{p}_{m/l}^l + \boldsymbol{R}_m^l(\boldsymbol{\Theta}_{lm})\boldsymbol{p}_{g/m}^m), \tag{B.14}$$

where $\boldsymbol{p}_{g/m}^m$ is the position of CG in the body-fixed frame $\{m\}$. For indoor MABs, $\boldsymbol{p}_{g/m}^m$ is usually a constant that solely determined by the geometry of the blimp. For GT-MAB, this position is $\boldsymbol{p}_{g/m}^m = [0, -H_{ENV}/2 - r_{z,g/b}^b, 0]^\top$.

The translational and angular velocity in the body-fixed frame $\{g\}$ can then be found with the rotation $\boldsymbol{R}(\cdot)$ and transformation matrix $\boldsymbol{T}(\cdot)$ defined in Section 4.2.

$$\begin{aligned} \boldsymbol{v}_{g/n}^b &= \boldsymbol{R}_b^n(\boldsymbol{\Theta}_{nb})^{-1}\dot{\boldsymbol{p}}_{g/n}^n \\ \boldsymbol{\omega}_{g/n}^b &= \boldsymbol{T}_{\boldsymbol{\Theta}}(\boldsymbol{\Theta}_{ng})^{-1}\dot{\boldsymbol{\Theta}}_{ng} = \boldsymbol{\omega}_{b/n}^b. \end{aligned} \tag{B.15}$$

APPENDIX C

JACOBIAN MATRIX

C.1 Jacobian Matrix of Planar Motion at CG

The Jacobian matrix $\boldsymbol{J}_p$ described in Eq. (6.32) in Chapter 6.2.3 can be expanded as:

$$
\begin{aligned}
J_{p,11} &= \frac{-D_{vx}^{CB} I_y^{CG} + D_{vx}^{CB} m_{Ax} {r_{z,g/b}^b}^2}{-{m_{Ax}}^2 {r_{z,g/b}^b}^2 + I_y^{CG} m_x} \\
J_{p,12} &= \frac{-g m_{Ax} m_{RB} {r_{z,g/b}^b}^2 cos(x_{p2})}{-{m_{Ax}}^2 {r_{z,g/b}^b}^2 + I_y^{CG} m_x} \\
J_{p,13} &= \frac{-D_{\omega y}^{CB} m_{Ax} r_{z,g/b}^b - D_{vx}^{CB} m_{Ax} {r_{z,g/b}^b}^3 + D_{vx}^{CB} I_y^{CG} r_{z,g/b}^b}{-{m_{Ax}}^2 {r_{z,g/b}^b}^2 + I_y^{CG} m_x} \\
J_{p,21} &= 0 \\
J_{p,22} &= 0 \\
J_{p,23} &= 1 \\
J_{p,31} &= \frac{D_{vx}^{CB} m_{RB} r_{z,g/b}^b}{-{m_{Ax}}^2 {r_{z,g/b}^b}^2 + I_y^{CG} m_x} \\
J_{p,32} &= \frac{-g m_{RB} m_x r_{z,g/b}^b cos(x_{p2})}{-{m_{Ax}}^2 {r_{z,g/b}^b}^2 + I_y^{CG} m_x} \\
J_{p,33} &= \frac{-D_{\omega y}^{CB} m_x - D_{vx}^{CB} m_{RB} {r_{z,g/b}^b}^2}{-{m_{Ax}}^2 {r_{z,g/b}^b}^2 + I_y^{CG} m_x}.
\end{aligned}
\tag{C.1}
$$

C.2 Jacobian Matrix of 3-DOF Motion at CG

The Jacobian matrix $\boldsymbol{J}$ described in Eq. (6.30) in Chapter 6.2.3 can be expanded as:

$$
\begin{aligned}
J_{11} &= \frac{-m_{Ax}(m_x - m_z)r^b_{z,g/b}x_2 - D^{CB}_{vx}I^{CG}_y + D^{CB}_{vx}m_{Ax}{r^b_{z,g/b}}^2}{-{m_{Ax}}^2{r^b_{z,g/b}}^2 + I^{CG}_y m_x} \\
J_{12} &= \frac{-m_{Ax}(m_x - m_z)r^b_{z,g/b}x_1 - I^{CG}_y m_z x_4 + {m_{Ax}}^2{r^b_{z,g/b}}^2 x_4}{-{m_{Ax}}^2{r^b_{z,g/b}}^2 + I^{CG}_y m_x} \\
J_{13} &= \frac{-g m_{Ax}m_{RB}{r^b_{z,g/b}}^2 cos(x_3)}{-{m_{Ax}}^2{r^b_{z,g/b}}^2 + I^{CG}_y m_x} \\
J_{14} &= \frac{-I^{CG}_y m_z x_2 + {m_{Ax}}^2{r^b_{z,g/b}}^2 x_2 - D^{CB}_{vx}m_{Ax}{r^b_{z,g/b}}^3 + D^{CB}_{vx}I^{CG}_y r^b_{z,g/b} - D^{CB}_{\omega y}m_{Ax}r^b_{z,g/b}}{-{m_{Ax}}^2{r^b_{z,g/b}}^2 + I^{CG}_y m_x} \\
J_{21} &= \frac{m_x x_4}{m_z} \\
J_{22} &= -\frac{D^{CB}_{vz}}{m_z} \\
J_{23} &= 0 \\
J_{24} &= \frac{m_x x_1 - 2m_{Ax}r^b_{z,g/b}x_4}{m_z} \\
J_{31} &= 0 \\
J_{32} &= 0 \\
J_{33} &= 0 \\
J_{34} &= 1 \\
J_{41} &= \frac{-m_x(m_x - m_z)x_2 + D^{CB}_{vx}m_{RB}r^b_{r,g/b}}{-{m_{Ax}}^2{r^b_{z,g/b}}^2 + I^{CG}_y m_x} \\
J_{42} &= \frac{-m_x(m_x - m_z)x_1 + m_{Ax}(m_x - m_z)r^b_{z,g/b}x_4}{-{m_{Ax}}^2{r^b_{z,g/b}}^2 + I^{CG}_y m_x} \\
J_{43} &= \frac{-g m_{RB}m_x r^b_{z,g/b} cos(x_3)}{-{m_{Ax}}^2{r^b_{z,g/b}}^2 + I^{CG}_y m_x} \\
J_{44} &= \frac{m_{Ax}(m_x - m_z)r_{r,g/b}x_2 - D^{CB}_{\omega y}m_x - D^{CB}_{vx}m_{RB}{r^b_{z,g/b}}^2}{-{m_{Ax}}^2{r^b_{z,g/b}}^2 + I^{CG}_y m_x}.
\end{aligned}
\tag{C.2}
$$

APPENDIX D

EXPERIMENTAL RESULTS OF SURGE VELOCITY CONTROL

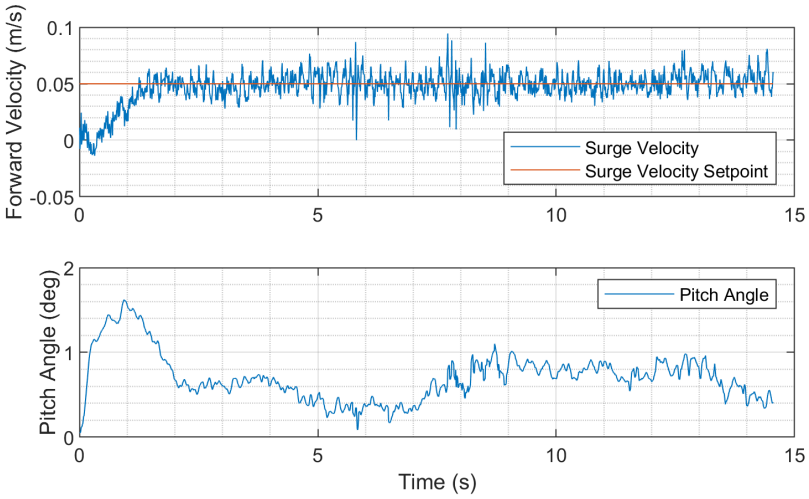

Figure D.1: Forward velocity control with setpoint 0.05m/s.

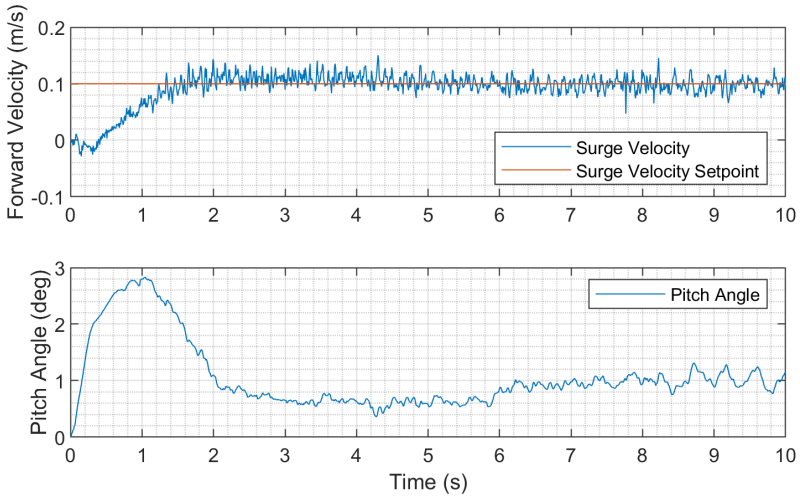

Figure D.2: Forward velocity control with setpoint 0.1m/s.

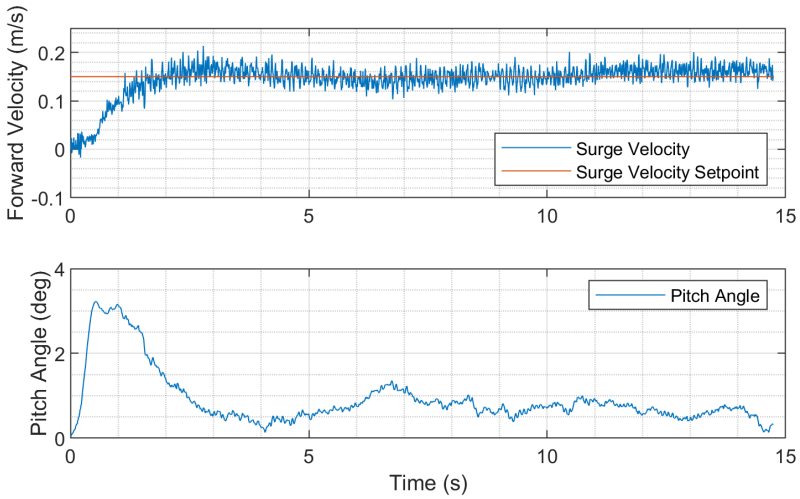

Figure D.3: Forward velocity control with setpoint 0.15m/s.

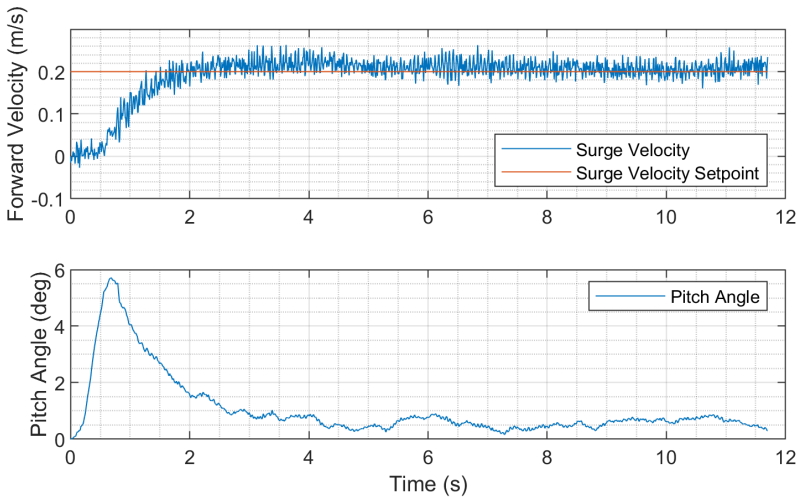

Figure D.4: Forward velocity control with setpoint 0.2m/s.

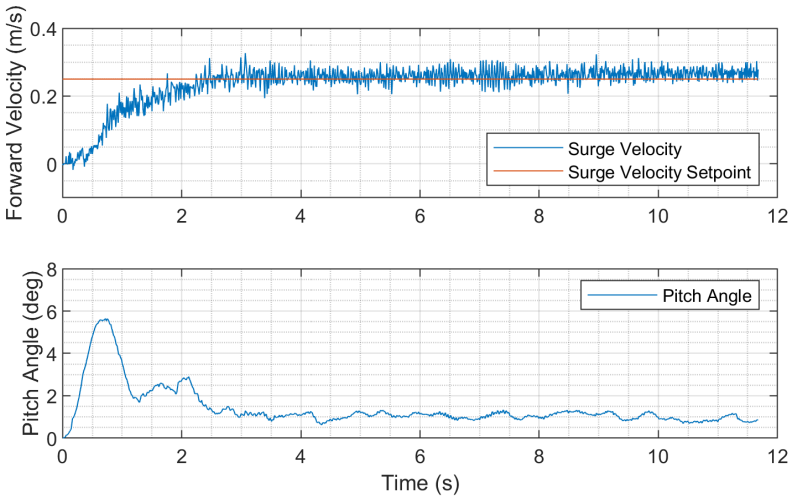

Figure D.5: Forward velocity control with setpoint 0.25m/s.

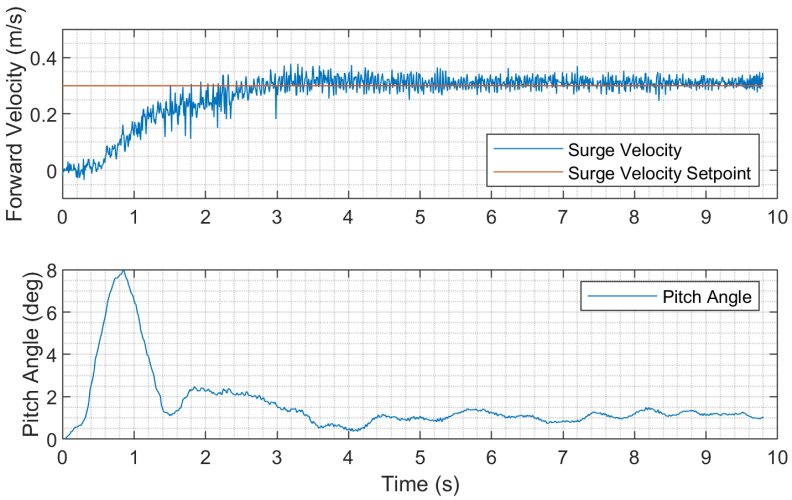

Figure D.6: Forward velocity control with setpoint 0.3m/s.

APPENDIX E

EXPERIMENTAL RESULTS OF SIMULTANEOUS VELOCITY CONTROL FOR BOTH SURGE AND SWAY MOVEMENTS

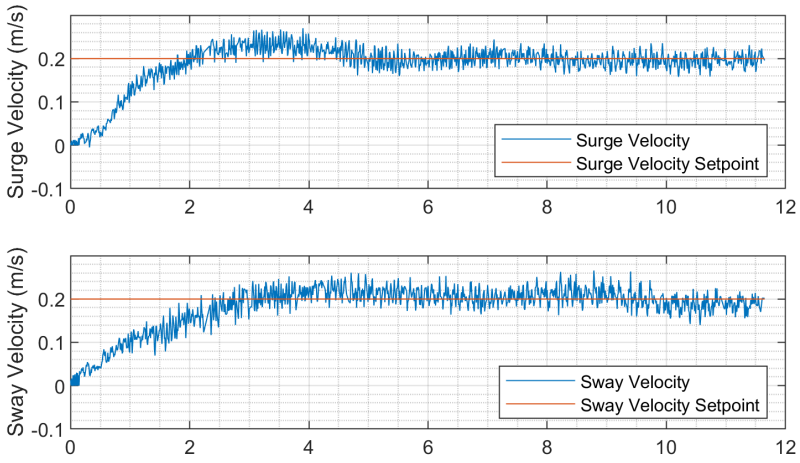

Figure E.1: Simultaneous velocity control for both surge and sway movements. Velocity setpoints for the longitudinal and lateral motions are 0.2m/s and 0.2m/s.

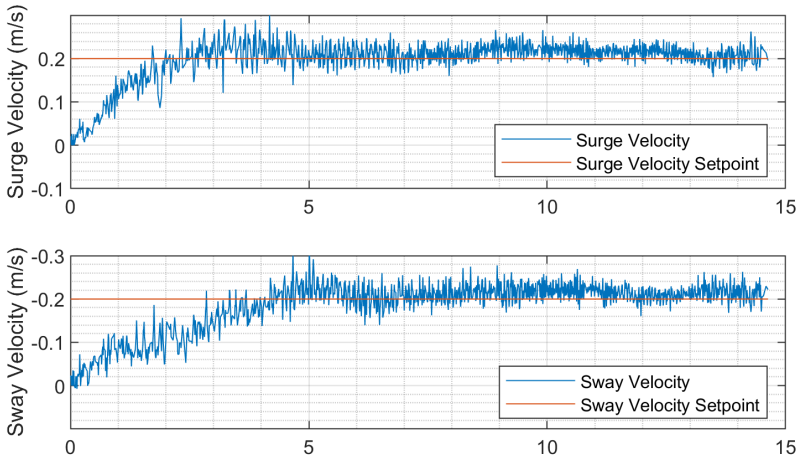

Figure E.2: Simultaneous velocity control for both surge and sway movements. Velocity setpoints for the longitudinal and lateral motions are 0.2m/s and -0.2m/s.

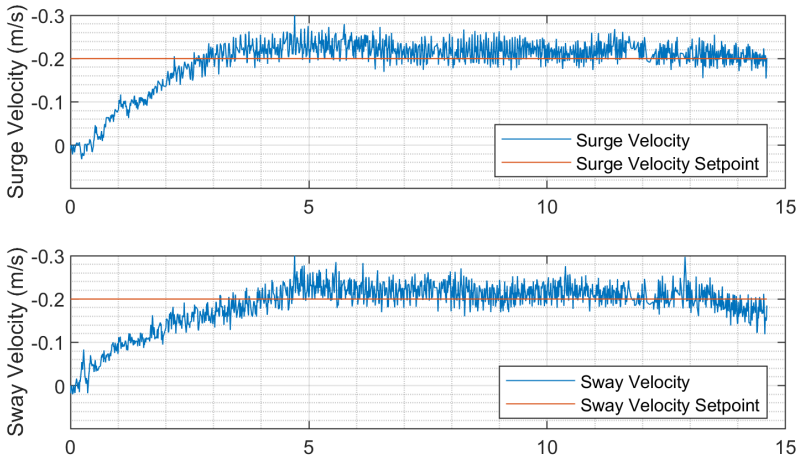

Figure E.3: Simultaneous velocity control for both surge and sway movements. Velocity setpoints for the longitudinal and lateral motions are -0.2m/s and -0.2m/s.

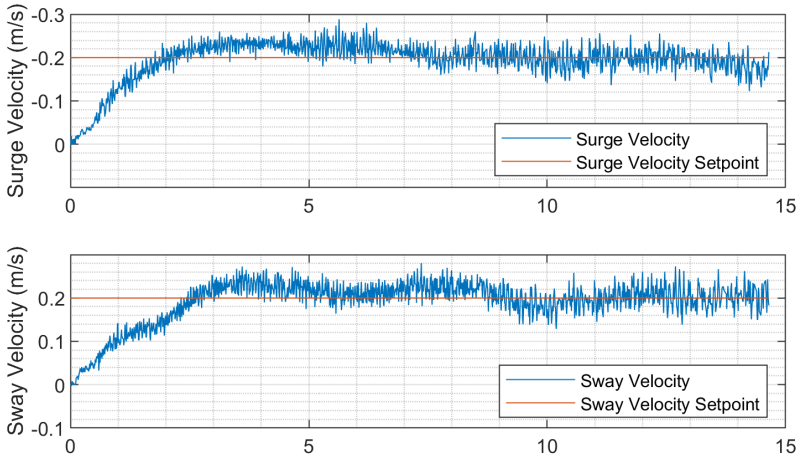

Figure E.4: Simultaneous velocity control for both surge and sway movements. Velocity setpoints for the longitudinal and lateral motions are -0.2m/s and 0.2m/s.

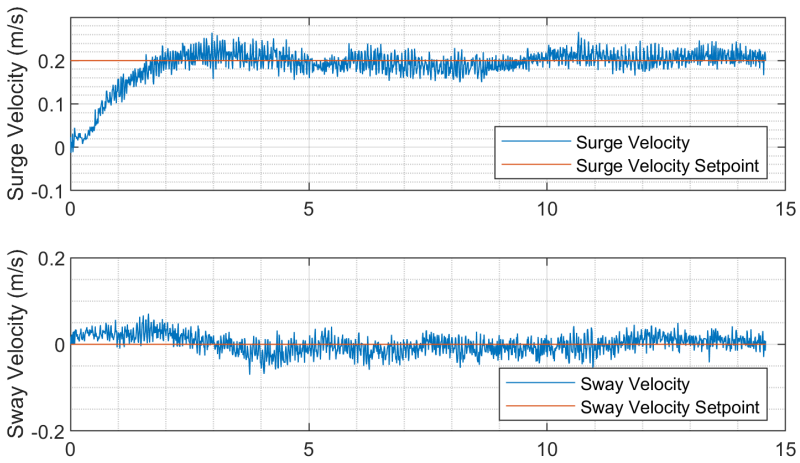

Figure E.5: Simultaneous velocity control for both surge and sway movements. Velocity setpoints for the longitudinal and lateral motions are 0.2m/s and 0m/s.

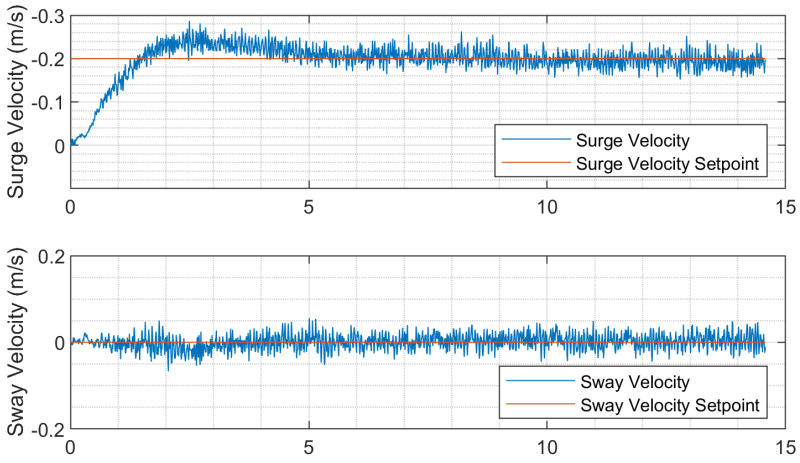

Figure E.6: Simultaneous velocity control for both surge and sway movements. Velocity setpoints for the longitudinal and lateral motions are -0.2m/s and 0m/s.

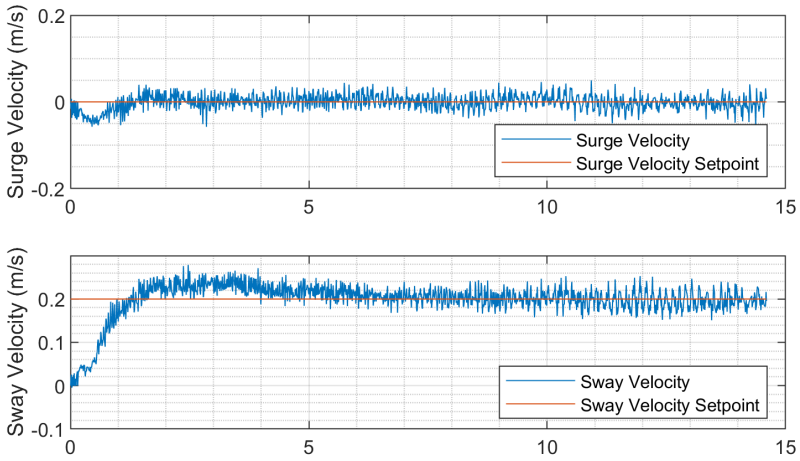

Figure E.7: Simultaneous velocity control for both surge and sway movements. Velocity setpoints for the longitudinal and lateral motions are 0m/s and 0.2m/s.

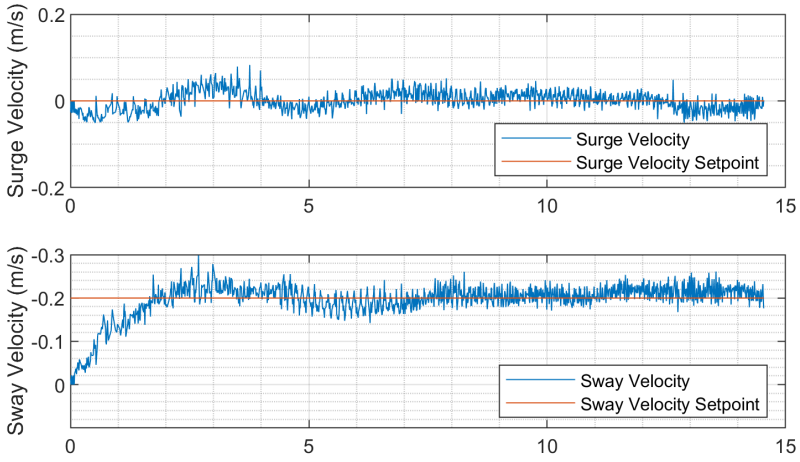

Figure E.8: Simultaneous velocity control for both surge and sway movements. Velocity setpoints for the longitudinal and lateral motions are 0m/s and -0.2m/s.

REFERENCES

[1] D. Palossi, A. Gomez, S. Draskovic, A. Marongiu, L. Thiele, and L. Benini, "Extending the lifetime of nano-blimps via dynamic motor control," *Journal of Signal Processing Systems*, vol. 91, no. 3-4, pp. 339–361, 2018.

[2] Z. Fang and S. Scherer, "Real-time onboard 6dof localization of an indoor MAV in degraded visual environments using a RGB-D camera," in *2015 IEEE International Conference on Robotics and Automation (ICRA)*, 2015, pp. 5253–5259.

[3] K. Asadi, A. K. Suresh, A. Ender, S. Gotad, S. Maniyar, S. Anand, M. Noghabaei, K. Han, E. Lobaton, and T. Wu, "An integrated UGV-UAV system for construction site data collection," *Automation in Construction*, vol. 112, p. 103 068, 2020.

[4] Y. Wang, G. Zheng, D. Efimov, and W. Perruquetti, "Disturbance compensation based controller for an indoor blimp robot," *Robotics and Autonomous Systems*, vol. 124, p. 103 402, 2020.

[5] D. St-Onge, P. Brèches, I. Sharf, N. Reeves, I. Rekleitis, P. Abouzakhm, Y. Girdhar, A. Harmat, G. Dudek, and P. Giguère, "Control, localization and human interaction with an autonomous lighter-than-air performer," *Robotics and Autonomous Systems*, vol. 88, pp. 165–186, 2017.

[6] R. A. S. Fernández, J. L. Sanchez-Lopez, C. Sampedro, H. Bavle, M. Molina, and P. Campoy, "Natural user interfaces for human-drone multi-modal interaction," in *2016 International Conference on Unmanned Aircraft Systems (ICUAS)*, 2016, pp. 1013–1022.

[7] S. Hwan Song, H. Wook Shon, G. Yang Yeon, and H. Ryeol Choi, "Design and implementation of cloud-like soft drone s-cloud," in *2018 IEEE/RSJ International Conference on Intelligent Robots and Systems (IROS)*, 2018, pp. 1–9.

[8] V. Srisamosorn, N. Kuwahara, A. Yamashita, T. Ogata, S. Shirafuji, and J. Ota, "Indoor human face following with environmental fisheye cameras and blimp," *Advanced Robotics*, vol. 34, pp. 621–636, 2020.

[9] N. Yao, E. Anaya, Q. Tao, S. Cho, H. Zheng, and F. Zhang, "Monocular vision-based human following on miniature robotic blimp," in *IEEE International Conference on Robotics and Automation (ICRA)*, 2017, pp. 3244–3249.

[10] S. U. Ferdous, A. Mohammadi, and S. Lakshmanan, "Developing a low-cost autonomous blimp with a reduced number of actuators," in *Unmanned Systems Technology XXI*, vol. 11021, SPIE, 2019, pp. 73–80.

[11] W. Yamada, H. Manabe, and D. Ikeda, "Zerone: Safety drone with blade-free propulsion," in *Proceedings of the 2019 CHI Conference on Human Factors in Computing Systems*, Glasgow, Scotland Uk, 2019, pp. 1–8.

[12] B. Siciliano and O. Khatib, *Springer handbook of robotics*. Germany: Springer-Verlag, 2016.

[13] *Crazyflie 2.1 product page*, https://store.bitcraze.io/products/crazyflie-2-1, [Accessed: 23-May- 2020].

[14] Y. Bestaoui-Sebbane, *Lighter than air robots*. Springer Netherlands, 2012.

[15] C. Blouin, E. Lanteigne, and W. Gueaieb, "Optimal control for the trajectory planning of micro airships," in *2017 International Conference on Unmanned Aircraft Systems (ICUAS)*, 2017, pp. 885–892.

[16] R. Saitou, Y. Ikeda, and Y. Oikawa, "Three-dimensional noise and spatial mapping system with aerial blimp robot," *Acoustical Science and Technology*, vol. 40, no. 1, pp. 12–22, 2019.

[17] T. Takaya, H. Kawamura, Y. Minagawa, M. Yamamoto, and A. Ohuchi, "PID landing orbit motion controller for an indoor blimp robot," *Artificial Life and Robotics*, vol. 10, no. 2, pp. 177–184, 2006.

[18] F. Zhang, Q. Tao, T. Tan, P. Cheng, S. Cho, V. Mishra, and J. Varnell, "Miniature autonomous robotic blimp," U.S. Utility Patent App. 16/280,579.

[19] N. Yao, Q. Tao, W. Liu, Z. Liu, Y. Tian, P. Wang, T. Li, and F. Zhang, "Autonomous flying blimp interaction with human in an indoor space," *Frontiers of Information Technology & Electronic Engineering*, vol. 20, no. 1, pp. 45–59, 2019.

[20] S. Cho, V. Mishra, Q. Tao, P. Varnell, M. King-Smith, A. Muni, W. Smallwood, and F. Zhang, "Autopilot design for a class of miniature autonomous blimps," in *Proc. of IEEE Conference on Control Technology and Applications (CCTA)*, 2017, pp. 841–846.

[21] Z. Ashraf and M. A. Choudhry, "Dynamic modeling of the airship using analytical aerodynamic model," in *2009 International Conference on Emerging Technologies*, 2009, pp. 188–193.

[22] Y. Li, M. Nahon, and I. Sharf, "Airship dynamics modeling: A literature review," *Progress in Aerospace Sciences*, vol. 47, no. 3, pp. 217–239, 2011.

[23] D. Palossi, "Self-sustainability in nano unmanned aerial vehicles: A blimp case study," in *CF'17 Proceedings of the Computing Frontiers Conference*, 2017, pp. 79–88.

[24] S. Kale, P. Joshi, and R. Pant, "A generic methodology for determination of drag coefficient of an aerostat envelope using CFD," *AIAA 5th ATIO and 16th Lighter-Than-Air Sys Tech. and Balloon Systems Conferences*, p. 7442, 2005.

[25] S. B. V. Gomes and J. G. Ramos, "Airship dynamic modeling for autonomous operation," in *Proceedings of IEEE International Conference on Robotics and Automation*, 1998, pp. 3462–3467.

[26] J. Shan, "Dynamic modeling and vision-based control for indoor airship," in *International Conference on Mechatronics and Automation*, 2009, pp. 2934–2939.

[27] Y. Wang, G. Zheng, D. Efimov, and W. Perruquetti, "Altitude control for an indoor blimp robot," *IFAC-PapersOnLine*, vol. 50, no. 1, pp. 15 990–15 995, 2017.

[28] *American blimp mz-3*, https://en.wikipedia.orgwiki/American_Blimp_MZ-3, [Accessed: 28-Mar- 2019].

[29] D. H. Robinson, *Giants in the Sky: A History of the Rigid Airship.* University of Washington Press, 1973.

[30] A. Rottmann, C. Plagemann, P. Hilgers, and W. Burgard, "Autonomous blimp control using model-free reinforcement learning in a continuous state and action space," in *2007 IEEE/RSJ International Conference on Intelligent Robots and Systems*, 2007, pp. 1895–1900.

[31] J. Ko, D. J. Klein, D. Fox, and D. Haehnel, "Gaussian processes and reinforcement learning for identification and control of an autonomous blimp," in *Proceedings 2007 IEEE International Conference on Robotics and Automation*, 2007, pp. 742–747.

[32] S. B. i Badia, P. Pyk, and P. F. M. J. Verschure, "A biologically based flight control system for a blimp-based uav," in *Proceedings of the 2005 IEEE International Conference on Robotics and Automation*, 2005, pp. 3053–3059.

[33] J.-C. Zufferey, A. Guanella, A. Beyeler, and D. Floreano, "Flying over the reality gap: From simulated to real indoor airships," *Autonomous Robots*, vol. 21, no. 3, pp. 243–254, 2006.

[34] M. Mahn and M. Kemper, "A behaviour-based navigation system for an autonomous indoor blimp," *IFAC Proceedings Volumes*, vol. 39, no. 16, pp. 837–842, 2006, 4th IFAC Symposium on Mechatronic Systems.

[35] T. Takaya, H. Kawamura, Y. Minagawa, M. Yamamoto, and A. Ouchi, "Motion control in three dimensional round system of blimp robot," in *2006 SICE-ICASE International Joint Conference*, 2006, pp. 1291–1294.

[36] Q. Tao, M. King-Smith, A. Muni, V. Mishra, S. Cho, P. Varnell, and F. Zhang, "Control theory - autonomous blimp," in *IEEE CSS Video Clip Contest*, 2015.

[37] V. Srisamosorn1, N. Kuwahara, A. Yamashita1, T. Ogata, and J. Ota, "Design of face tracking system using fixed 360-degree cameras and flying blimp for health care evaluation," in *The 4th International Conference on Serviceology*, 2016.

[38] Q. Tao, J. Cha, M. Hou, and F. Zhang, "Parameter identification of blimp dynamics through swinging motion," in *2018 15th International Conference on Control, Automation, Robotics and Vision (ICARCV)*, 2018, pp. 1186–1191.

[39] F. Hayato and S. Akira, "Wind-disturbance-based control approach for blimp robots," *Electronics and Communications in Japan*, vol. 97, no. 2, pp. 52–59,

[40] C. Wan, N. Kingry, and R. Dai, "Design and autonomous control of a solar-power blimp," in *2018 AIAA Guidance, Navigation, and Control Conference, AIAA SciTech Forum*, 2018, p. 1588.

[41] P. Funk, T. Lutz, and S. Wagner, "Experimental investigations on hull-fin interferences of the lotte airship," *Aerospace Science and Technology*, vol. 7, no. 8, pp. 603–610, 2003.

[42] C. Blouin, E. Lanteigne, and W. Gueaieb, "Trajectory optimization of a small airship in a moving fluid," *Transactions of The Canadian Society for Mechanical Engineering*, vol. 40, pp. 191–200, 2016.

[43] Q. Tao, M. Hou, and F. Zhang, "Modeling and identification of coupled translational and rotational motion of underactuated indoor miniature autonomous blimps," in *2020 16th International Conference on Control, Automation, Robotics and Vision (ICARCV)*, in press.

[44] P. Gonzalez, W. Burgard, R. Sanz, and J. L. Fernandez, "Developing a low-cost autonomous indoor blimp," *Journal of Physical Agents*, pp. 43–52, 2009.

[45] H. Kawamura, M. Yamamoto, T. Takaya, and A. Ohuchi, "Learning landing control of an indoor blimp robot for self-energy recharging," *Artificial Life and Robotics*, vol. 12, no. 1, pp. 116–121, 2008.

[46] H. Kawamura, H. Iizuka, T. Takaya, and A. Ohuchi, "Cooperative control of multiple neural networks for an indoor blimp robot," *Artificial Life and Robotics*, vol. 13, no. 2, pp. 504–507, 2009.

[47] Y. Wang, G. Zheng, D. Efimov, and W. Perruquetti, "Improved altitude control method with disturbance compensation for an indoor blimp robot," in *2017 IEEE 56th Annual Conference on Decision and Control (CDC)*, 2017, pp. 3902–3907.

[48] Y. Wang, G. Zheng, D. Efimov, and W. Perruquetti, "Differentiator application in altitude control for an indoor blimp robot," *International Journal of Control*, vol. 91, no. 9, pp. 2121–2130, 2018.

[49] K. Watanabe, N. Okamura, and I. Nagai, "Closed-loop control experiments for a blimp robot consisting of four-divided envelopes," in *IECON 2015 - 41st Annual Conference of the IEEE Industrial Electronics Society*, 2015, pp. 2568–2573.

[50] Q. Tao, T. J. Tan, J. Cha, Y. Yuan, and F. Zhang, "Modeling and control of swing oscillation of underactuated indoor miniature autonomous blimps," *Unmanned Systems*, in press.

[51] M. Hou, Q. Tao, P. Varnell, and F. Zhang, "Modeling pointing tasks in human-blimp interactions," in *2019 IEEE Conference on Control Technology and Applications (CCTA)*, 2019, pp. 73–78.

[52] J. Gibson, T. Schuler, L. McGuire, D. M. Lofaro, and D. Sofge, "Swarm and multi-agent time-based A* path planning for lta3 systems," *Unmanned Systems*, vol. 8, no. 3, pp. 253–260, 2020.

[53] L. Seguin, J. Zheng, A. Li, Q. Tao, and F. Zhang, "A deep learning approach to localization for navigation on a miniature autonomous blimp," in *The 16 th IEEE International Conference on Control & Automation*, in press.

[54] A. Mazumdar, M. S. Triantafyllou, and H. H. Asada, "Dynamic analysis and design of spheroidal underwater robots for precision multidirectional maneuvering," *IEEE/ASME Transactions on Mechatronics*, vol. 20, no. 6, pp. 2890–2902, 2015.

[55] I. M. Mladenov, "On the geometry of the mylar balloon," *Comptes Rendus de l'Academie Bulgare des*, pp. 9–39, 2001.

[56] W. H. Paulsen, "What is the shape of a mylar balloon?" *The American Mathematical Monthly*, vol. 101, no. 10, pp. 953–958, 1994.

[57] *Motion capture for robotics*, http://optitrack.com/motion-capture-robotics, [Accessed: 28-Jun- 2018].

[58] Q. Tao, F. Zhang, T. Lin, and Z. Xu, "Active motion capture marker for miniature indoor aerial robots," U.S. Provisional Patent App. 63/060,836.

[59] T. I. Fossen, *Handbook of Marine Craft Hydrodynamics and Motion Control*. United Kingdom: John Wiley & Sons, 2011.

[60] S. van der Zwaan, A. Bernardino, and J. Santos-Victor, "Vision based station keeping and docking for an aerial blimp," in *Proceedings. 2000 IEEE/RSJ International Conference on Intelligent Robots and Systems (IROS 2000)*, vol. 1, 2000, 614–619 vol.1.

[61] L. Ljung and R. Singh, "Version 8 of the system identification toolbox," in *6th IFAC Symposium on System Identification The International Federation of Automatic Control*, 2012.

[62] N. S. Nise, *Control systems engineering*. Addision-Wesley, 1995.

[63] G. Lu and F. Zhang, "Imu-based attitude estimation in the presence of narrow-band noise," *IEEE/ASME Transactions on Mechatronics*, vol. 24, no. 2, pp. 841–852, 2019.

[64] *About mass properties*, Autodesk Knowledge Network, [Accessed: 28- Jun- 2018].

[65] V. Léchappé, S. Rouquet, A. González, F. Plestan, J. D. León, E. Moulay, and A. Glumineau, "Delay estimation and predictive control of uncertain systems with input delay: Application to a DC motor," *IEEE Transactions on Industrial Electronics*, vol. 63, no. 9, pp. 5849–5857, 2016.